Theses and Dissertations

6-30-2016

Multiscale Modeling of Water Transport and the Influence of Water Quality Parameters on Membrane Processes

Linkel Kwabena Boateng
University of South Carolina

MULTISCALE MODELING OF WATER TRANSPORT AND THE INFLUENCE OF WATER
QUALITY PARAMETERS ON MEMBRANE PROCESSES

by

Linkel Kwabena Boateng

Bachelor of Science
Kwame Nkrumah University of Science and Technology 2007

Master of Science
North Carolina Agricultural and Technical State University 2011

Submitted in Partial Fulfillment of the Requirements

for the Degree of Doctor of Philosophy in

Civil Engineering

College of Engineering and Computing

University of South Carolina

2016

Accepted by:

Joseph R.V. Flora, Major Professor

Yeomin Yoon, Committee Member

Nicole D. Berge, Committee Member

Homayoun Valafar, Committee Member

Lacy Ford, Senior Vice Provost and Dean of Graduate Studies

ii

DEDICATION

To my uncle ***Dr. Robert Baffour*** whose support and inspiration has created a stirring atmosphere for my academic excellence.

ACKNOWLEDGMENTS

I would like to express my sincere gratitude and appreciation to my advisor, Dr. Joseph R.V. Flora, for his professional guidance and very insightful suggestions throughout the course of my study. Molecular modeling couldn't have been this exciting without his enthusiasm and passion. Many thanks to my co-advisor, Dr. Yeomin Yoon and members of my dissertation committee, Drs. Nicole Berge and Homayoun Valafar for their invaluable comments and review of the dissertation. I would like to extend special thanks to my dear wife (Efe Crentsil Boateng) and family members for their support and understanding and also for putting up with my "endless" school work. A sincere gratitude also to friends and colleague graduate students for their encouragement which has made this endeavor a possibility. Again, I would like to thank the University of South Carolina High Performance Computing group for the computational time used in this research. Finally all the thanks to God Almighty for giving me the strength to achieve this. I wouldn't have succeeded without His mercy.

ABSTRACT

Membrane-based desalination processes have become a viable means of producing potable water to meet water resource needs in both industrialized and developing nations. Extensive experimental investigation, in conjunction with computational modeling is critical in the development of sustainable and cost-effective desalination technologies. The overall goal of this dissertation is to develop a multiscale modeling framework to elucidate water and salt transport mechanisms and the influence of water quality parameters on membrane processes. The key tasks involved in this study are: establish a criterion for estimating water flux using Bayesian inference; develop a multiscale framework to connect molecular dynamics (MD) simulations to the process level; and evaluate the influence of different water chemistry conditions on water flux in forward and reverse osmosis membrane processes. Simulations are conducted to evaluate water transport and natural organic matter (NOM) fouling propensity in cellulose-triacetate (CTA) and nanoporous graphene (NPG) membranes. Bayesian updating of a probabilistic model is performed to estimate membrane permeability and a process model is developed to predict full-scale water flux through the membrane. Results of the Bayesian inference indicate that the use of unique structural configurations in MD simulations is essential to capture realistic membrane properties at the molecular scale. Full-scale water flux predictions based on estimated membrane parameters is within the same order of magnitude of experimental data suggesting that simulations at the molecular level can potentially be scaled up to reflect process level conditions. Moreover, surface functionalization of NPG membranes can enhance water flux and salt rejection and improve antifouling capabilities. NOM adsorption onto NPG membrane is energetically favored and results in water flux decline across the membrane due to increased resistance to flow. The results further indicate that fouling propensity of graphene-based

membranes is influenced by surface functionalization which dictates the strength of the interactions between the membranes and potential foulants. This work highlights the feasibility of forward osmosis processes and the potential application of ultrathin graphene membranes for water desalination. The findings can complement experimental studies to better understand observations at the macro-scale and expedite the development of mechanistic strategies for optimizing membrane performance.

TABLE OF CONTENTS

LIST OF FIGURES

x

xi

CHAPTER 1

INTRODUCTION

1.1 Motivation and significance

Recent reports on water scarcity in several parts of the world have accelerated the development of advanced membrane-based water treatment technologies in both industrialized and developing nations. Approximately one-third of Israel's water is expected to be sourced from reverse osmosis (RO) seawater desalination plants by 2020 [1]. Ghana has recently commissioned the first seawater desalination facility in the West African sub-region to expand water supply to surrounding urban communities [2]. Membrane-based water treatment processes have great potential in sustainable water purification and provide a viable avenue for producing potable water from alternative water sources to meet global water demand.

RO membranes have become the world-wide leading desalination technology for producing fresh water from seawater [3]. In recent times, RO desalination installations have significantly increased, accounting for 75% of new production capacity in 2003 [4]. Despite the advancement in RO-based desalination technology, the high energy requirement, coupled with its characteristic low water recovery continues to limit its widespread application in advanced water treatment systems.

Forward osmosis (FO) membranes have drawn special research interest as an alternative desalination technology with a reasonably lower cost and higher water recovery [5, 6, 7, 8, 9, 10]. The driving force in FO processes can produce water recovery of up to $\sim 85\%$ in seawater desalination which is significantly higher than the observed recovery in RO processes [11]. The lower energy requirement of FO-based membrane processes

1

have made them more attractive in an energy constrained environment. Although bench- and pilot-scale investigations have shown great promise for full-scale implementation of FO processes, the underlying transport and fouling mechanisms have not been fully explored. From a practical perspective, is it important to understand these mechanisms at the micro- and macro-scales to be able to engineer membrane properties and optimize process conditions to enhance the performance of FO systems.

The limitations in current membrane-based processes can be resolved through the development of advanced membrane materials with enhanced water flux and lower fouling propensity. Recently, carbon nanomaterials (CNMs) have found widespread applications in different fields due to their unique structural and physical properties. Carbon nanotubes (CNTs) can provide high flow rate of water when used as channels for water transport due to "hyperlubricity" effect [12]. Graphene with nanopores, otherwise known as nanoporous graphene (NPG) have exhibited high desalination performance, providing water flux several orders of magnitude higher than conventional RO membranes [13]. CNMs have also shown great adsorptive capacity for natural organic matter (NOM) under various treatment conditions [14]. The preferential sorption of NOM onto CNMs could lead to excessive fouling and potentially limit the full-scale implementation of CNM-based membranes in advanced water treatment systems. These observations highlight the need for extensive investigations into the fouling mechanisms of CNMs in order to fully assess the feasibility of CNT and NPG desalination membranes.

Recently, molecular dynamics (MD) simulations have become an effective tool for studying water and salt transport mechanisms in membrane-based water treatment processes. The results based on some available literature have indicated fair agreement of simulation results with experiments [15]. Although the consistency between simulation results and experimental data is encouraging, the missing link between molecular level simulations and process level models continues to limit the full-scale implementation of the outcome of such simulations. This study seeks to implement a multiscale framework

2

capable of connecting MD simulations to the process level and making predictions at the full-scale. The implementation of such a framework will link MD simulations to the process level and enable direct comparison of simulation results to experimental data within the time scale of experiments.

1.2 Objectives and scope

The development of sustainable and efficient membrane treatment processes requires a combination of theory, experiments, and modeling. Next-generation state-of-the-art membranes are expected to overcome the permeability and fouling limitations in conventional membranes to achieve high water flux and antifouling capabilities. An in-depth understanding of the mechanisms governing water and salt transport in membranes is critical in the development of novel strategies for flux enhancement and fouling control.

In recent times, the advancement in computational modeling has broadened the application of molecular level simulations in membrane-based water treatment processes. Nevertheless, the complexity and interrelationships between different membrane-based transport mechanisms are still not well understood. A major challenge with interpreting and implementing the outcome of MD simulations is the absence of a well-developed framework to connect simulation results to the full-scale. A review of the related literature on the applications of MD simulations in membrane processes shows relatively little focus on developing such a framework. Within this context, the goal of this study is to implement a multiscale framework that connects molecular scale simulations to the process level in order to establish a link between MD simulations and macro-scale experiments. The results of the current work is transformative because adopting a multi-scale modeling approach will provide an avenue for integrating simulation outcome into full-scale models to elucidate membrane-based transport mechanisms at the micro- and macro-scales.

The first objective of this study is to establish a criterion for estimating pure water permeability in pressure-driven membranes using a probabilistic approach. It is hypothesized

3

that the use of Bayesian inference will provide an effective model updating process based on prior knowledge to capture realistic distributions of the membrane permeability at the molecular scale. MD simulations are performed using different membrane configurations to obtain data for updating a probabilistic model to estimate membrane permeability. Moreover, considering the vast information that can be obtained from MD simulations, fundamental questions such as the time length of simulations and number of replicate simulations required must be answered prior to data analysis and interpretation. The convergence of the model is assessed to ascertain realistic simulation time lengths and number of replicate simulations required to reach stationary state. The estimated membrane permeability is used to predict full-scale water flux by means of a process level Monte Carlo simulation.

The second objective is to implement a multiscale modeling framework to scale up MD simulations. The hypothesis of this task is based on the fact that membrane parameters such as permeability and diffusion coefficients obtained from MD simulations can be used for full-scale predictions to reflect process level conditions. A process model describing a FO system within the construct of MD is developed to connect the molecular domain to the process level and to extract membrane parameters from the MD simulations to make full-scale flux predictions.

The third component of this study is to evaluate the desalination performance and NOM fouling propensity of pristine and functionalized NPG membranes using MD simulations. Although water recovery in NPG membranes is expected to be high, excessive fouling could result in significant decline in the water recovery rate. It is anticipated that selective functionalization of NPG membranes could impact membrane-foulant interactions and potentially offer a means to strategically control NOM fouling in NPG membranes. Pressure-induced flux simulations are conducted to estimate water permeability and salt rejection in the membranes. Umbrella sampling simulations are further performed to probe the fouling propensity of different functionalized NPG membranes.

4

1.3 Dissertation overview and organization

The overall goal of this study is to elucidate water and salt transport mechanisms and the effects of water chemistry conditions on membrane processes using a multiscale modeling approach. The specific tasks in this study are mainly accomplished through the use of MD simulations and process level modeling. Prior to the simulations, the appropriate molecular models for the membranes, solvents, and foulant layers are generated to adequately represent their experimental structure and properties. In the case of the functionalized NPG, surface functionalization is performed by attaching different functional groups to the pores of a pristine NPG membrane. Pressure-induced simulations are conducted to evaluate water and salt flux across CTA and NPG membranes. Osmotic water transport is also simulated to evaluate water transport across the CTA FO membrane. The strength and nature of membrane-foulant interactions are probed using umbrella sampling simulations. Based on the results of MD simulations, membrane parameters are estimated to make predictions at the full-scale using a process model. The full-scale model setup is based on relevant experimental conditions to reflect process level observations.

The organization of the dissertation is as follows: Chapter 1 presents a brief introduction and discusses the motivation and overall significance of this study. Chapter 2 focuses on reviewing related literature and background information as part of highlighting some of the significant studies in this area. The remaining chapters present independent studies on the main tasks of this study. Chapter 3 discusses a probabilistic approach for estimating pure water permeability in pressure-driven membranes. In Chapter 4, a multiscale framework based on molecular and process level modeling is presented to connect MD simulations to the bulk to provide a means to scale up molecular level simulations. Chapter 5 focuses on investigating water permeability, salt rejection and NOM fouling in NPG membranes using MD simulations. Chapter 6 presents a summary of the dissertation and the relevant conclusions drawn from the individual studies as well as recommendations for future work.

5

CHAPTER 2

BACKGROUND AND LITERATURE REVIEW

2.1 Overview of molecular modeling

In recent times, the use of molecular modeling for studying environmental systems has increased with specific applications in water quality modeling, reaction kinetics, adsorption studies and membrane filtration processes. Molecular modeling methods ranging from *ab initio* to coarse grain (CG) MD simulations have been extensively applied in environmental systems analysis and modeling. Figure 2.1 shows a general overview of molecular modeling methods. Quantum mechanics (QM) methods such as Hatree Fock (HF) and Møller-Plesset perturbation theory (MP) explicitly account for electron and nuclei interactions to mimic the behavior of atoms. In molecular mechanics (MM), atoms are considered as point masses in space and a set of potential energy functions known as force fields are used to describe the interactions between the atoms. QM methods are usually the most ideal for studying processes involving reaction kinetics, transition state and charge transfer. These methods provide the highest level of accuracy in describing atomic interactions but can also be computationally expensive even on the most powerful high performance computers. For instance, computational time varies to the fourth power of the basis set size for HF methods. Density Functional Theory (DFT) describes the electronic interactions between atoms using density functionals and are usually less computationally expensive compared to wave function methods. As one moves from left to right in Figure 2.1, simulations become less computationally expensive at the expense of decreased resolution.

MD simulations utilize classical Newtonian equations of motion to simulate the behavior of atomic scale particles with time. For a given system, both bonded and non-bonded

6
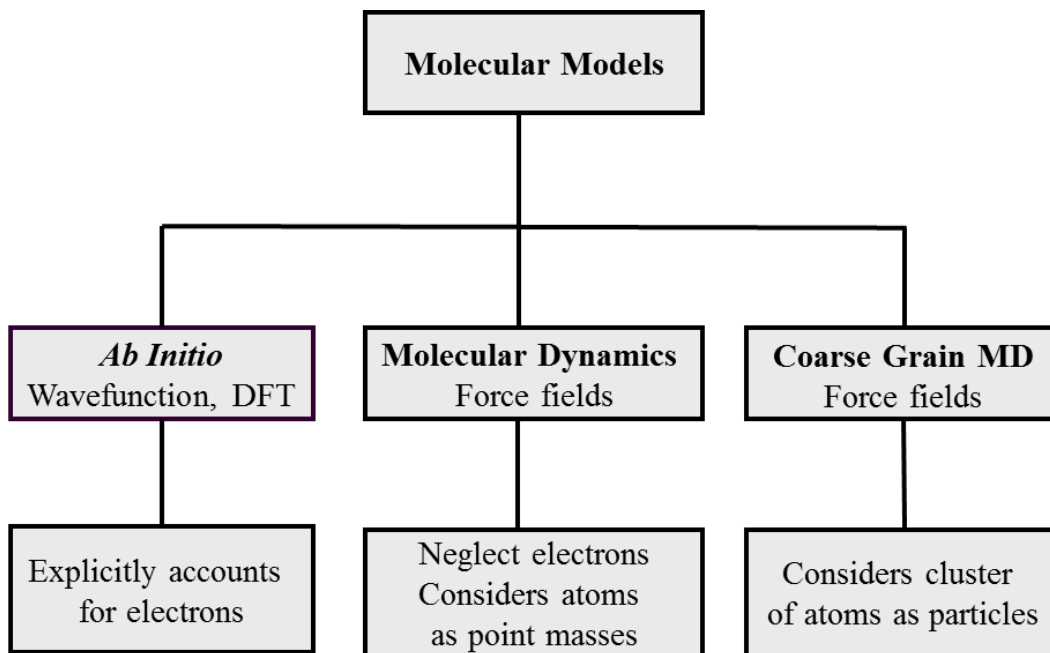
Fig. 2.1   Overview of molecular modeling methods

atom pairs interact and these interactions form the core of MD simulations. Simulations can either be based on QM or MM depending on how the inter-atomic potentials are defined. A combination of QM and MM MD (QM/MM) simulations can also be adopted where a region of the simulation system is described using QM potentials and the rest described with MM potentials. A typical MD simulation usually consists of three steps: initialization, equilibration, and production. Initialization involves setting up simulation preliminaries such as the type of atoms, simulation size, boundary conditions and assigning the initial velocities of the atoms. An initial geometry for MD simulations is usually obtained by collectively moving atoms to a minimum energy point by using some sort of conjugate gradient or steepest decent algorithm to locate the minimum energy conformation on the potential energy surface. In equilibration, MD simulations are conducted to relax the system; a constant volume MD simulation will typically be conducted to equilibrate temperature followed by a constant pressure simulation to allow the solvent to relax with the solute to stabilize the system density. The production stage is usually the data collection phase where the equilibrated system is simulated for a specified number of time

7

steps to obtain trajectories which can be analyzed to study the dynamics of the system under the given conditions.

Depending on the system being simulated and the expected level of accuracy, MD simulations can either be based on implicit or explicit solvation models. Implicit solvation represents solvent as continuum model with average properties for the real solvent with dielectric effect [16]. For instance, a polarizable continuum model usually has some dielectric effect based on the solvent polarity with the positive regions of the solvent accumulating at the negative regions of the solute and vice versa [16]. Explicit solvation models simulate some real properties of the solvent and represent the solvent with discrete solvent molecules. Some of the widely used explicit solvation models for describing interactions between water molecules in solution include TIP3P, TIP4P, and SPC models.

While the accuracy of QM methods is based on the level of theory adopted for the computation, the results of classical atomistic simulations can vary significantly depending on the type of force fields used in describing the interactions between the atoms. Thus the identification of accurate and compatible force fields for various systems is critical in advancing the applications of MD simulations in a wide range of fields.

Despite the advancement in computational modeling, full-scale atomistic simulations are able to handle systems with tens or hundreds of thousands of atoms and at the sub-microsecond time scale. In order to fully study the dynamics of larger systems, longer simulations are required to provide adequate time to observe conformational changes such as self-assembly of biological materials. Recent studies have shown that the use of CGMD simulations can effectively reduce the computational expense by removing both degrees of freedom and interactions from the system [17]. In CGMD, a simplified model of a larger system is built by clustering several subcomponents of a system into one particle [17]. The interactions between the particles are described using force fields. Residue-based CG (RBCG) and shape-based CG (SBCG) are two of the main classes of CG methods that have been extensively tested especially for biomolecular systems. In RBCG , a cluster of

8

10-20 covalently bonded atoms can be represented by a CG bead while SBCG usually have 150-500 atoms per CG bead [17]. RBCG represents sections of a molecule with similar chemical properties and spatial location with a bead and treat the CG system as an ensemble of beads [17].

CG models have been successfully used to study the behavior of proteins and other biomolecular systems and most of the force fields have been developed for such systems. However, properly parameterized force fields can be used to generate a refined CG model of an all atom (AA) structure for a wide range of systems including polymeric membranes and nanomaterials. The application of CGMD in studying macromolecules and polymeric materials has been extensively researched [18, 19, 20, 21, 22]. In the area of small molecule diffusion, Gautieri et al. combined classical and CGMD simulations to develop a multiscale method for predicting diffusivity in polymer matrices [20]. The CG MARTINI force field was parameterized using an atomistic-based method. The extended MARTINI force field was validated and the predicted diffusion coefficients were found to be in agreement with experimental data. The structure of the FT-30 polyamide membrane and its interaction with saline solution was investigated by Hughes and Gale via MD simulations [22]. The structure of the membrane was represented as AA while the polysulfone support layer was coarse-grained to allow greater length and time scales to be simulated. In another study, a new MARTINI model for large-scale simulations of the interaction of fullerene with water, organic solvents, and lipid membrane was proposed and validated [23]. The application of CG modeling in larger systems has provided realistic results, proving to be a suitable option for the simulation of larger polymeric systems at microsecond time scale. CGMD simulations can address the time and length scale limitations in AAMD simulations and can therefore serve as a valuable tool for probing systems at the mesoscopic scale.

2.2 Membrane-based water treatment processes

Low pressure membrane (LPM) processes such as ultrafiltration and microfiltration are extensively used in conventional water treatment systems for the removal of micropollutants [24, 25] based on a size exclusion mechanism. LPMs have high efficacy in producing quality water, coupled with the advantages of smaller footprints requirements and lower cost of operation [25, 26]. Nanofiltration and RO membranes utilize selective permeability to achieve separation of various mixtures under a significant pressure gradient. The applied pressure drives the transport of water through the dense active layer of the membrane while restraining solutes at the feed side to produce water of superior quality. Commercial RO membranes consisting of thin-film composite (TFC) with polyamide selective layer are currently the most established desalination technology [3]. Cellulose acetate-based membranes have also gained widespread application in RO processes due to their ability to resist biofouling in chlorinated systems [27, 28]. The implementation of RO desalination technology is usually energy and capital intensive because of the high hydraulic pressure required to maintain the driving force for water transport. While optimization and membrane redesign can reduce the energy demands of RO systems, fouling of the membrane by organic and colloidal matter can significantly reduce membrane permeability and result in membrane filtration flux decline.

FO membrane technology has been identified as a viable replacement for RO desalination technology as a result of its lower energy demand. FO membranes utilize osmotic pressure as the driving force for water transport and therefore do not require hydraulic pressure to achieve water flux and solute rejection [29]. The driving force for water transport is created by the osmotic pressure gradient between the feed solution (FS) and a draw solution (DS) with a high osmotic pressure. The gradient drives the flow of water from the lower solute concentration region to a region of higher solute concentration. The separation is achieved as a result of the selectivity of the membrane which allows the passage of water but retains solute such as NaCl on the surface of the membrane. As water flows from

10

the FS to the DS, the DS salt concentration becomes diluted which results in an overall decrease in the osmotic driving drive. The diluted DS is passed through a second stage treatment process where the draw solutes are removed to produce fresh water and the recovered draw solutes directed to reconcentrate the DS. A schematic of the FO process is shown in Fig. 2.2.

FO operations usually require the use of a feasible DS with unique properties to ensure easy regeneration with low energy consumption [30, 31]. Notably among these draw solutions include ammonium bicarbonate from which water can be easily regenerated through heating and evaporation of the draw solutes at a temperature of 60°C [32, 33, 34]. In addition, FO processes have lower fouling propensities [35, 36] unlike RO systems where extensive pretreatment may be required. The above factors make FO technology an attractive alternative water treatment process in seawater purification.

A major drawback with the FO process, however, is the issue of concentration polarization (CP), which can significantly reduce the driving force for water transport due to solutes buildup on the membrane surface. CP can be controlled by membrane porous support structure and membrane orientation [37] which may require intensive experimental tests on the characterization of membrane material and processes.
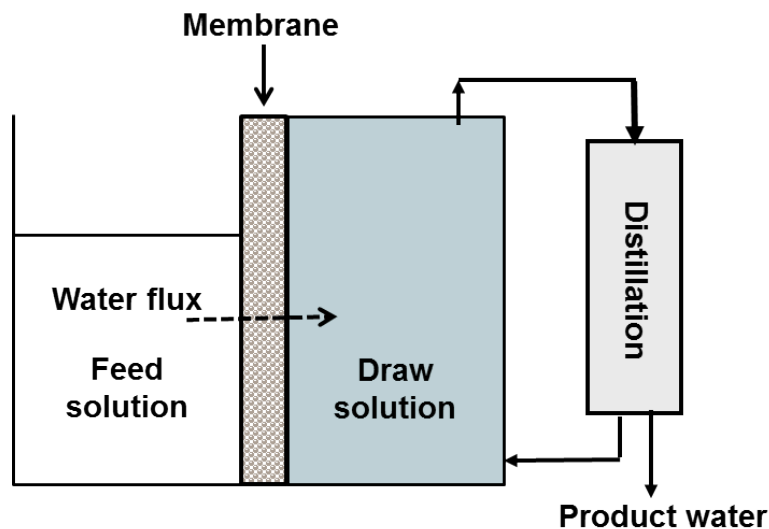
Fig. 2.2   Schematic of forward osmosis system.

11

Although experimental studies can provide useful insight into membrane-based processes, the underlying mechanisms governing such processes occur at the molecular scale and thus cannot be directly probed through macro-scale experiments. MD simulations can provide atomic-scale mechanistic details of water and salt transport in membranes. A recent review has shown extensive applications of MD simulations in studying membrane material properties and molecular transport of water and ions through membranes [38]. Membrane-based processes are typically simulated using either equilibrium or non-equilibrium MD (NEMD) simulation procedures. Equilibrium MD simulations usually involve the computation of transport properties from a system with no chemical potential between the two sides of the membrane [39]. In NEMD, a pressure gradient is created by applying external forces to selected atoms in the feed water [40, 41] or by the use of an external piston [42]. Simulation results based on the available studies have played a critical role in elucidating fundamental mechanisms governing water and ion transport as well as the microscopic interactions between membranes and solutes. The application of MD simulations in studying diffusion, adsorption, fouling and water transport in membranes has provided realistic results which have been in fair agreement with experimental data in some cases.

Luo et al. adopted MD simulations to investigate the relative permeability of salt to water across an atomistic model of the FT-30 RO membrane [43]. Salt permeability across the membrane was estimated based on a solution-diffusion theory using trajectories of a non-equilibrium targeted MD simulations. The reported simulation results were consistent with experimental data indicating the feasibility of using experimental and simulation techniques in studying membrane transport processes. The effect of different casting solutions on water flux and salt rejection in the HTI CTA membrane was investigated by Ong et al. [44]. They reported that CTA membrane casted with dioxane as the main solvent had excellent NaCl rejection but low water flux. It was further observed that, the addition of acetic acid into the casting solution can significantly increase the water flux. Harder

12

et al. estimated the water flux in a polymeric RO membrane using water diffusion coefficients obtained from an equilibrium MD simulation [15]. In another study, Luo and Roux presented a novel and practical method for calculating the osmotic pressure from MD simulations for ionic solutions by introducing an idealized semi-permeable membrane [45]. A method to estimate the flux in membrane channels using MD simulations was proposed by Zhu et al. [40]. A hydrostatic pressure difference across the membrane was established by subjecting bulk water molecules to a constant force and applying a counter force on the supplementary system. Over the course of the simulation, the observed water count across the membrane was small which limits the application of the method to systems with larger pressure differences.

The water flux across a model membrane during NEMD simulations is expected to be low under a typical experimental pressure gradient. Although scaling up the pressure gradient can increase the water count over the course of a simulation, realistic pressure gradients must be simulated in order to obtain results that are representative of experimental conditions.

2.3 Natural organic matter fouling in membrane systems

Preventing excessive membrane fouling remains a major challenge in membrane-based water treatment processes. Natural organic matter (NOM) is a major contributor to membrane fouling and deteriorates the extensive application of membrane processes in advanced water treatment systems. NOM can act as precursors for the formation of disinfection by-products which poses serious health effect. Humic acid (HA) has been identified as the major hydrophobic fraction of dissolved NOM which is usually considered to be responsible for severe membrane fouling [46, 47]. Although FO processes are less susceptible to fouling in comparison to RO systems, high levels of NOM in feed water could limit their extensive application in advanced water systems. NOM fouling can significantly reduce treatment efficiency by causing membrane pore clogging due to formation of a cake

13

layer on membrane surfaces [48, 49, 50, 51] resulting in a subsequent decline in membrane filtration flux [52, 53].

The use of MD simulations can provide unique insight about the molecular mechanisms of NOM interactions with membranes. The interactions of potential foulants (glucose and phenol) with RO membranes was simulated by means of umbrella sampling technique and free energy profiles were generated to probe the nature of the membrane-foulant interactions [54]. A strong association of the foulants onto the membrane was observed with phenol sometimes diffusing through the membrane pores. A similar approach was adopted by Boateng et al. to quantify the adsorptive capacity of CNTs for the removal of endocrine disrupting compounds (EDCs) in aqueous solution [55]. The EDCs indicated favorable interaction with the CNTs under both fresh and saline water conditions. The adsorption of synthetic organic compounds (SOCs) onto CTA and polyamide membranes was investigated using MD simulations in a previous study by Heo et al. [56]. Overall, the adsorption of SOCs onto the CTA membrane was characterized with less favorable binding free energies and lower removal efficiencies compared to the more hydrophobic polyamide membrane suggesting that polyamide-based membranes may be more susceptible to fouling than CTA membranes. The interactions between C_{60} molecules and a humic substance was simulated by Wu et al. [57]. Hydrophobic and $pi-pi$ interactions were identified as the main mechanisms driving the association of the humic substance onto the fullerenes. Recently, the remediation of naphthalene by PAMAM dendrimers and graphene oxide was investigated via experiments and atomistic MD simulations [58]. It was reported that cooperative interactions between naphthalene molecules play a significant role in the association of naphthalene onto dendrimers and graphene oxide.

Water quality parameters including pH and salinity can potentially alter the characteristics of adsorbents and affect the adsorption behavior of NOM. It has been reported that increased ionic strength can enhance the adsorption of organic compounds because of the screening effect of the surface charge produced by high salt content [59, 60]. MD simula-

14

tions have shown that increased calcium ion concentration can cause supramolecular aggregation of NOM fragments into larger colloidal particles [61] which can affect its adsorption behavior. Although NOM hydrophobicity can be associated with its fouling propensity, the exact fouling mechanism is still not understood. Ahn et al. combined experiments and molecular modeling to investigate the possible molecular mechanisms of membrane fouling by NOM in the presence of metal cations [62]. The carboxyl groups of NOM were observed to strongly associate with the divalent Ca^{2+} ions suggesting that divalent calcium ions may facilitate NOM fouling by promoting aggregation of NOM molecules in solution.

2.4 Application of carbon nanomaterials in water treatment processes

The development of sustainable and efficient membrane materials is critical in advancing desalination technologies. The advancement in the nanotechnology field has led to the discovery of various CNMs with unique physical and chemical properties. Fullerenes, single-walled carbon nanotubes (SWNTs), and multi-walled carbon nanotubes (MWNTs) have generated considerable interest in many fields for diverse applications. The use of CNMs in water treatment processes has drawn special research interest in recent years. In the area of water treatment, CNMs have indicated high adsorption capacities for polyaromatic hydrocarbons, heavy metals, and NOM [63, 64, 65]. SWNTs in particular have received considerable attention as a result of their high adsorptive capacity for the removal of EDCs [66, 67, 68, 69]. Reports from recent studies have shown that SWNTs can remove higher quantities of EDCs from various water sources compared to conventional activated carbon [69]. This high adsorptive capacity has been attributed to the presence of "evenly distributed hydrophobic sites" on the surfaces of SWNTs, coupled with large specific surface area and abundant pore size distribution [14]. These properties can enhance the interactions between the surfaces of SWNTs and nonpolar organic compounds, thus making SWNTs a preferred adsorption medium for organic contaminants in water. The underlying adsorption mechanism has been attributed to $\pi-\pi$ electron coupling between the adsorbent and

15

adsorbate molecules [14].

Several studies have adopted various computational techniques to investigate the adsorption mechanisms in CNMs and different adsorbates. The interaction of CNT with benzene and naphthalene was investigated using electron correlated quantum mechanical MP2 method [70]. The binding energy of benzene onto CNT was estimated to be in the range of 2.5-6.0 kcal/mol with preferential sorption on the zigzag (10, 0) CNT over the isoelectronic armchair (5, 5) CNT. Also, the binding energy increased with an increase in CNT length possibly due to the increase in the number of adsorption sites. The adsorption of EDCs onto CNT and the effect of ionic strength on the adsorption were investigated by Boateng et al. by means of umbrella sampling simulations [55]. CNTs exhibited high adsorptive capacity for EDCs under both fresh and saline water conditions. In another study, steered MD (SMD) simulations were conducted to study the transport of anticancer drugs in drug delivery systems [71]. The transport of gemcitabine was studied in an (18, 0) SWNT using SMD. Energy of the drug in its free solvated state was compared to the energy of the drug inside a SWNT. Gemcitabine inside the SWNT was found to have a stronger net solvation than the drug in its free state possibly due to the collaborative interactions between gemcitabine and the surface of the SWNT. Moreover, the cytosine ring of the gemcitabine was found to form a $\pi-\pi$ stacking conformation with the SWNT surface indicating that the drug prefers to locate inside the SWNT.

A wide range of CNMs have demonstrated potential applications for water transport and membrane filtration processes. The flow of water and salt through a regular and a surface-modified CNT under applied pressure was simulated using NEMD simulations [72]. The results showed that a higher water flux and better ion rejection can be achieved through membrane modification. Kalra et al. simulated the osmotically driven water transport through SWNT using MD simulations [73]. The flow of water from the pure-water compartment to a salt-solution compartment by osmotic force was observed within a 180 ns duration. The desalination performance of NPG membranes has been recently investi-

16

gated using MD simulations [13]. Chemical functionalization of NPG pores was observed to have an effect on water transport and salt rejection.

Since water flux scales inversely with membrane thickness, the ultrathin nature of NPG membranes may enhance water recovery and reduce energy demand. With the advancement in nanotechnology and the emergence of various techniques for material modification, NPG sheets can potentially be engineered to boost their application in seawater desalination.

A review of the available literature has shown extensive applications of MD simulations in a wide range of membrane-based water treatment processes. The results based on these studies have elucidated fundamental transport mechanisms in membrane-based processes. Nevertheless, there is relatively little focus on connecting molecular level simulations to the full-scale. This study seeks to implement a multiscale framework capable of connecting MD simulations to the process level and making predictions at the full-scale to provide an avenue to integrate MD simulations into full-scale models.

17

CHAPTER 3

A PROBABILISTIC APPROACH FOR ESTIMATING WATER PERMEABILITY IN PRESSURE-DRIVEN MEMBRANES[1]

Abstract

A probabilistic approach is proposed to estimate water permeability in a cellulose triacetate (CTA) membrane. Water transport across the membrane is simulated in reverse osmosis mode by means of non-equilibrium molecular dynamics (MD) simulations. Different membrane configurations obtained by an annealing MD simulation are considered and simulation results are analyzed by using a Hierarchical Bayesian model to obtain the permeability of the different membranes. The estimated membrane permeability is used to predict full-scale water flux by means of a process level Monte Carlo simulations. Based on the results, the parameters of the model are observed to converge within 5 ns total simulation time. The results also indicate that the use of unique structural configurations in MD simulations is essential to capture realistic membrane properties at the molecular scale. Furthermore, the predicted full-scale water flux based on the estimated permeability is within the same order of magnitude of bench-scale experimental measurement of 1.72×10^{-5}m/s.

Keywords: CTA membrane; molecular dynamics; Bayesian inference; permeability; stationary state; Darcy's law

---

3.1 Introduction

The purification of alternative water sources by membrane separation has become a well-established water treatment technology in recent years. Membrane-based separation processes such as nanofiltration and reverse osmosis (RO) membranes utilize selective permeability to achieve separation of various mixtures under a significant pressure gradient. Currently, thin-film composite (TFC) RO membranes with a polyamide selective layer are most widely used in desalination and purification of seawater and brackish water [3]. TFC-based RO membranes tend to have superior flux and solute rejection rates compared to cellulose triacetate (CTA) membranes [74]. However, CTA membranes have greater resistance to chlorine attack than TFC, and can potentially be used in conjunction with chlorination to suppress biofouling in desalination processes [27, 28]. Commercial CTA membranes developed by HTI (Hydration Technologies Inc., OR) consists of a thin selective hydrophilic CTA active layer which favors water transport and an embedded ultrathin polyester woven mesh support layer to provide mechanical stability [75]. Pure water permeability of the CTA membrane in RO mode has been reported to be $8.58 \times 10^{-21} \mathrm{m}^2$, with a corresponding NaCl rejection of $\sim 98\%$ under an experimental pressure gradient of 2 MPa [56].

The development of improved membrane-based water treatment systems requires extensive experimental investigations to optimize permeate flux and solute rejection, which are the two main criteria that characterize the efficiency of pressure-driven membranes. Within this context, several studies have focused on developing high performance TFC membranes with enhanced water flux and high salt selectivity [76, 77, 78]. Extensive experimental studies have also been conducted to study the transport of water and ions across membranes and the influence of fouling on water flux [56, 79]. These experimental studies have provided useful insight into the processes governing water and salt mobility in membranes and the macroscopic interactions between membranes and solutes. Despite the advancement in membrane-based treatment technology, relatively little is known about the molecular mechanisms of water and salt transport across CTA membranes. These trans-

19

port processes occur at the molecular scale and thus cannot be directly probed through macro-scale experiments.

Over the past few decades, atomistic simulations have been used to investigate the mechanism of water and salt flux in polymeric materials [80, 81, 15, 22, 43] and carbon nanotube membranes [82, 83]. A novel heuristic, molecular dynamics (MD)-based approach was developed to construct the atomic model of the FT-30 aromatic polyamide membrane to investigate molecular level transport processes across the membrane [15]. Salt permeability in the membrane was calculated based on a solubility-diffusion theory using trajectories of a non-equilibrium targeted MD simulations [43]. In a related study, the diffusivity of water within the FT-30 RO membrane was estimated from equilibrium MD simulations [15]. Water flux across the membrane was calculated based on linear response theory and Fick's law. Recent applications of MD simulations in membrane-based water treatment processes have shown consistency between simulation results and experimental measurements [15]. The fair agreement of simulation results with experimental data potentially offers a useful route for the development and optimization of membrane processes.

Although equilibrium MD simulations can adequately capture molecular mechanisms in membrane-based transport processes, the use of non-equilibrium MD (NEMD) simulations provides a means to create pressure gradients across membranes to realistically simulate pressure-driven systems. Pressure gradient in NEMD simulations is typically created by applying external forces to selected atoms in the feed water [40, 41] or by the use of an external piston [42].

Considering the vast information that can be obtained from MD simulations, fundamental questions such as the time length of simulations and number of replicate simulations required must be answered prior to data analysis and interpretation. The goal of this study is to establish a criterion for estimating pure water permeability in a CTA membrane by means of Bayesian inference. Water transport across a CTA membrane is simulated in

20

RO mode and the membrane permeability is estimated by updating a Hierarchical Bayesian model using data from the MD simulations. The convergence of the model is assessed to ascertain realistic simulation time lengths and number of replicate simulations required to reach stationary state. The estimated membrane permeability is used to predict full-scale water flux by means of a process level Monte Carlo simulation. The use of Bayesian inference provides a means to incorporate prior knowledge in the model updating process based on experience and experimental data. The results of this work can potentially provide insight into the estimation and scale up of water flux in pressure-driven systems.

3.2 Computational methods

3.2.1 Atomistic model of HTI CTA membrane

The active layer of the simulated membrane consists of 4 CTA polymer chains with each chain containing 30 repeating CTA units. The initial structure of the CTA monomer was generated in Gaussview [84] and optimized with dispersion-corrected density functional theory [85, 86] at the BLYP/6-31++G(d,p) level using TeraChem [87, 88]. A CTA polymer chain was created by sequencing 30 CTA monomers using the dendrimer builder toolkit (DBT) [89]. DBT is integrated with the AMBER MD package [90] and assigns partial charges of the atom based on AM1-BCC charges generated in Antechamber. An atomistic model of the CTA membrane was constructed to match the experimental density of $1.34 \, \text{g/cm}^3$ and a polymer content of 50% by volume [75, 44]. A $49.3 \, \text{Å} \times 49.5 \, \text{Å}$ graphene sheet was generated using the nanotube builder package in Visual Molecular Dynamics (VMD) [91] by following procedures outlined in a previous study [55]. All subsequent simulations after the membrane construction were performed with the NAMD MD package [92] using CHARMM force field [93, 94]. The thermostat was regulated using Langevin dynamics with a collision frequency of $2 \, \text{ps}^{-1}$. All bonds involving hydrogen atoms were restrained to their equilibrium value using the SHAKE algorithm [95]. A Particle Mesh Ewald [96] was used to compute the long-range electrostatic interactions and periodic

21

boundary conditions were applied in all directions. The non-bonded interactions were subjected to a switching cutoff distance of 12 Å. An integration time step of 1 fs was employed in all simulations.

Initially, 4 CTA polymer chains were randomly located in a large cubic box and minimized for several cycles. This was followed by an NPT simulation at an elevated temperature (600 K) and pressure (0.1 GPa) to allow the polymer chains to fold. The folded polymer chains were gradually compacted into a periodic cell of size 49.3 Å × 49.5 Å × 36.5 Å with a confined thickness of 36.5 Å in the z-direction. An annealing MD simulation was performed repeatedly in 1 ns sequence by heating the CTA film to 600 K and cooling to 300 K under an ambient pressure of 0.1 MPa to generate different membrane configurations for the simulations. The CTA film was finally immersed in a TIP3P water box to achieve a hydrated CTA membrane with the target system density of 1.17 g/cm^3. Fig. 3.1 shows the steps involved in generating the CTA membrane.
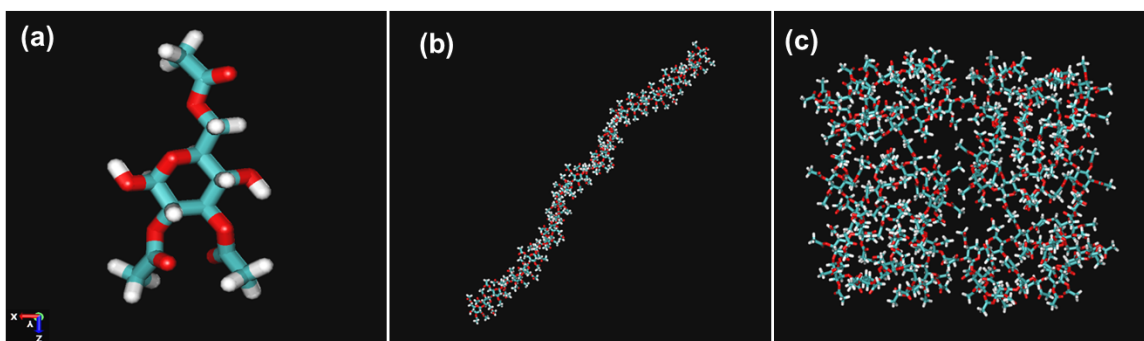
Fig. 3.1   CTA membrane construction process (a) CTA monomer (b) CTA polymer chain (c) CTA membrane model.

3.2.2   Pressure-induced water flux simulations

The setup for the pressure-induced water flux simulations was constructed by locating a TIP3P water box with xy dimensions of 49.3 Å × 49.5 Å and an extended dimensions of 90 Å and 45 Å along the -z and +z axis of the hydrated membrane, respectively. An external piston in the form of a graphene sheet was located at the -z boundary to create a

pressure gradient across the membrane during the simulations. The system was minimized for 1000 steps and equilibrated under the NPT ensemble for 1 ns at 300 K and 1 atm pressure, followed by a 1 ns NVT equilibration. Replicate simulations based on different membrane configurations were conducted in the NVT statistical ensemble (T=300 K) and the trajectories were saved at 10 ps interval for analysis. Water transport in the +z-direction was induced by applying a 0.024 kcal/mol external force on the carbon atoms of the graphene piston. The total external force resulted in an applied pressure of 60 MPa across the membrane. During the simulations, the membrane was held fixed along the z-axis using harmonic restraints to avoid translation of the system along the direction of the external forces.

3.2.3 Probabilistic modeling

Probabilistic models are used for modeling the uncertainty associated with observable data. Two different approaches can be adopted in these type of models: frequentism and Bayesianism. From the frequentist's point of view, data is considered repeatable and the underlying model parameters remain fixed. The source of uncertainty is usually epistemic or aleatory. Epistemic uncertainty is due to the lack of knowledge about the process that is observed and can be reduced as knowledge is discovered. Aleatory uncertainty cannot be reduced because it is the inherent "randomness" of experiments. The Bayesian however looks at the problem in a conceptually different way. A Bayesian's interest is in finding the probability of parameters and models by observing data and considering prior information. The analyst's initial belief on model parameters is first elicit using prior probability density functions (PDF) and is updated by observing new evidence. The Bayesian assumes that the uncertainty in the parameters is only epistemic and it can be reduced as new knowledge about the process is discovered, and more and high quality data is acquired [97].

The method discussed here follows a two-step approach. First, a PDF of the water flux is estimated using a hierarchical Bayesian model. A hierarchical model is chosen because

23

they can properly fit large amount of data due to the number of model parameters, without causing over-fitting as a result of the dependencies enforced by probabilistic relationships [98]. The parameters of a hierarchical model are represented by probability distributions with their own parameters, or hyper-parameters. The second step consists of estimating the PDF of the permeability based on Darcy's law. The PDF of the model parameters are used in this estimation.

The general Bayesian equation used to update the parameters, θ given a set of data D is used for the first step [99]:

$$p(\theta|D) \propto p(D|\theta)p(\theta) \tag{3.1}$$

where $p(\theta)$ is the prior PDF of the model parameters, $p(D|\theta)$ is the likelihood, and $p(\theta|D)$ is the posterior PDF. The prior expresses any knowledge about the parameters before the updating process is performed, while the likelihood expresses the probability of the data, D given a set of parameters, θ. The posterior PDF can be understood as an updated probability of the parameters, θ after considering (or given) the data, D. The data used in this study is obtained by NEMD simulations which calculate piston displacements, z (Å) at specific times, t. Therefore, the data used for updating is $D = \{z_1, z_2, \ldots z_n, t_1, t_2, \ldots, tn\}$, where n is the number of simulations performed. The parameters, θ depend on the probabilistic model used to represent the NEMD simulations. In this particular implementation the model is given by:

$$z_{i,j} = J \times t_{i,j} \tag{3.2}$$

where J is a random variable representing the water flux (Å/ns) and $t_{i,j}$ is the $j-th$ time value (ns) for the $i-th$ simulation. The proposed hierarchical model for this study represents J with a normal distribution using the mean and standard deviation as hyper-parameters. The flux is always positive therefore the prior of J is defined by

24

$$J \propto \begin{cases} N(\mu_J, \sigma_J) & \text{if } J > 0 \\ 0 & \text{if } J \leq 0 \end{cases} \tag{3.3}$$

where μ_J and σ_J are random variables representing the mean and standard deviation of J, respectively. The likelihood $P(D|\theta)$ is assumed to be a Gaussian distribution with zero mean [100]:

$$p(D|\theta) = \prod_{j=1}^{n} \prod_{i=1}^{m} \frac{1}{\sigma_l \sqrt{2\pi}} \exp\left[-\frac{1}{2} \left(\frac{z_{i,j} - \hat{z}_{i,j}}{\sigma_l} \right)^2 \right] \tag{3.4}$$

where $\hat{z}_{i,j}$ is the vector of piston displacements estimated using Equation 3.2, and σ_l is the standard deviation of the likelihood. The value of σ_l is not known and it is considered as a free parameter to be updated. Therefore, the parameters updated are $\theta = \{\mu_J, \sigma_J, \sigma_l\}$.

The selection of priors is critical in Bayesian updating and depends on available knowledge about the parameters. If no information is available, non-informative priors are usually selected [101]. Uniform priors are not always non-informative, for instance, for a linear model, a uniform prior for the slope will be in favor of steeper slopes. This can be easily demonstrated by plotting lines and uniformly increasing the slopes. More lines will be drawn close to 90° [102, 103]. Here, the prior for μ_J is defined as a normal distribution with a mean of 2.5 and standard deviation of 1.25 based on the experience of the analysts and prior bench-scale experiments [56]. A non-information prior for σ_J and σ_l was adopted using Jeffrey's prior [104]:

$$p(\sigma_l) \propto \begin{cases} \frac{1}{\sigma_l} & \text{if } \sigma_l > 0 \\ 0 & \text{if } \sigma_l \leq 0 \end{cases} \tag{3.5}$$

$$p(\sigma_j) \propto \begin{cases} \frac{1}{\sigma_j} & \text{if } \sigma_j > 0 \\ 0 & \text{if } \sigma_j \leq 0 \end{cases} \tag{3.6}$$

The prior used assumes that the parameters are independent such that $p(\theta) = p(\mu)p(\sigma_l)p(\sigma_j)$. This assumption does not limit the posterior to be independent. The posterior distributions is expected to show correlation between parameters if these dependencies are supported by the data [105].

The relationship between permeability and flux given by Darcy's law was used for the second step of the parameter estimation:

$$J = \frac{k\Delta P}{\mu L_{MD}} \qquad (3.7)$$

where, ΔP represents the pressure difference across the membrane (MPa), μ is water viscosity (Pa-s), L_{MD} is the membrane thickness (Å), and k is the membrane permeability (m^2). The NEMD simulations have specific, deterministic values of pressure difference, ΔP, thickness, L_{MD}, and water viscosity, μ. Therefore, the only random variable in Equation 3.7 is J, and the PDF of the viscosity can be easily calculated once the PDF of J is estimated. The model was implemented in Python and the PyMC package was used to draw samples of the posterior using the Metropolis-Hasting algorithm [106].

3.2.4 Extrapolation to full-scale

Monte Carlo simulations were performed to predict the full-scale water flux across the membrane using information obtained from the hierarchical Bayesian model. In predicting the flux, a representative full-scale membrane section with full-scale depth was constructed by assembling rectangular MD membrane prisms. Each prism had an area of 49.3 Å $\times$ 49.5 Å and a depth of 36.5 Å corresponding to the dimensions of the membrane used for the MD simulations. The area of the membrane section corresponds to the area of 500 prisms, and the number of prisms along the depth was varied to correspond to the full-scale depth range of 5-15 μm [75]. The water flux across the membrane section was described using the resistance in series and parallel models and a process level model was subsequently

26

formulated based on Darcy's law [107]. The full-scale flux, J_{FS} was predicted using the following model:

$$J_{FS} = \frac{\Delta P_{FS}}{n\mu L_{MD}} \left[\sum_{1}^{n} \frac{1}{\sum_{1}^{m} \frac{1}{k}} \right] \qquad (3.8)$$

where, ΔP_{FS} represents the experimental pressure gradient (MPa), n is the number of prisms in the x-y plane ($n = 500$), μ is water viscosity (Pa-s), L_{MD} is the depth of a single prism (Å), m is the number of prisms along the thickness of the membrane section, and k is the permeability (m^2) obtained from the flux distribution using Equation 3. Predictions were made based on both deterministic and probabilistic estimates for the membrane thickness. In the probabilistic approach, the thickness was defined as an uncertain parameter by assuming two different distributions.

The remainder of this paper is organized in three parts as follows; the first part discusses the results of the pressure-induced water flux simulations. In the second part, the results of the Bayesian analysis considering all simulation data are presented. The time length of simulations and the number of replicate simulations required to achieve convergence in the permeability estimations are discussed. Finally, results on the predictions of full-scale water flux based on the estimated permeability is presented and compared to bench-scale flux measurements.

3.3   Results and discussion

3.3.1   Water transport across CTA membrane

Simulations have been performed using different membrane configurations obtained from the annealing MD simulations described in section 3.2.1. For each pressure-induced simulation, a hydrostatic pressure difference of 60 MPa was created across the membrane, resulting in a net water flux along the +z-direction. Snapshots of the initial and final configurations of the simulation system are presented in Fig. 3.2. The piston gradually moves

27

over the course of the simulation as water continuously flows from the feed side to the permeate side of the membrane. As shown in Fig. 3.3, the graphene displacements for the different membrane configurations follow a linear trend. Considering the topmost config-
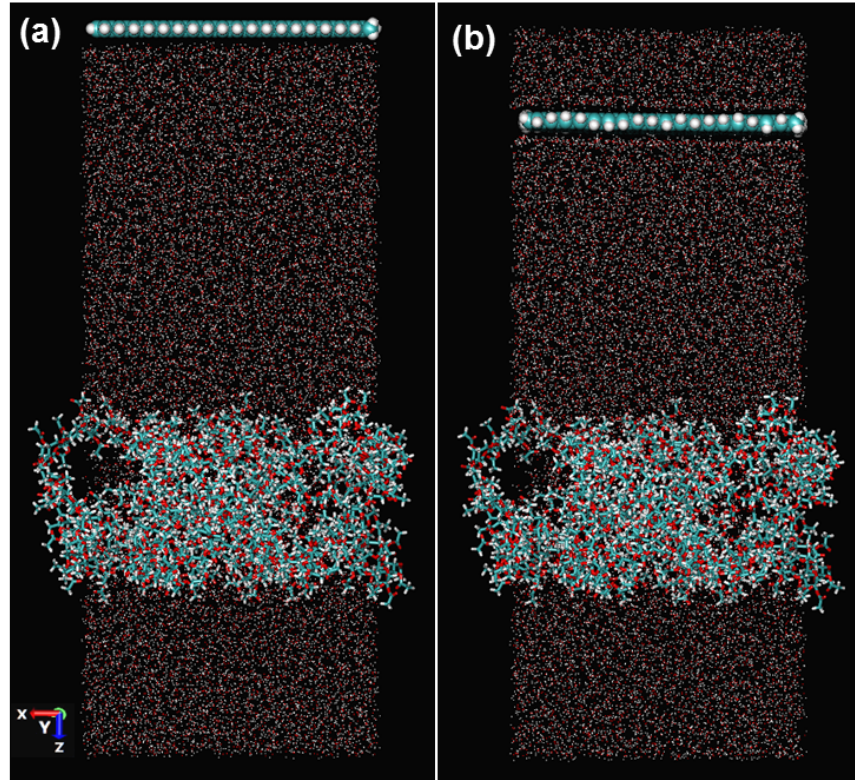
Fig. 3.2 Snapshots of (a) Pressure-induced simulation initial setup (b) Pressure-induced simulation after 10 ns. Membrane is shown in licorice model, graphene is shown in VDW model and TIP3P water molecules shown as points.

uration, an induced pressure of 60 MPa causes a 21.6 Å movement in the piston over a period of 10 ns, which corresponds to a net water flux of 2.16 Å/ns. At the molecular level, water flux across the membrane is computed as the slope of the graphene displacement, which is consistent with experimental procedures where fluxes are measured as mass of permeate collected over a given time period [56].

In a previous study, bench-scale RO experiments were performed to measure pure water permeability of CTA membranes over a pressure range of 0-2 MPa [56], which is significantly lower than the pressure range investigated in this study. At an induced pressure of 2 MPa, the net flux of water across the membrane is prohibitively small and would re-
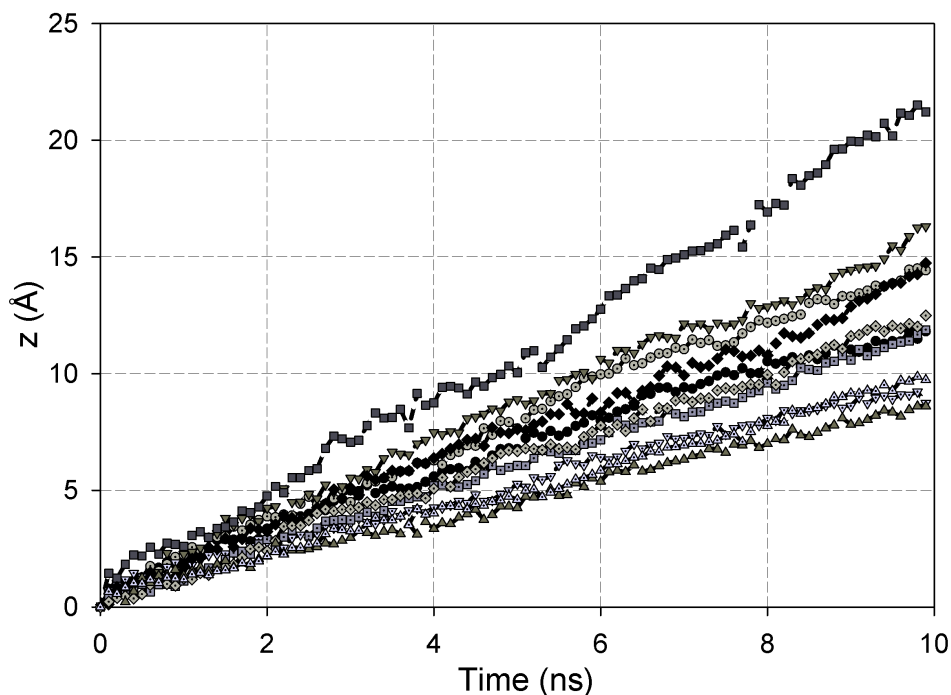
Fig. 3.3   Piston displacements for replicate simulations of different membrane configurations.

quire a considerable longer simulation to yield a significant graphene displacement at the molecular scale. In the present study, a pressure gradient of 60 MPa is sufficient to induce significant graphene displacement over the time frame of the simulations. It must be noted that for a pressure-driven system, the trend of the pressure-flux curve indicates a linear dependence of the pure water flux on the applied pressure [56] suggesting that using higher pressures during MD simulations should not change the underlying membrane permeability.

3.3.2   Estimation of water permeability

Data analysis based on a Bayesian hierarchical model is performed by considering 1000 MD simulation data points for each replicate simulation at a sampling rate of 0.2 ns. The chosen sampling rate was necessary to reduce the computational cost involved in updating the probabilistic model. A few runs with the complete data set confirmed that the effect

of the sampling rate on the results is not significant. Also, the initial 0.2 ns of the MD simulation data are discarded prior to the analysis to achieve pressure equilibration. The convergence of the Markov Chain Monte Carlo (MCMC) chains are assessed by visualizing the chain of each variable, calculating autocorrelations and comparing the variance and mean of different segments of the chain [108]. A typical chain for μ_J with the corresponding histogram and calculated z-score values after 0.5 ns is shown in Fig. 3.4. The chain has 100000 burn in samples, thinning of 10 and a total of 2×10^6 points. Based on the MCMC analysis there is no indication of the chain being "stuck" and the calculated z-scores are all within -2 and $+2$. Similar results are observed for the other random variables of the model (results not shown).

The posterior distribution for permeability, $p(k|D)$ is expected to vary depending on the data provided for model updating. The distribution obtained using a short MD simulation, for example, is expected to have a higher standard deviation compared to the distribution based on a longer simulation.

However, the distribution is expected to converge once "enough" data is provided for model updating. The second part of the study seeks to investigate the effect of different replicate simulations on the model updating. The goal is to determine if replicate simulations based on the same membrane configuration can be used to update the probabilistic model, or if replicate simulations based on unique configurations are needed. This part of the study also focuses on identifying the number of replicate simulations required for the posterior permeability distributions to converge as well as the time length of MD simulations necessary to reach convergence in the posterior distributions.

3.3.2.1 Effect of membrane configuration

Replicate simulations are usually performed to assess reproducibility and to obtain spatial and temporal averaging of simulation results. Conformational changes over the course of atomistic simulations can significantly influence results and data interpretation. For

30
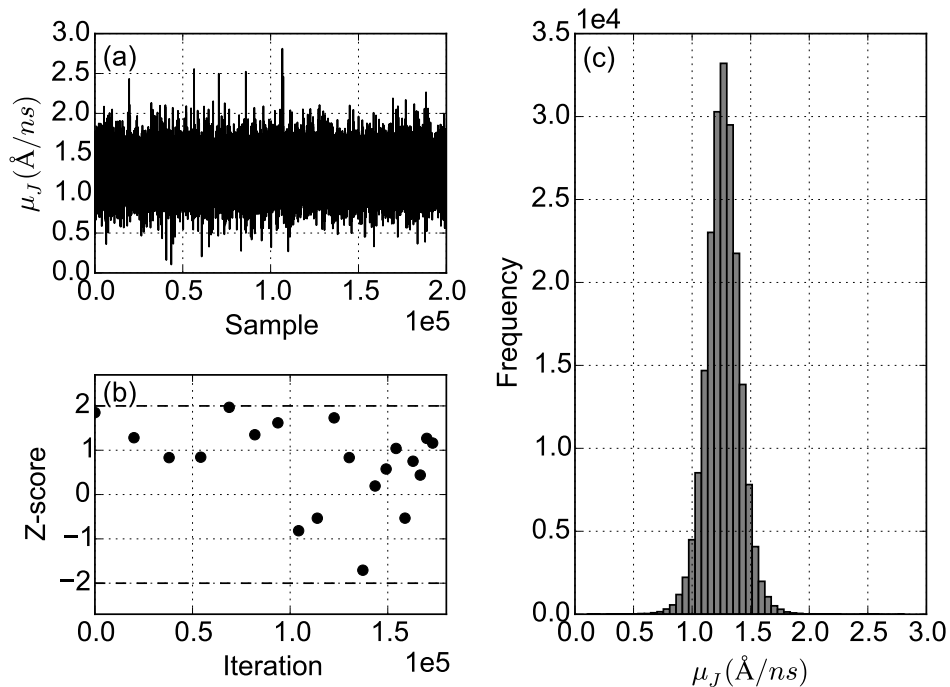
Fig. 3.4   (a) MCMC chain (b) Z-score (c) Histogram of μ_J for 10 different membrane configurations.

instance, conformational changes in membrane structure during flux simulations may directly impact the direction and velocity of water transport across the membrane. State-of-the-art studies of membrane processes at the molecular level have based simulations on single membrane configuration to estimate water and solute permeability across membranes [15, 40, 109]. In other cases, replicate simulations based on single membrane configuration have been conducted and the average results reported with standard deviations. To illustrate the effect of membrane configuration on simulation results, the permeability is estimated by updating the model using data from two sets of simulations; the first set consists of 10 replicate simulations based on a single membrane configuration while the second set consists of 10 single simulations conducted with unique configurations.

In estimating the permeability, data based on three replicate simulations from the first set are first analyzed and data is incrementally added up to a total of 10 simulations. The 95% high probability density (HPD) and the corresponding z-score values are calculated

31

and used as a criteria to assess convergence in terms of the number of replicate simulations required. The 95% HPD describes the entire permeability distribution and represents the area where there is a 95% chance of the permeability. The piston displacements for replicate simulations based on a single membrane configuration are presented in Fig. 3.5. It can
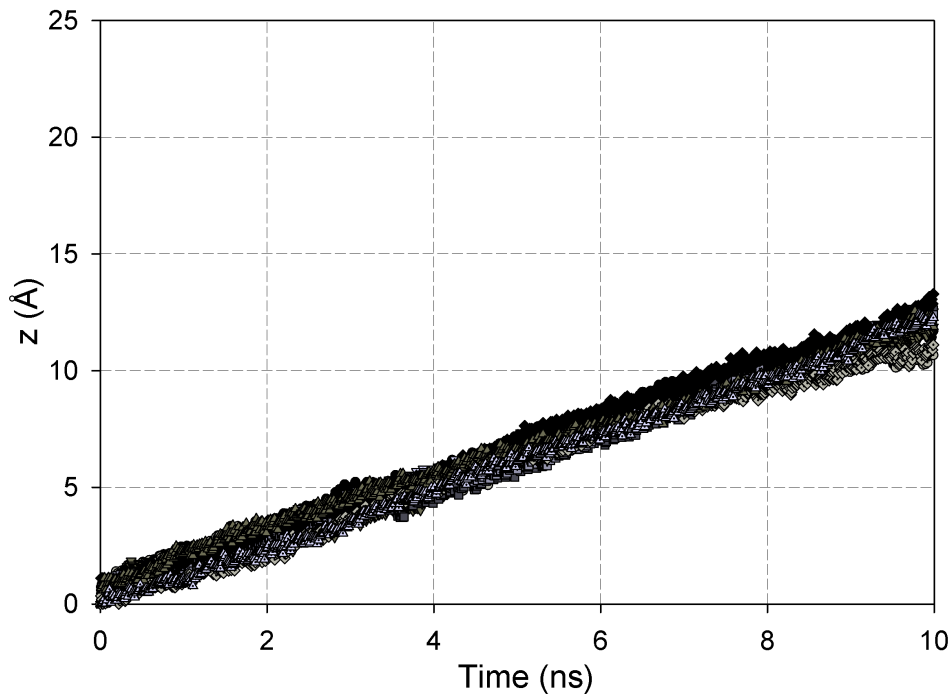
Fig. 3.5   Piston displacements for replicate simulations of the same membrane configuration.

be observed that there is no distinct variation in the graphene displacements over the course of the simulation. The slight variation in the data set is attributed to thermostat effects and other simulation dynamics which are not representative of the intrinsic membrane uncertainty. Fig. 3.6 shows the 95% HPD as error bars, and the mean as a line. The tight 95% HPD region observed further gives an indication that data based on a single membrane configuration does not capture the uncertainty in the membrane properties at the molecular scale. Moreover, as observed in Fig. 3.7, the permeability distributions based on a single configuration show no particular convergence trend because data obtained from the individual simulations are not significantly different and does not provide adequate information

32
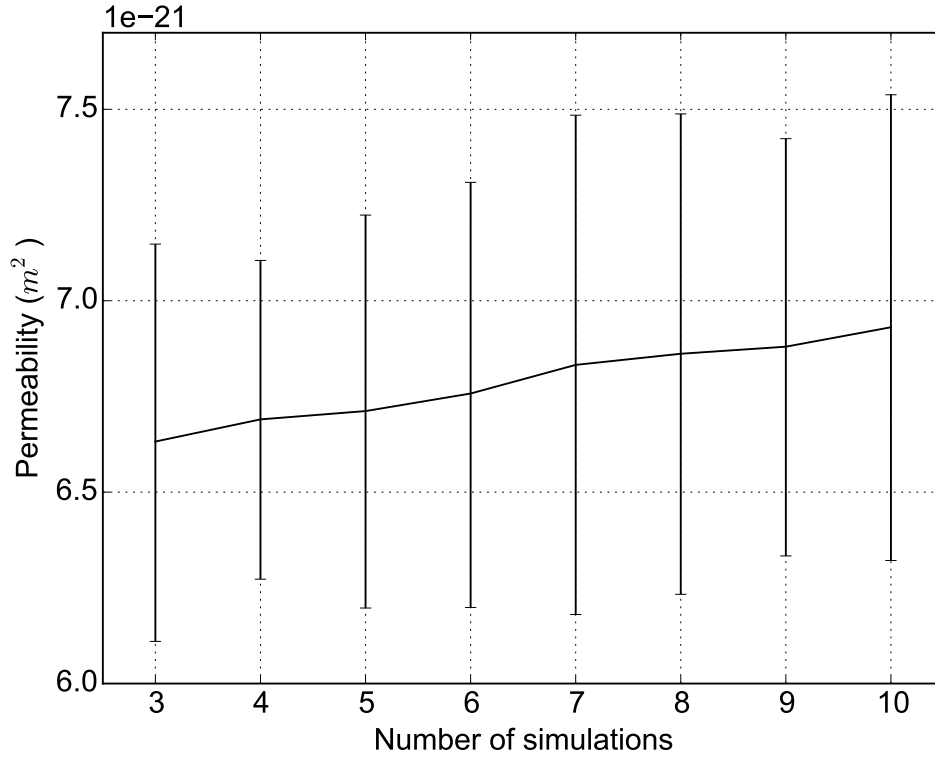
Fig. 3.6   Mean and 95% HPD of permeability for replicate simulations of the same membrane configuration.

on the membrane properties for model updating.

Conversely, as shown in Fig. 3.3, there is distinct variations in the graphene displacements for the replicate simulations based on unique membrane configurations. For instance, a graphene displacement of 21.6 Å is reported for the topmost configuration while the lowest configuration only traveled 8.4 Å despite the identical porosities of the two membrane configurations. This emphasizes the fact that structural rearrangement of the CTA polymer during the annealing process results in the creation of different pathways for water transport. The nature of the pore connectivity dictates the extent of water flow through the various membrane configurations. As further indicated in Fig. 3.8, the permeability distributions tend to converge to a final distribution as the model is updated with data from unique replicate simulations. With only a few replicate simulations, there is a higher standard deviation in the permeability estimates and a larger 95% HPD region as shown in

33
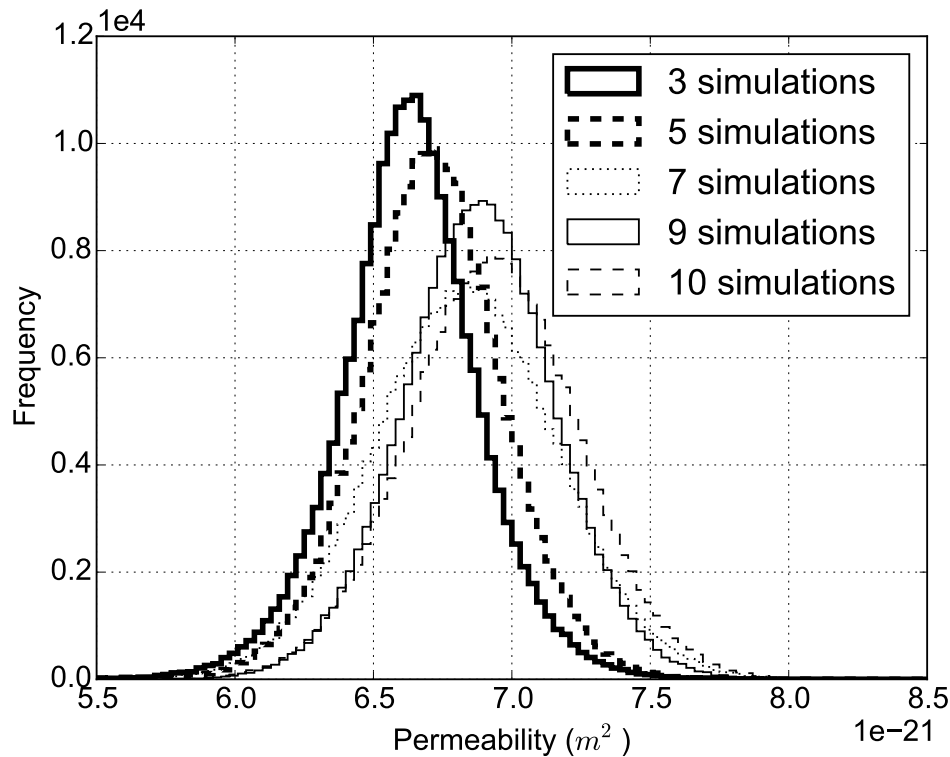
Fig. 3.7   Permeability distributions for replicate simulations of the same membrane configuration.

Fig. 3.9. The permeability estimates become tighter with increasing number of unique replicate simulations. Nevertheless, no significant change in the 95% HPD region is observed beyond eight replicate simulations. Although there seems to be changes in the mean of the permeability estimates up until six simulations, these changes are not significant when compared with the 95% HPD region.

The above observations indicate that the use of unique structural configurations in MD simulations is essential in estimating intrinsic membrane properties via Bayesian updating. Thus single simulations based on different membrane configurations can effectively capture the distributions of intrinsic membrane permeability at the molecular scale.

It is worth noting that despite the convergence in the permeability estimates after eight simulations, the magnitude of the standard deviations are seemingly high compared to the mean estimates. The uncertainty in the permeability estimates is expected to reduce
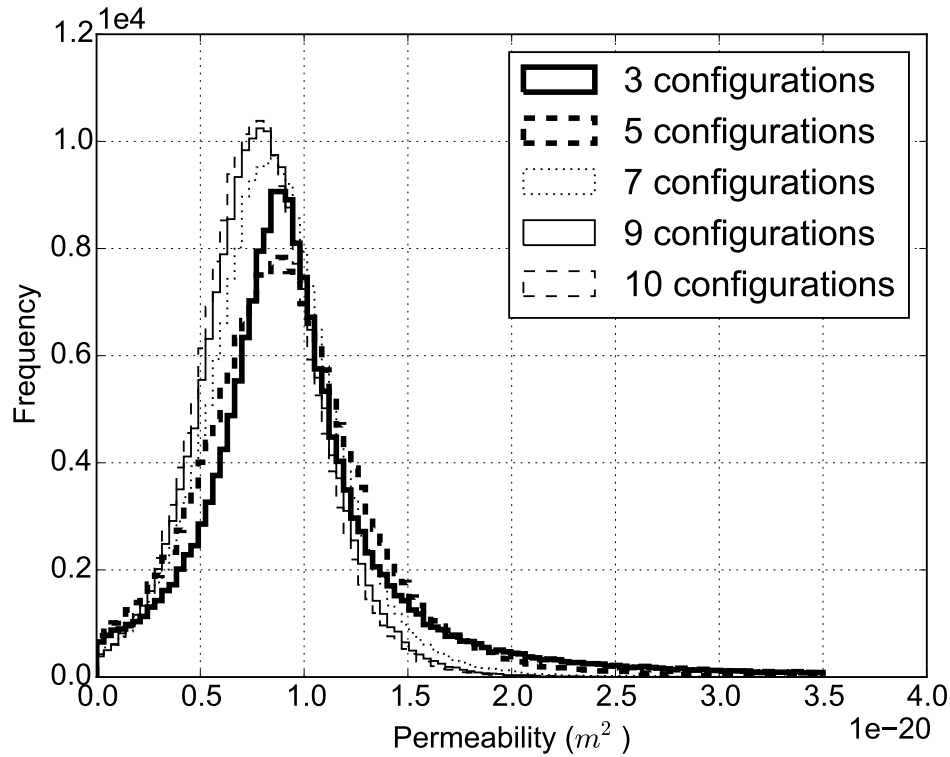
Fig. 3.8 Permeability distributions for replicate simulations of different membrane configurations.

when a bigger simulation size is considered. The time scale of MD simulations usually requires certain compromises to be made on the simulation size in order to simulate certain processes in reasonable computational time. The size of the membrane used in this study is $49.3\,\text{Å} \times 49.5\,\text{Å} \times 36.5\,\text{Å}$, which is several orders of magnitude smaller than the full-scale membrane dimensions. This necessitates the need to scale up molecular level simulations in order to reduce the uncertainty on derived quantities and to make reasonable comparisons with experimental data. In line with this, a process model is adopted to predict the full-scale water flux through the membrane using the estimated membrane permeability.

3.3.2.2 Effect of simulation time

The time length of simulations required to achieve convergence is investigated by updating the model with an increasing number of MD simulations data based on the unique repli-
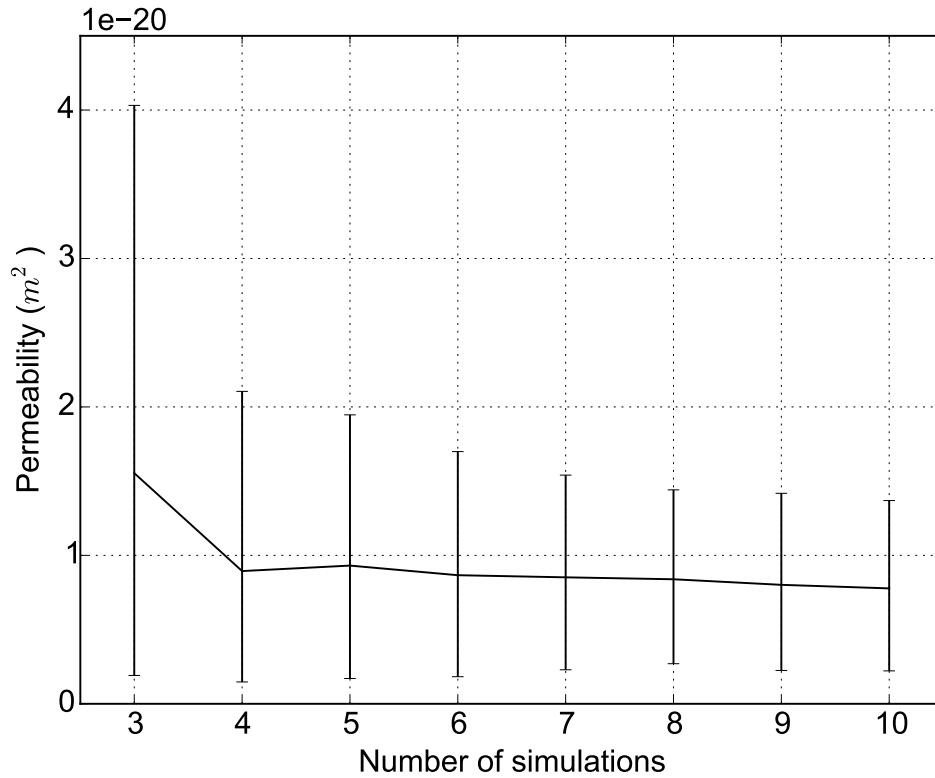
Fig. 3.9   Mean and 95% HPD of permeability for replicate simulations of different membrane configurations.

cate simulations. The posteriori distributions for the permeability are estimated for the initial 0.5 ns of the samples and data is incrementally added up to a total time of 9.5 ns. The histograms for the MCMC permeability samples over a period of 9.5 ns is shown in Fig. 3.10.

At 0.5 ns total simulation time, the mean of the distribution is somewhat close to the mean of the prior, suggesting that information based on a 0.5 ns simulation is not sufficient to change our prior knowledge. As the simulation become longer, the posterior probabilities change based on the prior information and converges towards a final distribution. Based on the molecular scale definition of water flux, it is expected that longer simulations will generate a longer graphene displacement over time and provide more information to accurately estimate the permeability. However, no significant change in the distributions can be observed beyond 5 ns total simulation indicating that the distributions have reached
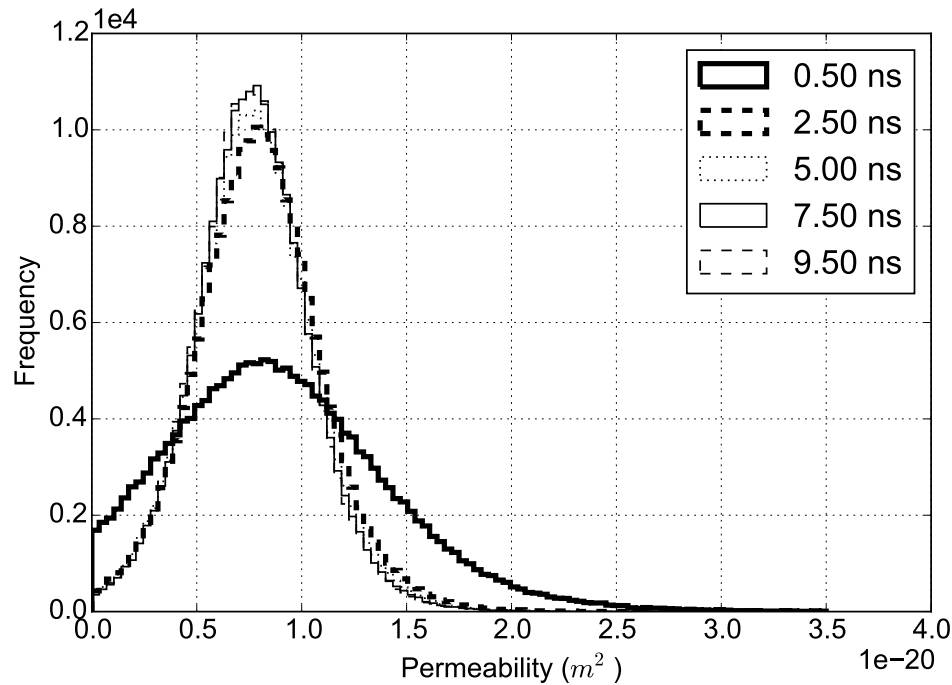
Fig. 3.10 Permeability distributions as a function of simulation time.

a stationary state. As shown in Fig. 3.11, there is a higher uncertainty with corresponding larger 95% HPD region at shorter simulation time. Nevertheless, the mean of the distributions still falls inside the 95% HPD region of the shortest simulation considered. The 95% HPD region is observed to be a little bit more symmetric around the mean, although somewhat skewed. The mean however, did not significantly change over the total simulation time, which indicates that the results are not being biased with some "noise" in the simulations. Overall, the model converges quickly and the permeability estimates become tighter as the simulation becomes longer although the reduction in standard deviation after 5 ns might not be worth the computational time. It is important to also note that the estimated membrane permeability from the Bayesian analysis are in good accord with the reported experimental CTA membrane permeability of $8.58 \times 10^{-21} \text{m}^2$ [56].

37
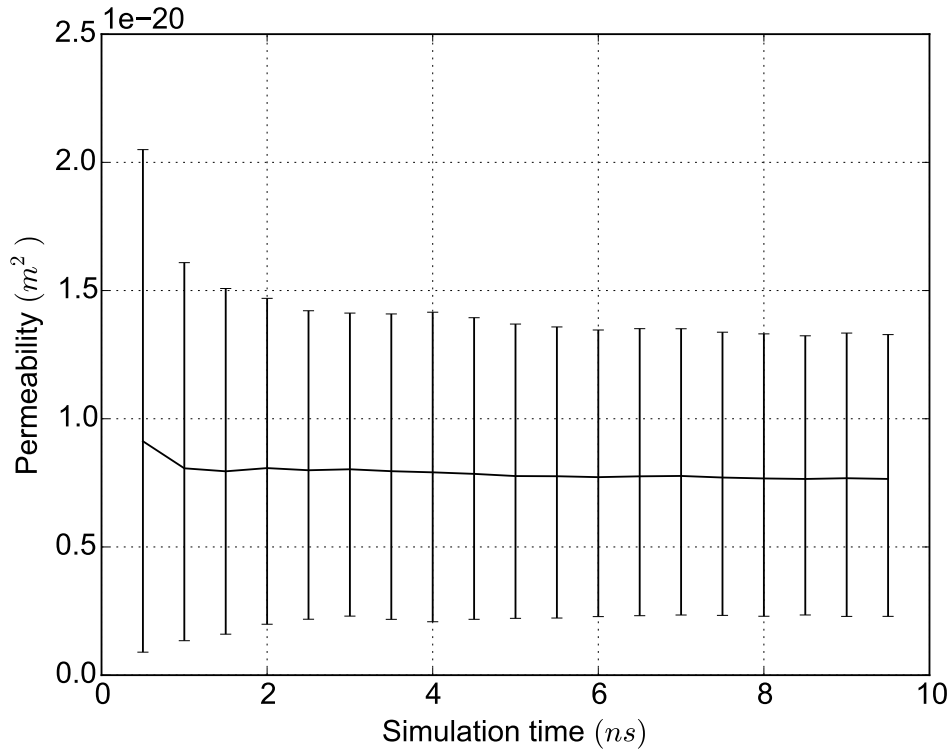
Fig. 3.11   Mean and 95% HPD of permeability as a function of simulation time.

3.3.3   Full-scale flux prediction

The full-scale water flux is predicted based on the hierarchical Bayesian model using the estimated membrane permeability. The probabilistic model is used together with experimental parameters in the process model to make predictions at the full-scale. In a previous experimental study, pure water permeability of the CTA membrane in RO mode was measured using a membrane with an effective area of $0.064 \, \text{m}^2$ over a pressure range of 0-2 MPa. The membrane thickness is considered as an uncertain parameter and it's therefore defined as a random variable in the process model. The full-scale predictions are reported as fluxes in order to make direct comparisons with bench-scale experimental flux measurements. Predictions of the full-scale water flux are initially based on a deterministic definition of the membrane thickness by sampling different thicknesses within the reported range of 5-15 μm. Fig. 3.12 shows the predicted full-scale water flux in comparison with the experimental data at a pressure of 2 MPa shown as a vertical line [56]. As expected,

38

the full-scale water flux scales inversely with membrane thickness because of the greater resistance to flow at increased thickness. The predicted results are within the same order of magnitude of the experimental data despite the uncertainty in the membrane parameters. Although the full-scale predictions are reported as fluxes, the permeability of a given membrane configuration can be obtained using Equation 3; which relates the flux to the permeability by taking into account the applied pressure, viscosity and membrane thickness. In general, the permeability of the membrane is regarded as the inverse of the membrane
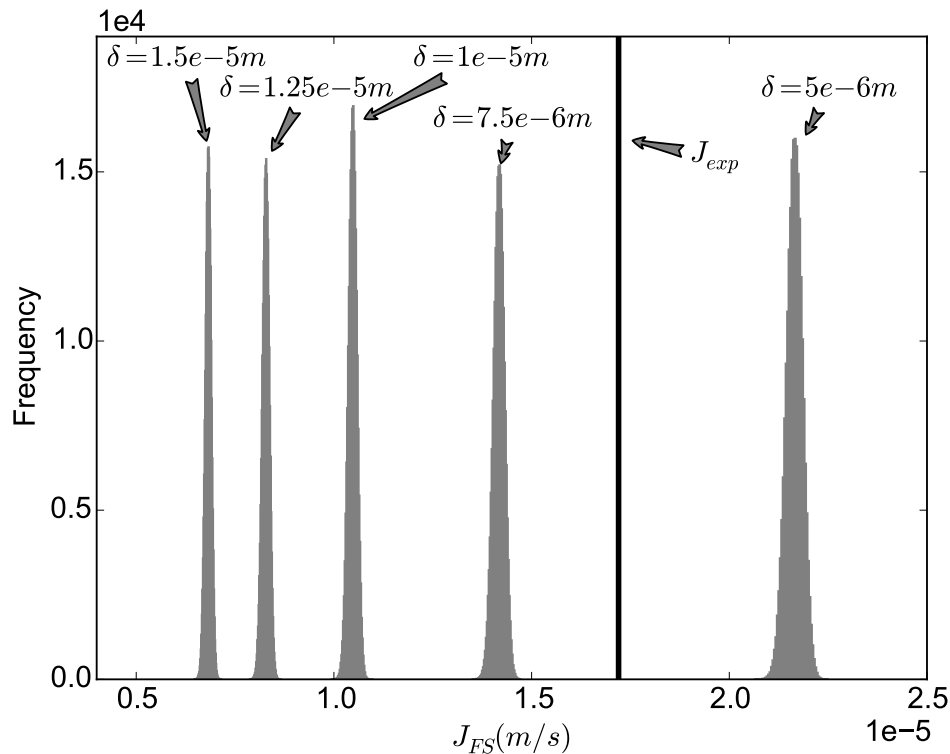
Fig. 3.12   Full-scale water flux prediction based on deterministic membrane thickness.

resistance and indicates the ease with which water crosses the membrane.

In the probabilistic approach, sampling of the membrane thickness is performed within a uniform and a normal distribution. Based on the specified range of the membrane thickness, the uniform distribution is assigned a mean of 10 μm and a standard deviation of 1.66 μm. The full-scale predictions based on the uniform and normal distribution membrane thickness are presented in Figs. 3.13 and 3.14, respectively. As indicated by the

39
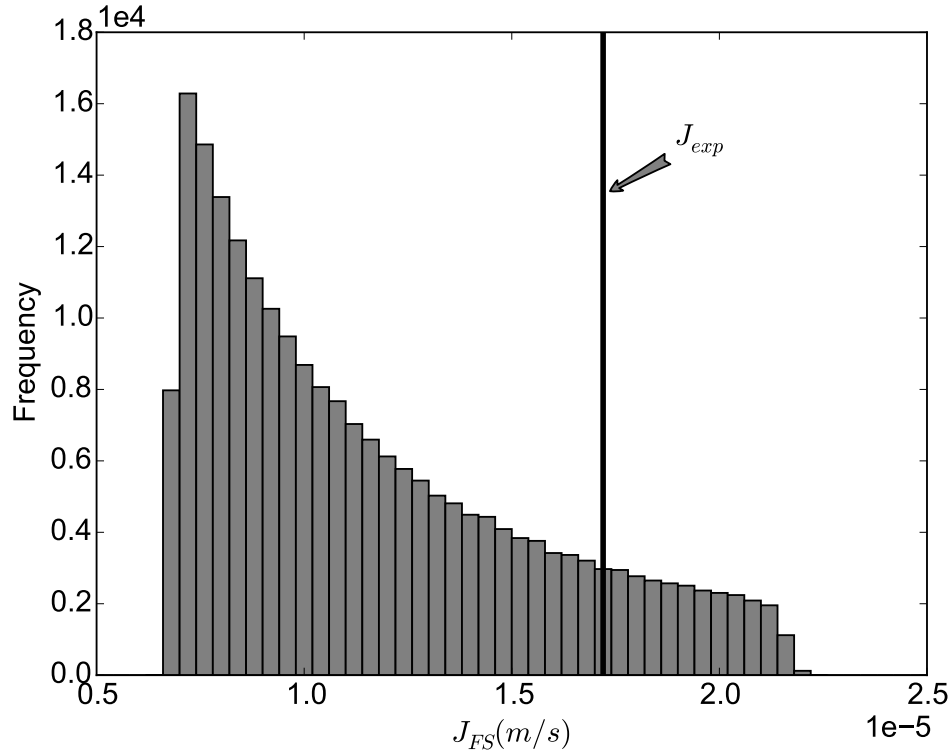
Fig. 3.13   Full-scale water flux prediction based on uniform distribution membrane thickness.

results, the experimental data falls inside the predicted range for both distributions. Although the real distribution for a membrane thickness is unknown, one could argue that a normal distribution would be a better choice to model membrane thickness than a uniform distribution. It is unlikely that the probability density would sharply fall outside the 5-15 μm reported range.

Overall, the full-scale flux predictions based on the different membrane thickness distributions are fairly consistent with the experimental flux measurement, indicating that MD simulations can potentially be scaled up to the full-scale to capture process level conditions. It must be emphasized that the seemingly high prediction error is possibly due to the uncertainty in the estimation of the membrane thickness since the proposed framework allows uncertainties to be incorporated into the process model. Therefore, to reduce uncertainty in the predictions, proper characterization of the membrane thickness is required.
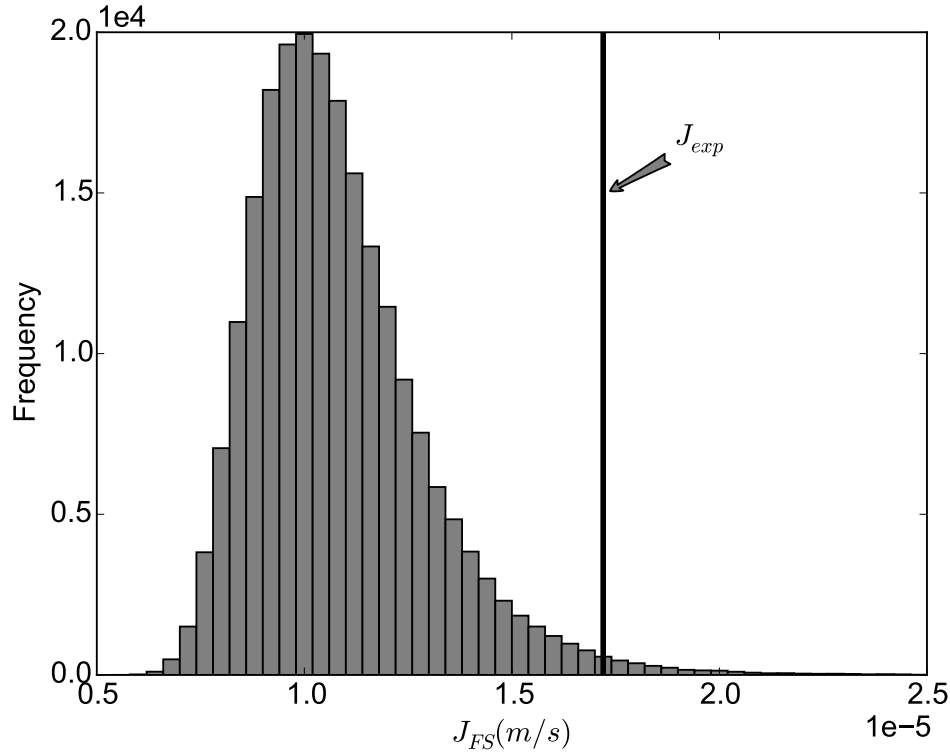
Fig. 3.14   Full-scale water flux prediction based on normal distribution membrane thickness.

3.4   Conclusions

A probabilistic framework to estimate pure water permeability in pressure-driven membranes is presented in this study. The proposed framework uses Bayesian inference to update a probabilistic model using the results of MD simulations. Permeability distributions obtained from the MD simulations was used to predict the full-scale water flux using process level Monte Carlo simulations. Based on the convergence diagnostics, the simulations were observed to reach a stationary state after 5 ns, indicating that a 5 ns total MD simulation is adequate to achieve converged statistics. Replicate simulations of the same membrane configuration indicated a tight estimate of the membrane permeability and did not effectively capture the uncertainty associated with the membrane properties. It was established that MD simulations based on eight unique structural configurations can effectively capture realistic distributions of the membrane permeability at the molecular scale.

41

Moreover, the estimated membrane permeability and the predicted full-scale flux were in good agreement with experimental data despite the uncertainty in the membrane thickness. More accurate prediction of full-scale flux requires detailed characterization of the membrane properties. The presented framework can potentially serve as a useful tool for analyzing and interpreting MD simulations to gain insight in pressure-driven membrane systems. Future work will investigate salt rejection and the influence of natural organic matter fouling on water flux in CTA membranes.

Acknowledgments

Nomenclature

$p(\theta)$ Prior PDF of model parameters

$p(D|\theta)$ likelihood

$p(\theta|D)$ Posterior PDF

z Piston displacement (Å)

J Water flux (Å/ns)

μ_J Mean of flux

σ_J Standard deviation of flux

σ_l Standard deviation of likelihood

k Membrane permeability (m^2)

ΔP Pressure difference across membrane (MPa)

μ Water viscosity (Pa-s)

L_M MD membrane thickness (Å)

J_{FS} Full-scale flux (m/s)

ΔP_{FS} Experimental pressure gradient (MPa)

n Number of prisms in the $x - y$ plane

m Number of prisms along thickness of membrane section

δ Full-scale membrane section thickness (m)

43

CHAPTER 4

MULTISCALE MODELING OF OSMOTIC WATER TRANSPORT AND SALT SELECTIVITY IN FORWARD OSMOSIS MEMBRANES[1]

Abstract

Multiscale modeling of water and salt transport in a cellulose triacetate (CTA) forward osmosis membrane is investigated by means of MD simulations and process level modeling. MD simulations are conducted to simulate osmotic water transport and salt diffusivity, and a process model is formulated to model the FO system within the construct of MD. The results indicate that the driving force for water transport is influenced by dilution of the draw solution and back diffusion of salt across the membrane. Based on the estimates of the membrane permeability and salt diffusion coefficients, the predicted full-scale water flux is within the same order of magnitude of experiments although the predictions approached steady state more rapidly. The difference in the predicted and experimental flux trends is attributed to the different modes of operation in the experimental and modeling setups. Moreover, draw solution (DS) concentration and the type of DS solutes have significant effect on the osmotic driving force, in accordance with experiments. The consistency between model predictions and experiments suggests that MD simulations can potentially be scaled up to reflect process level observations. The presented framework can be useful for studying water and salt transport mechanisms in FO systems.

Keywords: Forward osmosis; CTA membrane; molecular dynamics; multiscale modeling; permeability; salt rejection;

4.1 Introduction

The depletion in global energy resources, coupled with water scarcity in several parts of the world has accelerated the adoption of energy efficient desalination treatment technologies. Efficient and cost-effective treatment methods will serve as a viable means of producing potable water from alternative water sources to meet the world's water demand. Although reverse osmosis (RO) membranes are currently the most widely used commercial membranes in desalination technologies [3], their long term sustainability is uncertain because of their high energy requirement. Forward osmosis (FO) membranes have been identified as an alternative desalination technology with a reasonably lower cost and higher water recovery rate [5, 6, 7, 8, 9, 10]. The driving force for water transport in FO processes is created by the osmotic pressure gradient between the feed solution (FS) and a draw solution (DS) with a high osmotic pressure. The resulting driving force can produce water recovery of up to $\sim 85\%$ in seawater desalination which is significantly higher than the observed recovery in RO processes [11].

Commercial cellulose triacetate (CTA) membranes developed by HTI (Hydration Technologies Inc., OR) contains approximately 14% CTA as the membrane material [75]. The asymmetric FO membrane consists of a thin selective CTA active layer and an embedded ultrathin polyester support layer to provide mechanical stability [75]. The support layer of the CTA membrane consists of polyester fibers and contains spacious voids which minimizes internal concentration polarization (ICP) to enhance permeate flux. Novel asymmetric FO membranes have the ability to reduce fouling and suppress the ICP phenomenon to maintain high water flux and solute rejection [110, 111]. However, bench-scale studies conducted using CTA FO membrane have indicated significant effect of ICP on water flux [56].

Although FO processes are less susceptible to fouling in comparison to RO systems, high levels of natural organic matter (NOM) in feed water could limit their extensive application in advanced water systems. NOM fouling can significantly reduce treatment effi-

45

ciency by causing membrane pore clogging and formation of cake layer on the membrane surface [48, 49, 50, 51] which can result in membrane filtration flux decline [52, 53]. The treatment efficiency of membrane-based processes can significantly be influenced by several other water quality conditions including pH, FS and DS conditions, and temperature. A recent study has shown that increasing temperature can lead to an increased osmotic driving force and an overall increase in water transport [112]. The increased driving force for water transport was attributed to the reduction in water viscosity and ICP across the membrane at higher temperature.

Due to the increasing application of membrane technology for water treatment, a detailed understanding of membrane separation mechanisms have become critical for advancing membrane-based treatment processes. Atomistic simulations can provide atomic-scale details on the mechanisms of water and salt transport in membranes. Recently, the application of MD simulations in membrane-based processes have provided unique insight to elucidate various transport mechanisms and the microscopic interactions between membranes and solutes. The results based on some available literature have indicated consistency between simulation results and experimental measurements. The fair agreement of simulation results with experimental data potentially offers a useful route for combining experimental and simulation results for the development of mechanistic strategies to optimize membrane performance. Such strategies could aim at optimizing process conditions and water quality parameters to minimize membrane fouling and enhance water flux and solute rejection.

Despite the consistency between MD simulations and experiments, there have been relatively little focus on connecting molecular level simulations to the full-scale. One approach is to extract membrane parameters from MD simulations and adopt a process level model to make predictions at the full-scale. The goal of this study is to adopt a multiscale modeling approach to connect MD simulations to the process level. MD simulations are conducted to simulate osmotic water transport and salt rejection in a CTA FO membrane. A process level model is formulated within the construct of MD to extract membrane pa-

46

rameters from the simulations to make predictions at the full-scale. Such a framework will enable reasonable comparison of simulation results to experimental data within the time scale of experiments and potentially provide a means to optimize membrane processes based on simulations and experimental data.

4.2 Computational methods

4.2.1 Atomistic model of HTI CTA membrane

The simulated FO membrane consists of 4 CTA polymer chains, representing the active layer of the membrane with each chain containing 30 repeating CTA units. Based on the manufacturer's specifications, the CTA FO membrane model was constructed to match an experimental density of $1.34 \, \text{g/cm}^3$ and a polymer content of 50% by volume [75, 44]. The starting structure of the CTA monomer was generated in Gaussview [84] and optimized with dispersion-corrected density functional theory [85, 86] at the BLYP/6-31++G(d,p) level using TeraChem [87, 88]. 30 CTA monomers were sequenced using the dendrimer builder toolkit (DBT) [89] to generate a CTA polymer chain. A $49.3 \, \text{Å} \times 49.5 \, \text{Å}$ graphene sheet was generated using the nanotube builder package in Visual Molecular Dynamics (VMD) [91] by following procedures outlined in a previous study [55]. All subsequent simulations after the membrane construction were performed with the NAMD MD package [92] using CHARMM force field [93, 94]. The system temperature was controlled using Langevin dynamics with a collision frequency of $2 \, \text{ps}^{-1}$. All bonds involving hydrogen atoms were restrained to their equilibrium value using the SHAKE algorithm [95]. The long-range electrostatic interactions were computed using Particle Mesh Ewald [96] with all non-bonded interactions subjected to a switching cutoff distance of $12 \, \text{Å}$. Periodic boundary conditions were applied in all directions and an integration time step of 1 fs was employed in all simulations.

The CTA membrane model was generated by randomly locating 4 polymer chains in a large cubic box and performing minimization for several cycles to remove bad contacts.

47

The next step consisted of a 1 ns MD simulation at an elevated temperature (600 K) and pressure (0.1 GPa) to speed up the polymer folding process. This was followed by a gradual compaction of the folded polymer chains into a $49.3\,\text{Å} \times 49.5\,\text{Å} \times 36.5\,\text{Å}$ periodic cell while confining the cell thickness in the z-direction. An annealing MD simulation was performed repeatedly in 1 ns sequence by heating the CTA film to 600 K and cooling to 300 K under an ambient pressure of 0.1 MPa to generate different membrane configurations for the flux simulations. Finally, the CTA film was hydrated in a TIP3P water box to achieve the target system density of $1.17\,\text{g/cm}^3$.

4.2.2 Osmotic and pressure-induced water flux simulations

The setup for the osmotic water transport simulations consisted of the hydrated CTA membrane with 0.25 M NaCl FS and 2.5 M NaCl DS located along the $-z$ and $+z$-directions, respectively. The molar concentration of the solutions were obtained by randomly adding the appropriate number of Na^+ and Cl^- ions into the FS and DS domains. The system was minimized for 1000 steps and equilibrated under the NPT ensemble for 1 ns at 300 K and 1 atm pressure, followed by a 1 ns NVT equilibration. A graphene sheet with similar xy dimensions as the water box was located on top of the FS domain to quantity the osmotic water flux across the membrane. Water and salt transport across the membrane were simulated by performing 100 ns replicate simulations under the NVT ensemble at a temperature of 300 K and 1 atm pressure. The effect of different DS solutes on osmotic water transport was also investigated by performing simulations using a 2.5 M $CaCl_2$ and 2.5 M KCl DS with 0.25 M NaCl FS in each case.

A pressure-induced NEMD simulation was performed to estimate the pure water permeability of the CTA membrane. In the case of the pressure induced-simulations, no salt was added to the FS and DS domains. A hydraulic pressure gradient was created across the membrane by applying a 0.024 kcal/mol external force on the carbon atoms of the graphene piston resulting in an applied pressure of 60 MPa. During the simulations, the membrane

48

was fixed along the *z*-axis using harmonic restraints to avoid translation of the system along the direction of the applied force. 10 ns replicate simulations were conducted under similar conditions and the trajectories were saved at 10 ps interval for analysis.

4.2.3 Membrane fouling simulations

Humic acid (HA) is chosen as a representative NOM foulant to investigate the influence of fouling on CTA membrane permeability. The HA structure is based on the Temple-Northeastern-Birmingham (TNB) molecular model which consists of carboxyl, phenolic and amine functional groups [113]. The initial HA structure was generated and optimized by following procedures described in section 4.2.1. An atomistic model of the hydrated CTA-NOM system was constructed by randomly locating HA molecules on the surface of the CTA membrane to achieve an NOM layer with different thickness. The addition of 10 HA molecules resulted in a relatively porous foulant layer with a thickness of 20.9 Å, while 20 HA molecules created a relatively dense foulant layer with a thickness of 26.3 Å. For the pH under consideration, all three carboxyl groups of the HA molecule were assumed to be deprotonated; Na$^+$ counter ions were added to the solvated system to achieve charge neutrality. The system was equilibrated and the effect of the NOM foulant on pure water flux was quantified by repeating the pressure-induced flux simulation procedures described in section 4.2.2.

4.2.4 Process level model

A triple layer process model is proposed to model the FO system described in section 4.2.2 within the construct of MD. The proposed model accounts for the moving boundary of the graphene sheet and is also applicable to pressure assisted FO systems. Fig. 4.1 shows the process level representation of the molecular domain which is comparable to the MD snapshot shown in Fig. 4.3. The FS and DS domains contain NaCl salt at an initial concentration of C_{FS0} and C_{DS0}, respectively. The graphene sheet is initially located at

49

$x_{DS} = L_{DS0}$ and moves such that $x_{DS} > L_{DS0}$ for $t > 0$, where L_{DS} is the moving boundary domain defining the changes in the length of the DS domain with time. Equivalently, because of periodic boundary conditions, the graphene sheet is also initially located at $x_{FS} = 0$ and the domain of FS decreases with time. A derivation of the key equations for modeling FO membranes within the construct of MD is presented below.
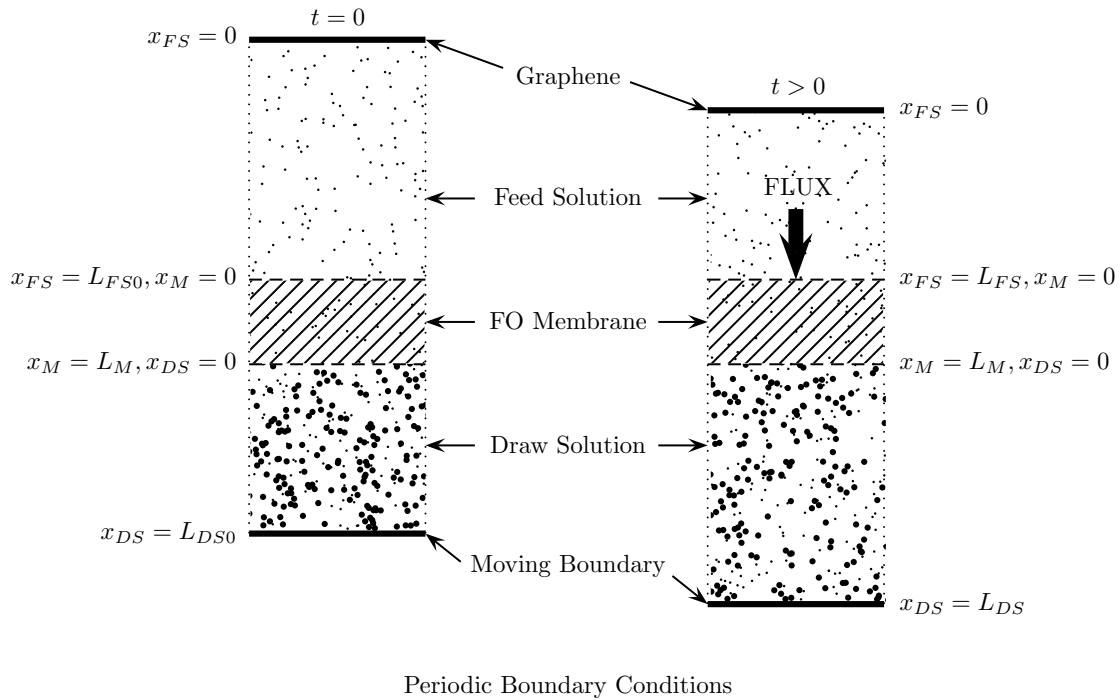
Fig. 4.1   Process level schematic of FO system.

Material balances on the salt in the draw solution (DS), feed solution (FS), and membrane (M) are given by

$$\frac{\partial c_{DS}}{\partial t} + v_b \frac{\partial c_{DS}}{\partial x_{DS}} = D_b \frac{\partial^2 c_{DS}}{\partial x_{DS}^2} \tag{4.1}$$

$$\frac{\partial c_{FS}}{\partial t} + v_b \frac{\partial c_{FS}}{\partial x_{FS}} = D_b \frac{\partial^2 c_{FS}}{\partial x_{FS}^2} \tag{4.2}$$

$$\frac{\partial c_M}{\partial t} + v_M \frac{\partial c_M}{\partial x_M} = D_M \frac{\partial^2 c_M}{\partial x_M^2} \tag{4.3}$$

Multiplying both sides of equations 4.1 to 4.3 by $\frac{L_{DS,0}}{v_{b,0} c_{DS,0}}$ and using $\tilde{C}_i = \frac{c_i}{c_{DS,0}}$ and $\tilde{T} = \frac{t v_{b,0}}{L_{DS,0}}$ where $v_{b,0}$ is the initial water flux across the FO membrane, results in

$$\frac{\partial \tilde{C}_{DS}}{\partial \tilde{T}} + \frac{v_b L_{DS,0}}{v_{b,0}} \frac{\partial \tilde{C}_{DS}}{\partial x_{DS}} = \frac{D_b L_{DS,0}}{v_{b,0}} \frac{\partial^2 \tilde{C}_{DS}}{\partial x_{DS}^2} \tag{4.4}$$

$$\frac{\partial \tilde{C}_{FS}}{\partial \tilde{T}} + \frac{v_b L_{DS,0}}{v_{b,0}} \frac{\partial \tilde{C}_{FS}}{\partial x_{FS}} = \frac{D_b L_{DS,0}}{v_{b,0}} \frac{\partial^2 \tilde{C}_{FS}}{\partial x_{FS}^2} \tag{4.5}$$

$$\frac{\partial \tilde{C}_M}{\partial \tilde{T}} + \frac{v_M L_{DS,0}}{v_{b,0}} \frac{\partial \tilde{C}_M}{\partial x_M} = \frac{D_M L_{DS,0}}{v_{b,0}} \frac{\partial^2 \tilde{C}_M}{\partial x_M^2} \tag{4.6}$$

The dimensionless distance, $\tilde{X}_{DS}$, is related to L_{DS} and the normalized time varying length $\tilde{L}_{DS}$ as follows

$$L_{DS} = L_{DS,0} + \int_0^t v_b \, \mathrm{d}t \tag{4.7a}$$

$$= L_{DS,0} + \int_0^{\tilde{T}} v_b \frac{L_{DS,0}}{v_{b,0}} \mathrm{d}\tilde{T} \tag{4.7b}$$

$$\tilde{L}_{DS} = \frac{L_{DS}}{L_{DS,0}} = 1 + \int_0^{\tilde{T}} \frac{v_b}{v_{b,0}} \mathrm{d}\tilde{T} \tag{4.7c}$$

$$\tilde{X}_{DS} = \frac{x_{DS}}{L_{DS}} = \frac{x_{DS}}{L_{DS,0} \left(1 + \int_0^{\tilde{T}} \frac{v_b}{v_{b,0}} \mathrm{d}\tilde{T}\right)} = \frac{x_{DS}}{L_{DS,0} \tilde{L}_{DS}} \tag{4.7d}$$

Note that $\tilde{L}_{DS}$ is not a function of position x_{DS}. As shown later, v_b is a function of the osmotic pressure, which is determined by the concentration difference across the membrane

51

(i.e., at specific, unchanging boundary locations of x_{DS} and x_{FS}). Using the chain rule, and equation 4.7d, the derivatives of concentration *wrt* x_{DS} are written as

$$\frac{\partial \tilde{C}_{DS}}{\partial x_{DS}} = \frac{\partial \tilde{C}_{DS}}{\partial \tilde{X}_{DS}}\frac{\partial \tilde{X}_{DS}}{\partial x_{DS}} = \frac{\partial \tilde{C}_{DS}}{\partial \tilde{X}_{DS}}\frac{1}{L_{DS,0}\tilde{L}_{DS}} \tag{4.8a}$$

$$\frac{\partial^2 \tilde{C}_{DS}}{\partial x_{DS}{}^2} = \frac{\partial}{\partial x_{DS}}\left(\frac{\partial \tilde{C}_{DS}}{\partial \tilde{X}_{DS}}\frac{1}{L_{DS,0}\tilde{L}_{DS}}\right) = \frac{\partial^2 \tilde{C}_{DS}}{\partial \tilde{X}_{DS}^2}\left(\frac{1}{L_{DS,0}\tilde{L}_{DS}}\right)^2 \tag{4.8b}$$

Substituting equation 4.8a and 4.8b into equation 4.4,

$$\frac{\partial \tilde{C}_{DS}}{\partial \tilde{T}} + \frac{v_b L_{DS,0}}{v_{b,0}}\frac{\partial \tilde{C}_{DS}}{\partial \tilde{X}_{DS}}\frac{1}{L_{DS,0}\tilde{L}_{DS}} = \frac{D_b L_{DS,0}}{v_{b,0}}\frac{\partial^2 \tilde{C}_{DS}}{\partial \tilde{X}_{DS}^2}\left(\frac{1}{L_{DS,0}\tilde{L}_{DS}}\right)^2 \tag{4.9a}$$

$$\frac{\partial \tilde{C}_{DS}}{\partial \tilde{T}} + \frac{1}{\tilde{L}_{DS}}\frac{v_b}{v_{b,0}}\frac{\partial \tilde{C}_{DS}}{\partial \tilde{X}_{DS}} = \left(\frac{1}{\tilde{L}_{DS}}\right)^2 \frac{D_b}{L_{DS,0}v_{b,0}}\frac{\partial^2 \tilde{C}_{DS}}{\partial \tilde{X}_{DS}^2} \tag{4.9b}$$

$$\frac{\partial \tilde{C}_{DS}}{\partial \tilde{T}} + \frac{1}{\tilde{L}_{DS}}\frac{v_b}{v_{b,0}}\frac{\partial \tilde{C}_{DS}}{\partial \tilde{X}_{DS}} = \left(\frac{1}{\tilde{L}_{DS}}\right)^2 \frac{1}{Pe_{DS,0}}\frac{\partial^2 \tilde{C}_{DS}}{\partial \tilde{X}_{DS}^2} \tag{4.9c}$$

where $Pe_{DS,0}$ is the Peclet number at the onset of the simulation. A similar analysis is performed to obtain the dimensionless distance $\tilde{X}_{FS}$. Noting that the FS space domain is decreasing, $\tilde{X}_{FS}$ is related to L_{FS} and the normalized time varying length $\tilde{L}_{FS}$ is as follows

$$L_{FS} = L_{FS,0} - \int_0^t v_b \, dt \tag{4.10a}$$

$$= L_{FS,0} - \int_0^{\tilde{T}} v_b \frac{L_{DS,0}}{v_{b,0}} d\tilde{T} \tag{4.10b}$$

$$\tilde{L}_{FS} = \frac{L_{FS}}{L_{FS,0}} = 1 - \frac{L_{DS,0}}{L_{FS,0}}\int_0^{\tilde{T}} \frac{v_b}{v_{b,0}} d\tilde{T} \tag{4.10c}$$

$$\tilde{X}_{FS} = \frac{x_{FS}}{L_{FS}} = \frac{x_{FS}}{L_{FS,0}\left(1 - \frac{L_{DS,0}}{L_{FS,0}}\int_0^{\tilde{T}} \frac{v_b}{v_{b,0}} d\tilde{T}\right)} = \frac{x_{FS}}{L_{FS,0}\tilde{L}_{FS}} \tag{4.10d}$$

Since $\tilde{L}_{FS}$ is not a function of position x_{FS}, the derivatives of concentration *wrt* x_{FS} are

$$\frac{\partial \tilde{C}_{FS}}{\partial x_{FS}} = \frac{\partial \tilde{C}_{FS}}{\partial \tilde{X}_{FS}}\frac{\partial \tilde{X}_{FS}}{\partial x_{FS}} = \frac{\partial \tilde{C}_{FS}}{\partial \tilde{X}_{FS}}\frac{1}{L_{FS,0}\tilde{L}_{FS}} \tag{4.11a}$$

$$\frac{\partial^2 \tilde{C}_{FS}}{\partial x_{FS}{}^2} = \frac{\partial}{\partial x_{FS}}\left(\frac{\partial \tilde{C}_{FS}}{\partial \tilde{X}_{FS}}\frac{1}{L_{FS,0}\tilde{L}_{FS}}\right) = \frac{\partial^2 \tilde{C}_{FS}}{\partial \tilde{X}_{FS}^2}\left(\frac{1}{L_{FS,0}\tilde{L}_{FS}}\right)^2 \tag{4.11b}$$

52

Substituting equation 4.11a and 4.11b into equation 4.5,

$$\frac{\partial \tilde{C}_{FS}}{\partial \tilde{T}} + \frac{v_b L_{DS,0}}{v_{b,0}} \frac{\partial \tilde{C}_{FS}}{\partial \tilde{X}_{FS}} \frac{1}{L_{FS,0}\tilde{L}_{FS}} = \frac{D_b L_{DS,0}}{v_{b,0}} \frac{\partial^2 \tilde{C}_{FS}}{\partial \tilde{X}_{FS}^2} \left(\frac{1}{L_{FS,0}\tilde{L}_{FS}}\right)^2 \qquad (4.12a)$$

$$\frac{\partial \tilde{C}_{FS}}{\partial \tilde{T}} + \frac{1}{\tilde{L}_{FS}} \frac{L_{DS,0}}{L_{FS,0}} \frac{v_b}{v_{b,0}} \frac{\partial \tilde{C}_{FS}}{\partial \tilde{X}_{FS}} = \left(\frac{1}{\tilde{L}_{FS}}\right)^2 \left(\frac{L_{DS,0}}{L_{FS,0}}\right)^2 \frac{D_b}{L_{DS,0}v_{b,0}} \frac{\partial^2 \tilde{C}_{FS}}{\partial \tilde{X}_{FS}^2} \qquad (4.12b)$$

$$\frac{\partial \tilde{C}_{FS}}{\partial \tilde{T}} + \frac{1}{\tilde{L}_{FS}} \frac{L_{DS,0}}{L_{FS,0}} \frac{v_b}{v_{b,0}} \frac{\partial \tilde{C}_{FS}}{\partial \tilde{X}_{FS}} = \left(\frac{1}{\tilde{L}_{FS}}\right)^2 \left(\frac{L_{DS,0}}{L_{FS,0}}\right)^2 \frac{1}{Pe_{DS,0}} \frac{\partial^2 \tilde{C}_{FS}}{\partial \tilde{X}_{FS}^2} \qquad (4.12c)$$

Since equation 4.6 does not have a moving boundary domain, x_M can be normalized by L_M to obtain

$$\frac{\partial \tilde{C}_M}{\partial \tilde{T}} + \frac{L_{DS,0}}{L_M} \frac{v_m}{v_{b,0}} \frac{\partial \tilde{C}_M}{\partial \tilde{X}_M} = \left(\frac{L_{DS,0}}{L_M}\right)^2 \frac{D_M}{D_b} \frac{D_b}{L_{DS,0}v_{b,0}} \frac{\partial^2 \tilde{C}_M}{\partial \tilde{X}_M^2} \qquad (4.13a)$$

$$\frac{\partial \tilde{C}_M}{\partial \tilde{T}} + \frac{L_{DS,0}}{L_M} \frac{v_m}{v_{b,0}} \frac{\partial \tilde{C}_M}{\partial \tilde{X}_M} = \left(\frac{L_{DS,0}}{L_M}\right)^2 \frac{D_M}{D_b} \frac{1}{Pe_{DS,0}} \frac{\partial^2 \tilde{C}_M}{\partial \tilde{X}_M^2} \qquad (4.13b)$$

The driving force for water flux, v_b, across the FO membrane is determined by the osmotic pressure difference, $\Delta\pi$, across the membrane and foulant layer (if present), the intrinsic resistance of the membrane and the foulant layer, and any applied pressure (P_0) to augment the driving force in pressure assisted systems. Assuming a constant depth of the membrane (L_M) and foulant layer (L_F), v_b, $v_{b,0}$, and v_M can be expressed as:

$$v_b = \frac{\sigma}{\mu\left(\frac{L_M}{k_M} + \frac{L_F}{k_F}\right)} \left(\Delta\pi + P_0\right) \qquad (4.14a)$$

$$v_{b,0} = \frac{\sigma}{\mu\left(\frac{L_M}{k_M} + \frac{L_F}{k_F}\right)} \left(\Delta\pi_0 + P_0\right) \qquad (4.14b)$$

$$v_M = \frac{v_b}{\varepsilon}\left(1 - \sigma\right) \qquad (4.14c)$$

$$\frac{v_b}{v_{b,0}} = \frac{\Delta\pi + P_0}{\Delta\pi_0 + P_0} \qquad (4.14d)$$

$$\frac{v_M}{v_{b,0}} = \frac{v_b}{v_{b,0}} \frac{(1 - \sigma)}{\varepsilon} \qquad (4.14e)$$

where k_M and k_F are the membrane and foulant layer permeability, respectively, σ is the membrane reflection coefficient, μ is the water viscosity, and ε is the membrane porosity. For a completely rejecting membrane, $\sigma = 1.0$ e [114, 115]. Since the membrane is not

53

completely impermeable to salt, a reflection coefficient was incorporated into the model to account for the reduction in osmotic pressure as a result of the flux of ions across the membrane. $\Delta \pi$ is the difference between the bulk osmotic pressures of the DS(π_{DS}) and FS(π_{FS}), respectively, given by

$$\Delta \pi = \phi \left(c_{DS}(x_{DS} = 0) - c_{FS}(x_{FS} = L_{FS}) \right) RT \tag{4.15a}$$

$$\Delta \pi = \phi \left(\tilde{C}_{DS}(\tilde{X}_{DS} = 0) - \tilde{C}_{FS}(\tilde{X}_{FS} = 1) \right) c_{DS,0} RT \tag{4.15b}$$

where ϕ is the osmotic coefficient factor introduced to correct for the deviations of real solutions from ideal behavior. Subsequently, σ and ϕ were identified as the appropriate fitting parameters in the process model. The partial differential equations 4.9c, 4.12c, and 4.13b are subject to the following initial conditions

$$c_i(t = 0, x_i) = c_{i,0} \tag{4.16a}$$

$$\tilde{C}_{DS}(\tilde{T} = 0, \tilde{X}_{DS}) = 1 \tag{4.16b}$$

$$\tilde{C}_{FS}(\tilde{T} = 0, \tilde{X}_{FS}) = \frac{c_{FS,0}}{c_{DS,0}} \tag{4.16c}$$

$$\tilde{C}_{M}(\tilde{T} = 0, \tilde{X}_{M}) = \frac{c_{M,0}}{c_{DS,0}} \tag{4.16d}$$

and boundary conditions (going from FS to M then DS),

$$\left(v_b c_{FS} - D_b \frac{\partial c_{FS}}{\partial x_{FS}} \right) \Bigg|_{t, x_{FS} = 0} = 0 \tag{4.17a}$$

$$c_{FS}(t, x_{FS} = L_{FS}) = c_M(t, x_M = 0) \tag{4.17b}$$

$$\int_0^{x_{FS}} c_{FS}(t, x_{FS}) \mathrm{d}x_{FS} = \int_0^{x_{FS}} c_{FS}(t = 0, x_{FS}) \mathrm{d}x_{FS} - \int_0^t \varepsilon \left(v_M c_M - D_M \frac{\partial c_M}{\partial x_M} \right) \Bigg|_{t, x_M = 0} \mathrm{d}t$$

$$\tag{4.17c}$$

$$c_M(t, x_M = L_M) = c_{DS}(t, x_{DS} = 0) \tag{4.17d}$$

$$\int_0^{x_{FS}} c_{FS}(t, x_{FS}) \mathrm{d}x_{FS} + \int_0^{x_M} \varepsilon c_M(t, x_M) \mathrm{d}x_M + \int_0^{x_{DS}} c_{DS}(t, x_{DS}) \mathrm{d}x_{DS} = \tag{4.17e}$$

$$\int_0^{x_{FS}} c_{FS}(t = 0, x_{FS}) \mathrm{d}x_{FS} + \int_0^{x_M} \varepsilon c_M(t = 0, x_M) \mathrm{d}x_M + \int_0^{x_{DS}} c_{DS}(t = 0, x_{DS}) \mathrm{d}x_{DS}$$

$$\left(v_b c_{DS} - D_b \frac{\partial c_{DS}}{\partial x_{DS}} \right) \Bigg|_{t, x_{DS} = L_{DS}} = 0 \tag{4.17f}$$

54

The boundary conditions in dimensionless parameters are

$$\left(\frac{v_b}{v_{b,0}} \tilde{C}_{FS} - \frac{1}{\tilde{L}_{FS}} \frac{L_{DS,0}}{L_{FS,0}} \frac{1}{Pe_{DS,0}} \frac{\partial \tilde{C}_{FS}}{\partial \tilde{X}_{FS}} \right) \Bigg|_{\tilde{T}, \tilde{X}_{FS}=0} = 0 \qquad (4.18a)$$

$$\tilde{C}_{FS}(\tilde{T}, \tilde{X}_{FS} = 1) = \tilde{C}_M(\tilde{T}, \tilde{X}_M = 0) \qquad (4.18b)$$

$$\int_0^{\tilde{X}_{FS}} \tilde{C}_{FS}(\tilde{T}, \tilde{X}_{FS}) \mathrm{d}\tilde{X}_{FS} = \int_0^{\tilde{X}_{FS}} \tilde{C}_{FS}(\tilde{T}_0, \tilde{X}_{FS}) \mathrm{d}\tilde{X}_{FS} - \qquad (4.18c)$$

$$\int_0^{\tilde{T}} \varepsilon \left(\frac{v_M}{v_{b,0}} \tilde{C}_M - \frac{L_{DS,0}}{L_M} \frac{D_M}{D_b} \frac{1}{Pe_{DS,0}} \frac{\partial \tilde{C}_M}{\partial \tilde{X}_M} \right) \Bigg|_{\tilde{T}, \tilde{X}_M=0}$$

$$\tilde{C}_M(\tilde{T}, \tilde{X}_M = 1) = \tilde{C}_{DS}(\tilde{T}, \tilde{X}_{DS} = 0) \qquad (4.18d)$$

$$\int_0^{\tilde{X}_{FS}} \tilde{C}_{FS}(\tilde{T}, \tilde{X}_{FS}) \tilde{L}_{FS} \frac{L_{DS,0}}{L_{FS,0}} \mathrm{d}\tilde{X}_{FS} + \int_0^{\tilde{X}_M} \varepsilon \tilde{C}_M(\tilde{T}, \tilde{X}_M) \frac{L_{DS,0}}{L_M} \mathrm{d}\tilde{X}_M + \qquad (4.18e)$$

$$\int_0^{\tilde{X}_{DS}} \tilde{C}_{DS}(\tilde{T}, \tilde{X}_{DS}) \tilde{L}_{DS} \mathrm{d}\tilde{X}_{DS} = \int_0^{\tilde{X}_{FS}} \tilde{C}_{FS}(\tilde{T} = 0, \tilde{X}_{FS}) \tilde{L}_{FS} \frac{L_{DS,0}}{L_{FS,0}} \mathrm{d}\tilde{X}_{FS} +$$

$$\int_0^{\tilde{X}_M} \varepsilon \tilde{C}_M(\tilde{T} = 0, \tilde{X}_M) \frac{L_{DS,0}}{L_M} \mathrm{d}\tilde{X}_M + \int_0^{\tilde{X}_{DS}} \tilde{C}_{DS}(\tilde{T} = 0, \tilde{X}_{DS}) \tilde{L}_{DS} \mathrm{d}\tilde{X}_{DS}$$

$$\left(\frac{v_b}{v_{b,0}} \tilde{C}_{DS} - \frac{1}{\tilde{L}_{DS}} \frac{1}{Pe_{DS,0}} \frac{\partial \tilde{C}_{DS}}{\partial \tilde{X}_{DS}} \right) \Bigg|_{\tilde{T}, \tilde{X}_{DS}=1} = 0 \qquad (4.18f)$$

In developing the model system, equal flux boundary conditions at the membrane-DS and membrane-FS interfaces were not used because combinations thereof resulted in either unrealistic concentration profiles or unacceptable errors in overall salt material balance. The combination of the above boundary conditions ensured both a realistic concentration profile and mass conservation.

4.2.5 Process Model Solution

When the spatial domains (i.e., L_{DS}, L_{FS} and L_M) are divided into $N_{DS} - 1$, $N_{FS} - 1$ and $N_M - 1$ sections, the concentration along N nodes are unknown and must be solved. The concentration derivatives with respect to space were discretized using finite differences, resulting in $N_{DS} + N_{FS} + N_M - 6$ ordinary differential equations in time and six algebraic equations corresponding to the boundary conditions. The model constitute a system of differential-algebraic equations that were solved using DASSL as implemented in Scilab [116].

55

4.2.6 Extrapolation to full-scale

At the process level, water flux is predicted based on full-scale membrane dimensions using membrane parameters obtained from the results of MD simulations and least-square parameter estimation. The model was reformulated to reflect a fixed FS and DS dimensions (i.e., no moving boundary) with constant salt concentrations at the bulk boundaries between the DS and FS. This was achieved by defining a mass transfer boundary layer thickness at the membrane-DS and membrane-FS interfaces such that salt concentration beyond that thickness remained fixed and equivalent to the bulk concentration. The schematic of the scaled up FO system is shown in Fig. 4.2. In addition, the boundary conditions were revised to account for the flux of salts into the respective domains. Although this does not completely represent the experimental conditions, the results are expected to give a first approximation to the full-scale behavior of the FO system.

The experimental bench-scale FO setup consisted of a double channel with dimensions of 76 mm length, 27 mm width, and 2 mm height, providing an effective area of $41.02\,\text{cm}^2$. The flow rate and cross flow velocity were $0.19\,\text{L/min}$ and $10\,\text{cm}^2/\text{s}$, respectively. Based on the available experimental data, the calculated Reynolds number, *Re* indicated a laminar flow regime, hence the Sherwood number, *Sh* was calculated using the laminar correlation for a rectangular channel [117, 114]:
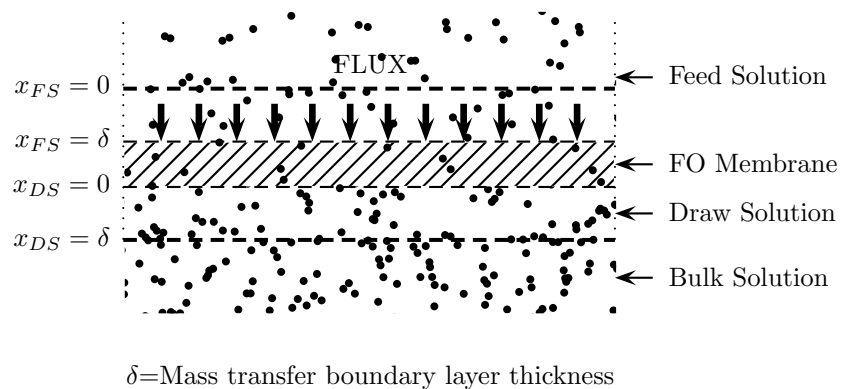

δ=Mass transfer boundary layer thickness

Fig. 4.2   Schematic of scaled up FO system.

$$Sh = 1.85 \left(ReSc \frac{d_h}{L} \right)^{0.33} \tag{4.19}$$

where Sc is Schmidt number, d_h is the hydraulic diameter, and L is the length of the channel. The mass transfer coefficient, k, and the theoretical mass transfer boundary layer thickness, δ were calculated based on the Sherwood number and the diffusion coefficients, D for the salts using:

$$Sh = \frac{kd_h}{D} \tag{4.20a}$$

$$\delta = \frac{D}{k} \tag{4.20b}$$

4.3   Results and discussion

4.3.1   Osmotic water flux

Initial osmotic pressure gradients of 8.75, 9.0 and 12.85 MPa are created across the membrane for the KCl, NaCl and CaCl$_2$ FO systems, respectively. In the case of the divalent DS solute, there is an increased ionic species in solution, hence the higher osmotic pressure gradient. The driving force resulting from the osmotic pressure gradient across the membrane induces a net osmotic water transport along the $+z$-direction from the FS to the DS. The water flux is quantified by the movement of the graphene sheet initially located above the FS domain. Snapshots of the simulated FO system are presented in Fig. 4.3, where a lower graphene position is observed at the end of the 100 ns simulation. The change in the graphene position with time for replicate simulations conducted with different membrane configurations is presented in Fig. 4.4. At the initial stage of the simulations, water flows across the membrane at a relatively constant rate, hence the observed linear regime in the graphene displacements. However, beyond 20 ns the variations in the graphene displacements become pronounced due to the increased effect of the membrane pore connectivity on water transport. Furthermore, a gradual decreasing trend is observed in the graphene
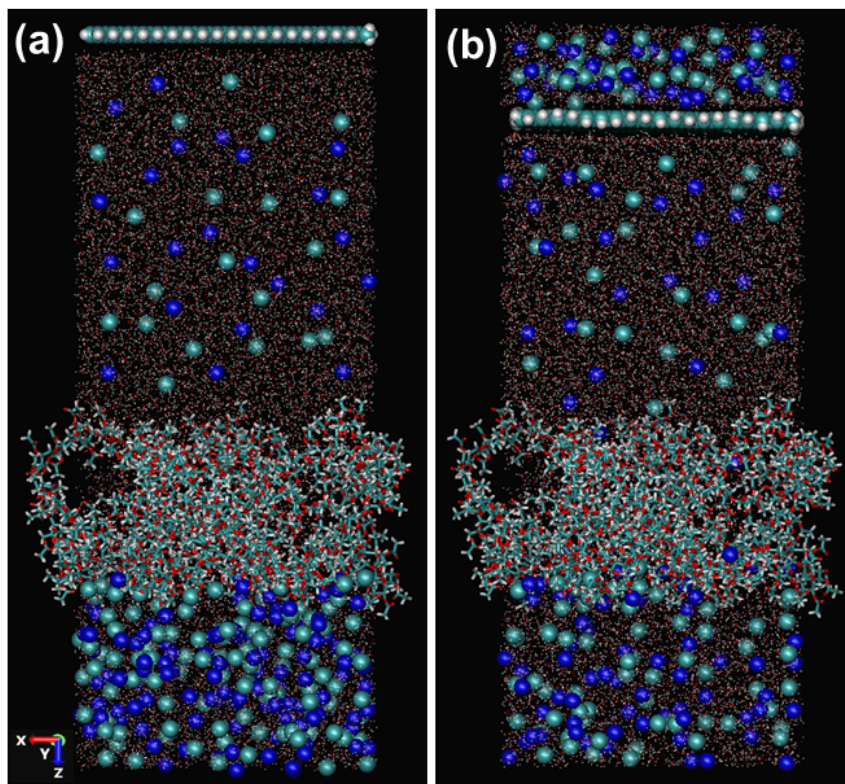
Fig. 4.3 Snapshots of (a) Osmotic water transport simulation initial setup (b) Osmotic water transport simulation after 100 ns. Membrane is shown in licorice model, graphene is shown in VDW model, Na$^+$ and Cl$^-$ ions are shown as blue and green spheres, respectively and TIP3P water molecules shown as points.

displacements because of the reduction in osmotic driving force as a result of the dilution of the DS concentration and back diffusion of salt.

Due to the dependence of the osmotic driving force on concentration gradient, slight changes in concentration resulting from dilution, reverse salt flux (RSF) and ICP can significantly impact the driving force for water transport. ICP results from the buildup of solutes at the membrane surface which reduces permeate flux because of the increased osmotic pressure that must be overcome to facilitate water transport. Depending on the severity of ICP and the rate of RSF, the osmotic driving force can vary significantly as depicted by the "noisy" nature of the graphene displacements.

The average salt concentration profiles over the initial and final 5 ns for the base production simulation are shown in Fig. 4.5. The membrane is located in the region $-7.5\,\text{Å} <$
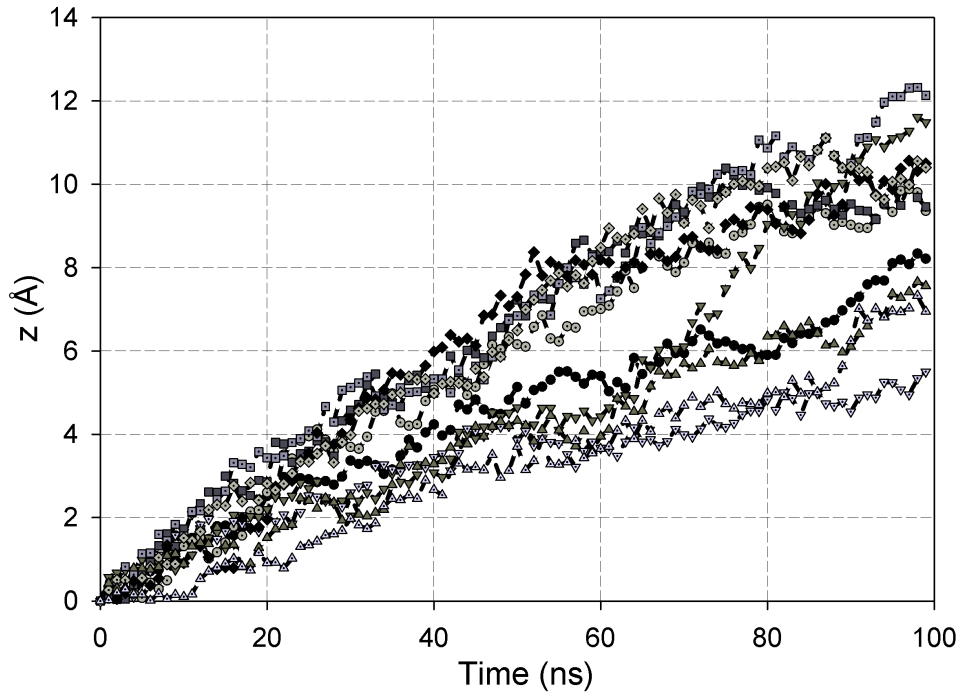
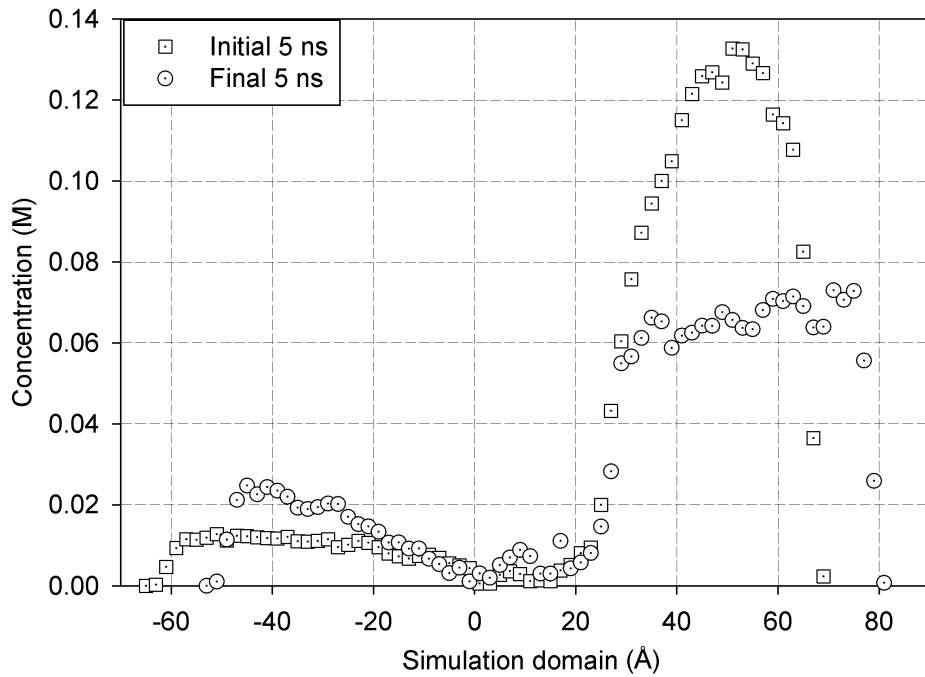Fig. 4.4   Graphene displacements for replicate simulations.

Fig. 4.5   Average salt concentration profiles over simulation domain.

59

z > +28.5 Å and its position remained relatively fixed over the course of the simulation. The flow of water across the membrane results in the movement of the graphene sheet from its initial position of −63.5 Å to −51.4 Å, traveling a total distance of 12.1 Å within 100 ns. Noting that the volume of the simulation box remains constant and that periodic boundary conditions are implemented, an increase in the salt concentration is observed in the FS domain (initially at −63.5 Å < z > −7.5 Å) between the graphene and the membrane. The increase in the FS concentration is due to the influx of water into the DS domain (initially at +28.5 Å < z > −68.5 Å), thus reducing the volume of water in the FS domain and diluting the DS concentration over time. The dilution of the DS, coupled with the back diffusion of salt across the membrane subsequently results in a decrease in the DS salt concentration.

The decrease in the DS salt concentration with time results in an overall reduction in the driving force for water transport. This leads to a reduction in the net water flux and a corresponding decrease in the graphene velocity as depicted in the trends observed in Fig. 4.4. Although the graphene displacements indicate no distinct decreasing trend within the 100 ns, the water flux is expected to decrease over the course of a longer simulation. At equilibrium, the graphene sheet is expected to be stationary due to zero net flux of water across the membrane. A flat concentration region that corresponds to the bulk DS and a decline in the salt concentration as it approaches the membrane is expected. This will however require a considerable longer time to simulate. The variations in the average ion concentration in the FS, DS and membrane domains over the course of the simulation are shown in Fig. 4.6. The average concentration of ions in the membrane increases within the first 5 ns and remains relatively constant within the time frame of the simulation. Although the increase in salt concentration results from the occurrence of RSF and the influx of salt from the FS domain, the overall salt flux across the membrane is dictated by the RSF effect. Moreover, the trend of the membrane concentration profile suggests that RSF effects may be dominant at the initial stage of the simulations. RSF as a function of water chemistry can significantly vary depending on the type of DS solute (will be discussed in later section).
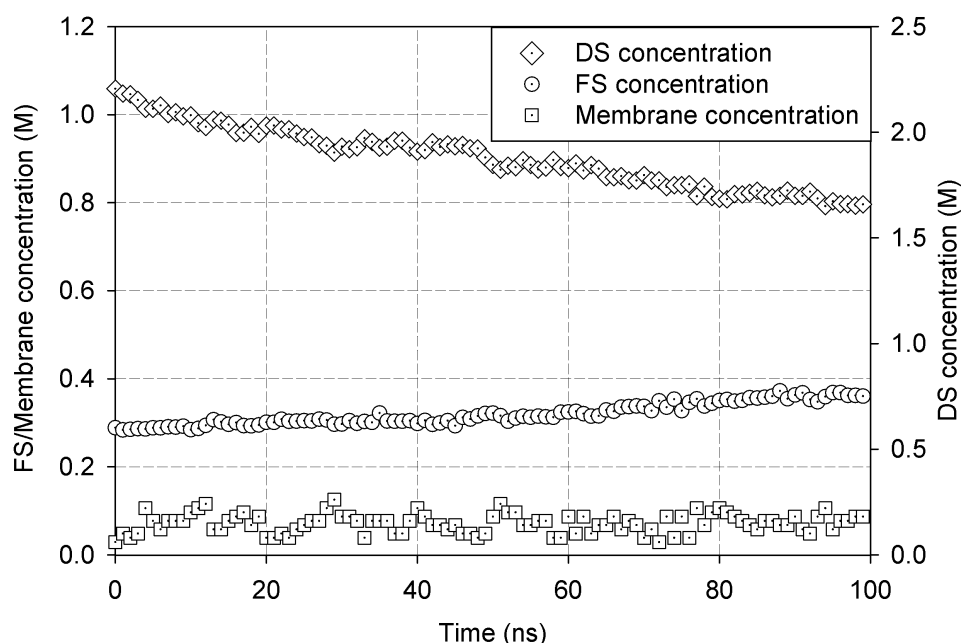
Fig. 4.6   DS, FS, and membrane salt concentration profiles over 100 ns.

4.3.2   Estimation of water permeability and salt diffusivity

The flux of water and salt across membranes can be quantified based on membrane parameters such as permeability and diffusion coefficients. In the present study, data obtained from NEMD and equilibrium MD simulations are used to estimate CTA membrane permeability and diffusion coefficients of NaCl, KCl and $CaCl_2$. The detailed discussion on estimating pure water permeability has been presented in Chapter 3. Briefly, pure water permeability is quantified based on the slope of the graphene displacements from the pressure-induced simulations. A relatively constant water flux is observed in the pressure-induced simulations because of the constant external forces on the graphene piston, which maintains a driving force for continuous water transport. The experimental protocol for estimating pure water permeability involves measuring the change in the weight of the permeate over a given time [56]. In accordance with experimental procedures, water flux in the CTA membrane is quantified based on the velocity of the graphene. In estimating the pure water permeability, simulations were performed using unique membrane configurations to

61

capture the uncertainty associated with the membrane and to obtain realistic permeability estimates.

The flux of salt across the solvated membrane system is quantitatively described by salt diffusivity and membrane rejection coefficient. The diffusion of salt in the membrane can be influenced by intrinsic membrane properties such as porosity and density. Fig. 4.7 shows the density profiles for the solvated membrane system. Although the membrane position ranges from -7.5 to $+28.5$ Å, a reasonable estimate of the membrane thickness is defined over the highest density region, -4.5 Å $< z > +25.5$ Å resulting in a membrane thickness of 30 Å. Therefore, to obtain realistic estimates of the diffusion coefficients in the
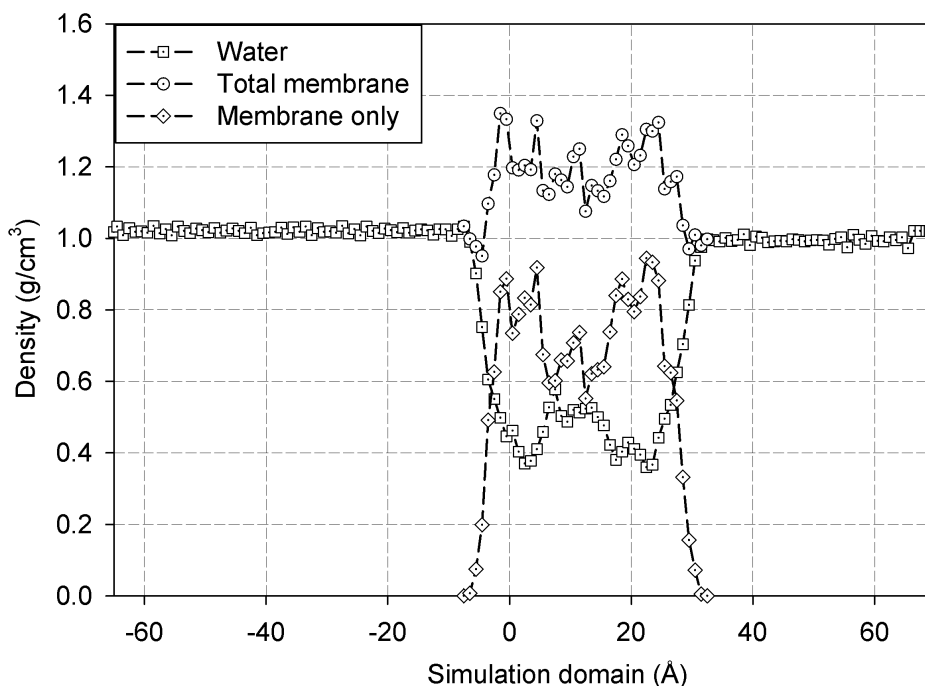
Fig. 4.7   Density profiles for solvated membrane system over simulation domain.

membrane, the diffusion of the ions were confined within the highest density region during the simulations. The trajectories of five salt ion pairs are used to calculate the diffusion coefficients based on the mean-squared displacement of the ions along the z-axis. The diffusion coefficients of salts in the membrane and in the bulk are calculated based on the

62

results of a 10 ns equilibrium MD simulations. The combined bulk diffusion coefficients for the different DS salts are fairly consistent with experimental results. The estimated membrane parameters are subsequently used to predict the behavior of the FO system at the full-scale.

4.3.3 Process modeling of FO system

The process model predictions of the FO system behavior are compared to the results of the MD simulations to evaluate the accuracy of the model representation of the molecular domain. A comparison of the predictions with the simulation data indicates consistency in the trends of the graphene displacement and salt concentration profiles. The predicted velocity profile for the graphene over the course of the simulation is presented in Fig. 4.8. Due to the dependence of the driving force on the osmotic pressure gradient, a decrease in the osmotic pressure results in a gradual reduction in the graphene velocity which is in good accord with observations at the molecular level. Parameter estimation based on least-
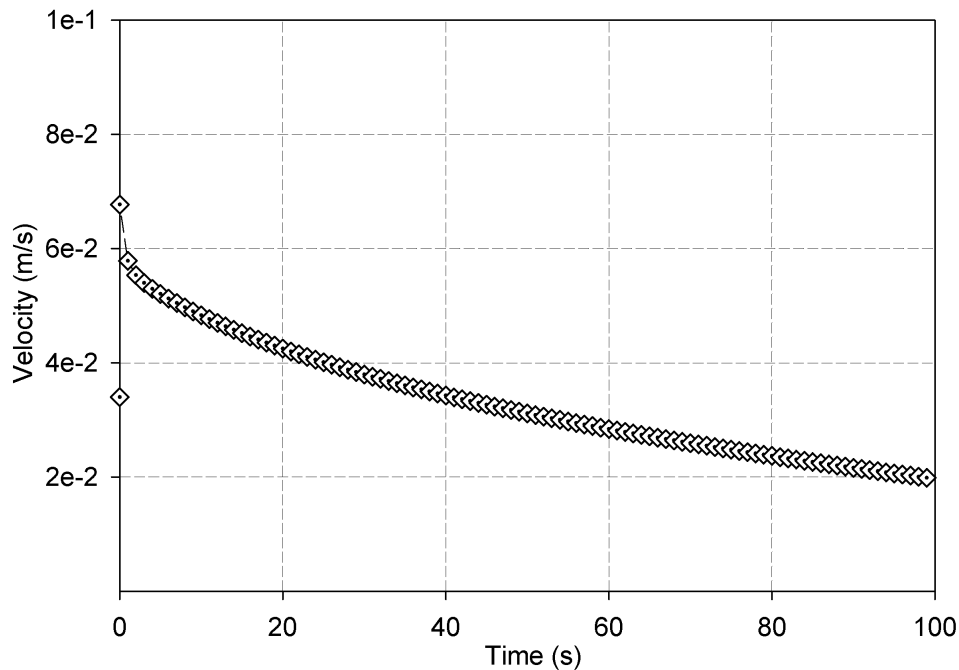

Fig. 4.8   Predicted graphene velocity profile.

square fitting of the process model is performed to adjust model parameters to accurately capture the observations at the molecular scale. Fig. 4.9 shows a fit of the process model to the graphene displacement data for the base simulation. Based on the fitted parameters, the model indicates sensitivity to the osmotic and reflection coefficients and gives reasonable estimates of the parameters. The osmotic coefficient is a property of the salt which corrects for non-ideal behavior while the refection coefficient accounts for the reduction in osmotic pressure as a result of ion permeation into the membrane.
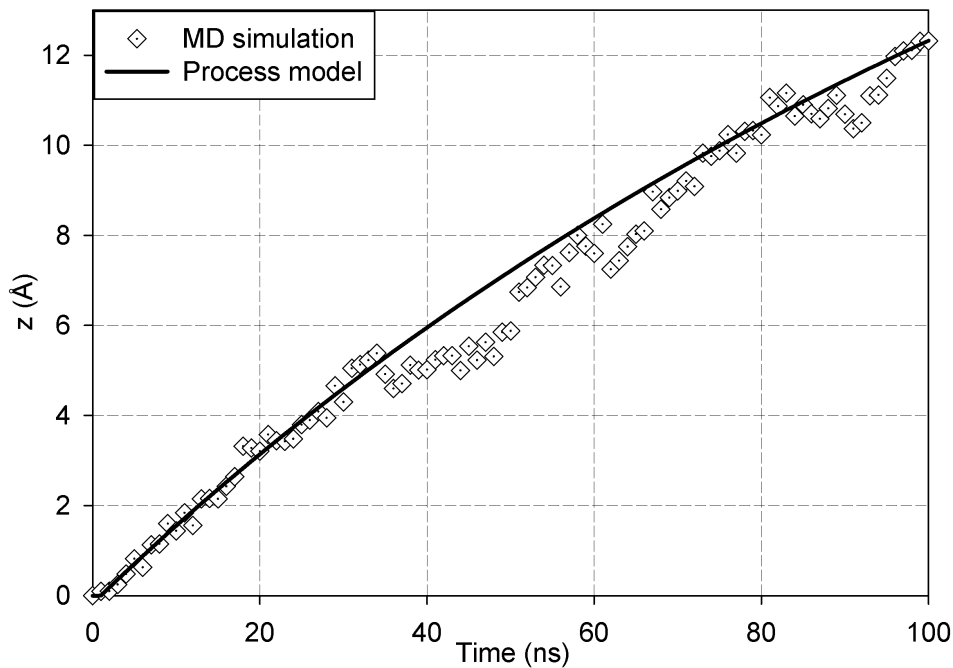
Fig. 4.9   Least-square fit of graphene displacement.

Fig. 4.10 shows a fit of the process model to the NaCl concentration in the FS, membrane and DS, expressed as total ion count in each domain over the course of the simulation. Despite the significant changes in the FS and DS salt concentration observed in Fig. 4.6, the total ion count in these regions indicates less variation with time. These observations suggest that changes in FS and DS salt concentration are dominated by dilution effects rather than RSF. Indeed, only three DS ions completely crossed the membrane to the FS domain while two FS ions permeated the membrane in the reverse direction over the time frame of

64
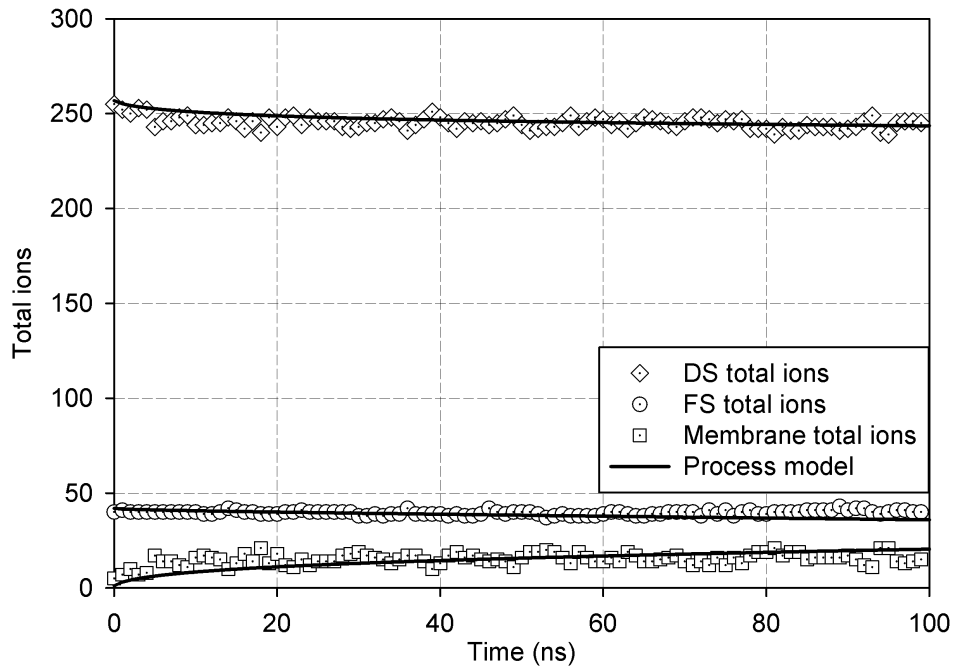
Fig. 4.10   Least-square fit of DS, FS, and membrane total ions.

the simulations. The relatively constant ions concentration in the FS and DS domains also gives an indication of a high salt rejection by the membrane. Therefore a fit of the process model to the salt concentration is expected to give a realistic estimate of the refection coefficient of the membrane. Since the reflection coefficient defines the percentage of salt reflected away from the surface of the membrane, the estimated value is expected to give an indication of the membrane's selectivity to salt. In general, the reflection coefficient can be related to solute permeability to estimate the observed rejection coefficients in membrane processes.

Table 4.1 summarizes the parameters for the CTA membrane. As observed, the diffusion and reflection coefficients indicate some dependence on the membrane permeability. Overall, high permeability membranes indicate lower values of the reflection coefficients and higher salt diffusivity. This is attributed to the effect of pore connectivity on solute transport within the membranes. For the $CaCl_2$ and KCl systems, similar procedures were followed to estimate the membrane parameters using data from a single base simulation.

65

Table 4.1   Estimated membrane parameters.

CTA	$k_m(10^{-21}m^2)$	$D_m(10^{-11}m^2/s)$	ϕ	σ
1	5.66	9.26	0.87	0.964
2	7.21	7.49	0.89	0.982
3	7.61	8.82	0.88	0.967
4	4.37	7.06	0.89	0.975
5	10.30	9.92	0.87	0.962
6	11.60	13.67	0.86	0.942
7	6.78	12.79	0.91	0.982
8	6.12	6.84	0.90	0.969
9	4.70	9.92	0.89	0.988
10	4.12	7.28	0.90	0.987
Average	6.83 ±2.48	9.31 ±2.37	0.87 ±0.01	0.973 ±0.011

4.3.3.1   Full-scale water flux prediction

The estimated parameters are intrinsic membrane properties and can therefore be directly used for full-scale predictions. However, the membrane thickness is considered an uncertain parameter and its defined based on the manufacturer's specified range of 5-15 μm. Fig. 4.11 shows the predicted full-scale water flux based on a 10 μm membrane thickness and 100 μm mass transfer boundary layer thickness. Predictions indicate an immediate drop in the water flux from 6.0×10^{-6}m/s to 3.6×10^{-6}m/s because of the rapid rearrangement of the solute ions in the DS and FS mass transfer boundary layers. The water flux approaches steady within a few seconds and remains constant afterwards because of the fixed bulk salt concentration. In contrast, the bench-scale experiments were conducted in a continuous mode which ensured a gradual decrease in the water flux. In order to predict similar trends, the process model would have to be revised to reflect the appropriate mode of operation of the experiments. It is notable however that the flux predictions are within the same order of magnitude of experiments despite the uncertainty in the membrane parameters and the different mode of operation of the scaled up FO system. To further improve full-scale predictions, proper characterization of the membrane thickness is required which is beyond the scope of this study.
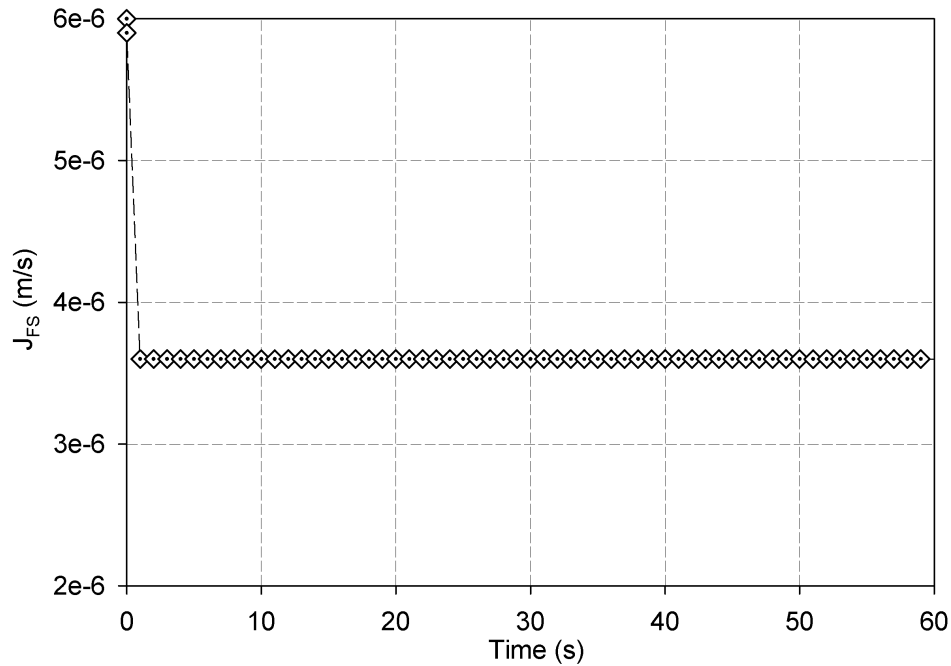
Fig. 4.11   Predicted full-scale water flux as a function of time.

The influence of mass transfer boundary layer and membrane thickness on the full-scale water flux are evaluated by conducting sensitivity tests on the parameters. The results of the sensitivity tests are shown in Fig. 4.12. As expected, the flux scales inversely with membrane thickness because of the greater resistance to flow at increased thickness. Similarly, flux decreases with an increase in mass transfer boundary layer thickness as a result of the longer distance required for back diffusion of salt. Based on these sensitivity tests, a critical point of the mass transfer boundary layer falls within 1-10 μm. The performance of an assisted FO system is assessed by applying hydraulic pressures on the FS domain from 0 to 100 MPa. The effect of the applied pressure on the water flux is shown in Fig. 4.13. The application of 1 MPa of applied pressure increases the water flux from 3.6×10^{-6}m/s to 4.1×10^{-6}m/s, indicating that the performance of FO membrane processes can be enhanced by augmenting the system with pressure to provide additional driving force for water transport. However at an applied pressure beyond 100 MPa, the effect of the mass transfer boundary layer diminishes and the system essentially becomes pressure dominated.

67
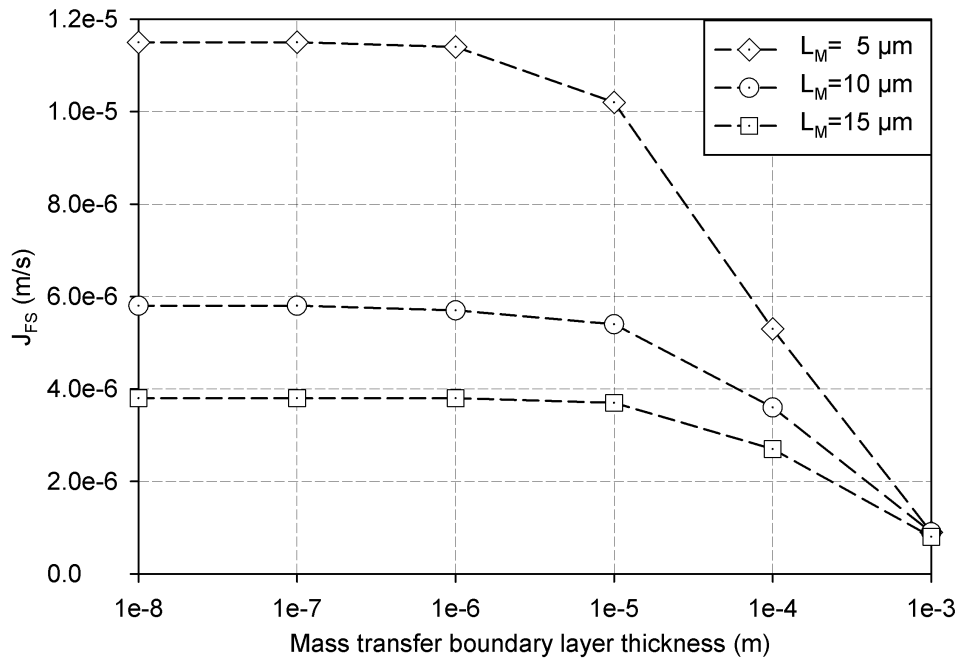
Fig. 4.12   Full-scale water flux as a function of mass transfer boundary layer and membrane thickness.

4.3.4   Influence of water quality conditions on FO processes

The assessment of the impact of different water chemistry conditions on FO processes is essential in identifying optimum treatment conditions. The influence of NOM fouling on pure water flux is shown in Fig. 4.14. A decline in water flux is observed because of the increased resistance to flow resulting from the presence of the NOM foulant layer. As expected, a thicker foulant layer produces a corresponding higher decline in water flux which suggests that the continuous buildup of NOM on membrane surfaces could lead to a significant flux decline over the course of the filtration process. The effect of different DS concentration on water flux is also investigated as shown in Fig. 4.15. Flux increases with an increase in DS concentration because of the greater concentration gradient which increases the system osmotic pressure gradient thus providing a greater driving force for water transport. Overall, the full-scale water flux is sensitive to the DS concentration range of 1-5 M. The properties of inorganic DS solutes can significantly influence water and salt
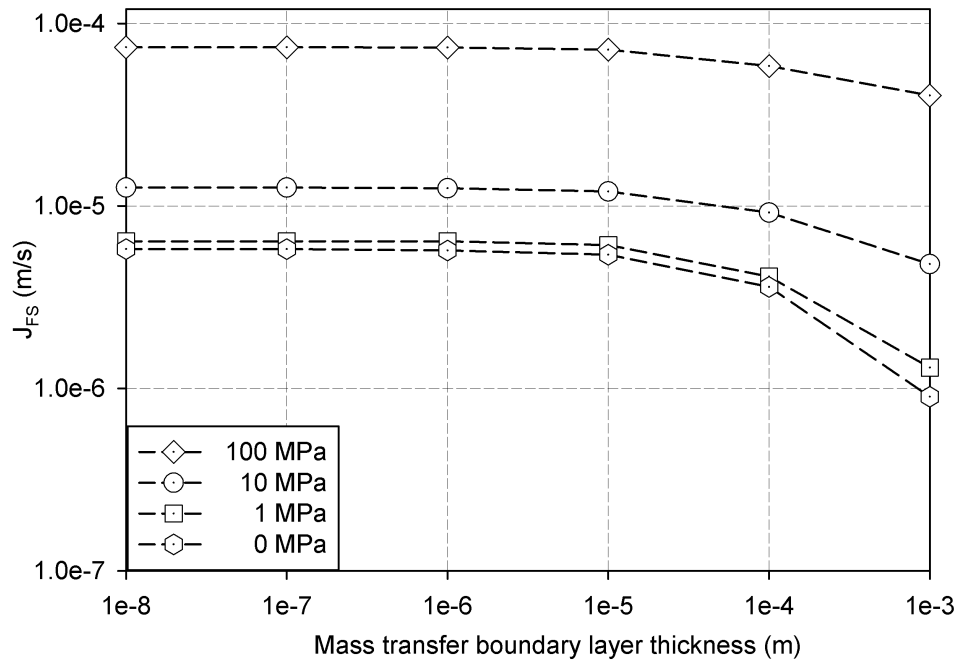
Fig. 4.13   Full-scale water flux as a function of mass transfer boundary layer and applied pressure.

transport across FO membranes. The performance of two monovalent and one divalent DS solutes are investigated to assess their separation properties in FO systems. Based on the results, the membrane exhibits greater selectivity to divalent ions because the larger hydration radii of the ions results in a lower salt permeability across the membrane. As shown in Fig. 4.16, $CaCl_2$ provides a greater driving force for water transport due to its higher osmotic pressure. Moreover, the lower permeability of $CaCl_2$ results in a reduced RSF effect which further enhances the osmotic driving force to facilitate water transport. Among the monovalent ions, Na^+ provides a slightly higher driving force for water transport since K^+ ions are less hydrated resulting in a greater K^+ ions permeability and possibly higher RSF. Thus the type of DS solutes has significant implications on the performance of osmotically driven FO processes. These observations are consistent with recent bench-scale experimental studies where the RSF was also found to be dependent on temperature [112] which emphasizes the need to optimize operating conditions to maximize process performance.

69
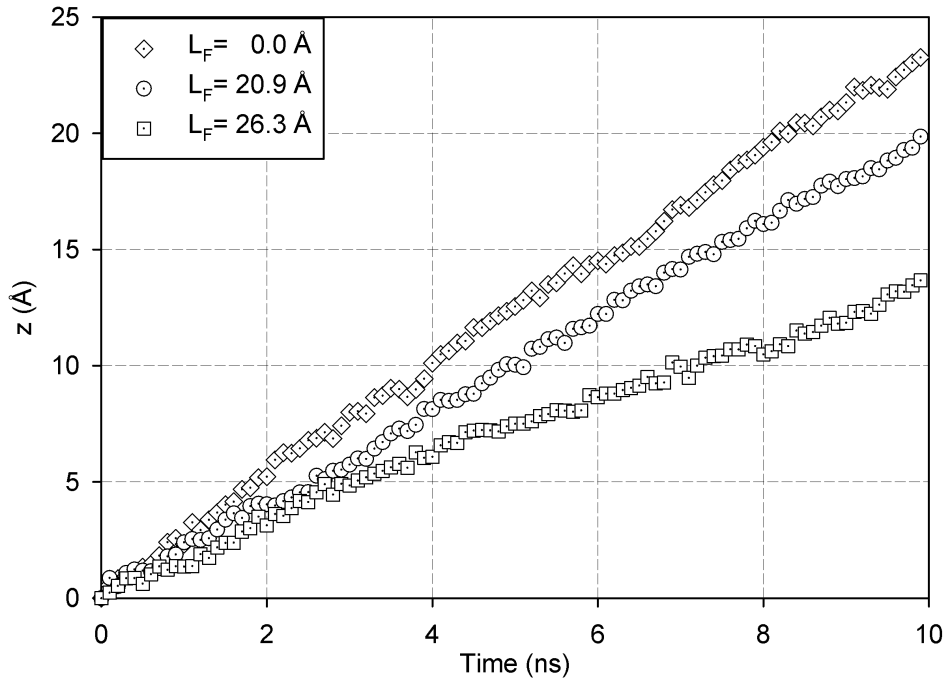
Fig. 4.14   Influence of NOM foulant on water flux.
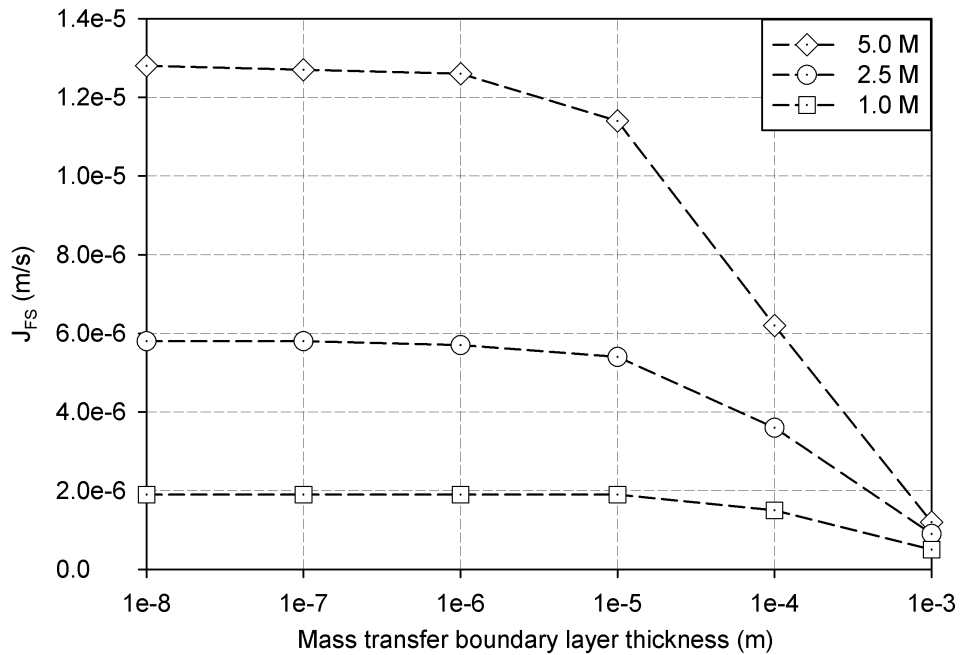
Fig. 4.15   Full-scale water flux as a function of mass transfer boundary layer and DS concentration.
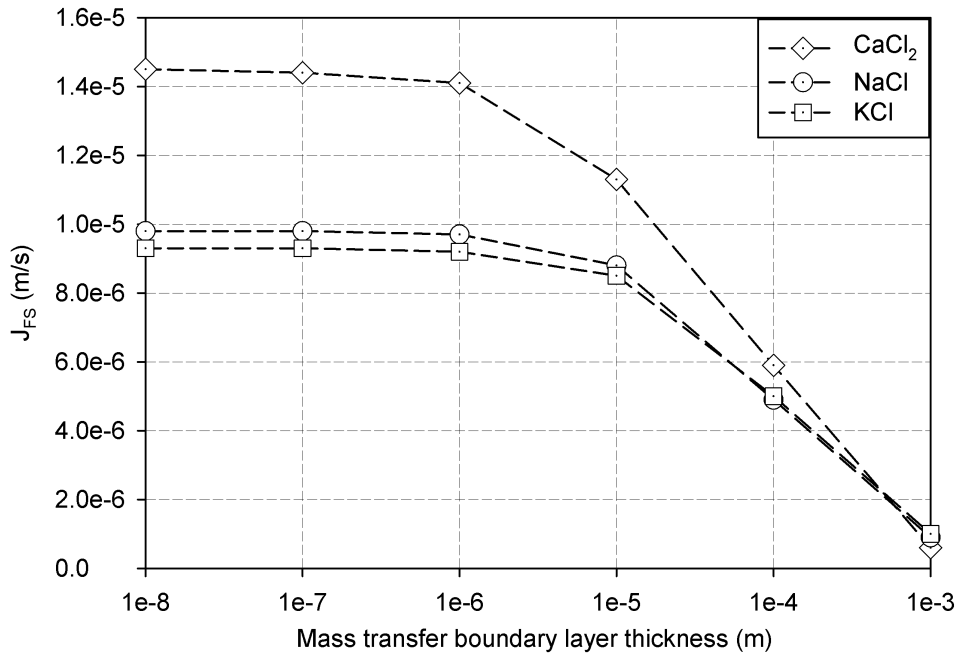
Fig. 4.16   Full-scale water flux as a function of mass transfer boundary layer and DS solutes.

4.4   Conclusions

A multiscale framework for modeling osmotic water transport and salt rejection in FO membrane systems has been presented. The framework incorporates MD simulations data into a process model to make full-scale predictions. Membrane permeability and salt diffusion coefficients were obtained from MD simulations performed using different membrane configurations. The estimated membrane parameters were used to predict full-scale water flux based on a specified full-scale membrane thickness. The results indicated that the driving force for water transport is influenced by dilution of the DS and the back diffusion of salt across the membrane. At the process level, water flux decreases with an increase in mass transfer boundary layer thickness because of the longer distance required for back diffusion of salt across the membrane. The critical point of the mass transfer boundary layer for the simulated FO system was found to be within 1-10 μm based on a membrane thickness range of 5-15 μm.

71

Furthermore, DS concentration and the type of DS solutes indicated significant effect on the osmotic driving force, in accordance with experiments. Divalent ions provide greater driving force for water transport due to higher osmotic pressure and lower RSF effects compared to monovalent ions. The presence of NOM foulant layer resulted in a decline in water flux suggesting that NOM fouling can significantly impact FO performance.

Overall, the predicted full-scale water flux was consistent with experiments suggesting that MD simulations can potentially be scaled up to capture process level observations. The presented framework can be useful for studying water and salt transport mechanisms at the molecular and process levels to gain insight into FO desalination processes.

Acknowledgments

Nomenclature

DS Draw solution

FS Feed solution

M Membrane

C_{DS0} Initial DS salt concentration (M)

C_{FS0} Initial FS salt concentration (M)

C_M Membrane salt concentration (M)

C_{DS} DS salt concentration (M)

C_{FS} FS salt concentration(M)

L_{DS0} Initial length of DS domain (m)

L_{FS0} Initial length of FS domain (m)

L_{DS} Length of DS domain (m)

L_{FS} Length of FS domain (m)

x_{DS} DS spatial domain (m)

x_{FS} FS spatial domain (m)

x_M Membrane spatial domain (m)

$\tilde{C}_{DS}$ Dimensionless DS salt concentration

$\tilde{C}_{FS}$ Dimensionless FS salt concentration

$\tilde{L}_{DS}$ Dimensionless length of DS domain

$\tilde{L}_{FS}$ Dimensionless length of FS domain

t Time (s)

$\tilde{T}$ Dimensionless time

$\tilde{x}_{DS}$ Dimensionless DS spatial domain

$\tilde{x}_{FS}$ Dimensionless FS spatial

$\tilde{x}_M$ Dimensionless membrane spatial domain

73

Nomenclature

$v_{b,0}$ Initial water velocity (m/s)

v_b Bulk velocity (m/s)

v_M Water velocity in membrane (m/s)

L_M Length of membrane (m)

L_F Length of foulant layer (m)

k_M Membrane permeability (m^2)

k_F Foulant layer permeability (m^2)

P_0 Applied pressure (MPa)

$\Delta\pi$ Osmotic pressure difference (MPa)

σ Reflection coefficient

ϕ Osmotic coefficient

ε Membrane porosity

μ Water viscosity (Pa-s)

J_{FS} Full-scale water flux (m/s)

CHAPTER 5

INFLUENCE OF FUNCTIONALIZATION ON THE DESALINATION PERFORMANCE OF NANOPOROUS GRAPHENE[1]

Abstract

Water permeability and salt rejection in nanoporous graphene (NPG) membranes are investigated using molecular dynamics simulations. The fouling propensity of the NPG membranes is also evaluated by simulating NOM interactions with the membranes via umbrella sampling. Results of the simulations established that water permeability across the NPG membranes follows the order: NPG-OH > NPG-H > NPG-COO⁻. Moreover, a higher salt rejection is observed in the COO⁻ functionalized membrane as a result of the electrostatic interactions between ions and the negatively charged membrane. The results further indicate that functionalization of NPG pores can enhance water flux and salt rejection and improve the antifouling ability of the membranes. Surface functionalization affects the orientation of water molecules approaching the pores and dictates the strength of membrane-foulants interactions. NPG-COO⁻ functionalized membrane exhibits improved antifouling performance due to less favorable membrane-foulant interactions. However, adsorption of NOM onto the NPG membranes is energetically favored and results in a water flux decline. This work highlights the implications of surface functionalization on the desalination performance of NPG membranes.

Keywords: NPG membrane; surface functionalization; molecular dynamics; permeability; salt rejection; fouling.

---

[1]Boateng, L.K., J.R.V. Flora, Y. Yoon. Influence of Functionalization on the Desalination Performance of Nanoporous Graphene. To be submitted to *Journal of Membrane Science.*

5.1 Introduction

Reports of impending water scarcity have necessitated the need to adopt desalination technologies to produce potable water from seawater and brackish water. A significant percentage of the world's future water demand is expected to be sourced from reverse osmosis (RO) seawater desalination plants. RO desalination installations have significantly increased in recent years and are currently the world-wide leading desalination technology for producing freshwater from seawater [3]. Conventional RO membranes typically compose of polyamide and cellulose acetate selective layer with a micro-porous support layer for mechanical stability. Although RO membranes are considered less energy intensive compared to other thermal distillation-based desalination technologies, full-scale implementation of RO installations can be energy and capital intensive. Next-generation membranes must overcome high energy requirements and demonstrate high water recovery and fouling resistance.

The advancement in the nanotechnology field have led to the discovery of various carbonaceous nanomaterials (CNMs) with unique physical and chemical properties. Recent simulation studies have shown that carbon nanotubes (CNTs) can provide a high flow rate of water when used as channels for water transport due to "hyperlubricity" effect [12]. Nanoporous graphene (NPG) have exhibited great desalination potential providing water flux several orders of magnitude higher than conventional RO membranes [13]. The ultrathin nature of NPG, coupled with other unique structural properties makes them sustainable and cost-effective desalination membranes. Since water flux scales inversely with membrane thickness, it is expected that NPG membranes will demonstrate high water flux with relatively lower energy demands.

Water transport and salt rejection in NPG membranes can be facilitated by creating nanopores of optimum pore sizes capable of enhancing water transport and hindering salt passage. The fabrication of nanopores in graphene has been extensively investigated using different techniques. Controlled exposure of electron beam onto graphene sheets in a trans-

76

mission electron microscope [118], helium ion beam drilling [119] and diblock copolymer templating [120] have successfully been used in generating pores on graphene sheets.

Despite the high water recovery rates observed in NPG membranes; strong hydrophobic interactions between NPG membranes and NOM can result in excessive fouling and significantly reduce membrane permeability. CNMs have exhibited high adsorptive capacity for organic compounds under both fresh and saline water conditions [55]. The underlying adsorption mechanism of organic compounds onto CNMs have been attributed to hydrophobic interactions and $\pi-\pi$ electron coupling between the adsorbent and adsorbate molecules [14]. In general, the adsorptive capacity of CNMs depends greatly on the surface functional groups and the type of adsorbate. Therefore the surface chemistry of NPG membrane pores can influence membrane-foulant interactions and the overall fouling propensity of NPG desalination membranes. The goal of this study is to simulate water and salt transport in NPG membranes and investigate the influence of NOM fouling on water flux as well as the impact of surface functionalization on NPG membrane desalination performance.

5.2 Computational methods

5.2.1 NPG system setup and simulations

A $36\,\text{Å} \times 36\,\text{Å}$ unit cell of graphene sheet was generated using the nanotube builder package in Visual Molecular Dynamics (VMD) [91] by following procedures outlined in a previous study [55]. The nanopores were created by removing the appropriate number of carbon atoms from the center of the unit cells to create NPG with different pore diameters. A pore size of $5.5\,\text{Å}$ has been reported to be sufficient to achieve water transport while restraining ions passage across NPG [13]. The OH and COO^- functionalized membranes were created by attaching six OH and COO^- functional groups, respectively to a $11.8\,\text{Å}$ diameter pore membrane. The attachment of the different functional groups resulted in a $11.2\,\text{Å}$ and $9.6\,\text{Å}$ pore diameters for the OH and COO^- functionalized membranes, respectively. The differ-

77

ence in pore diameters was due to steric constraints which restricts the functional groups to point to the center of the pore thereby reducing the effective pore size. The diameter of each NPG pore was measured as the distance between the ends of two opposite functional groups. Fig. 5.1 shows the snapshots of the NPG membranes used in the simulations.
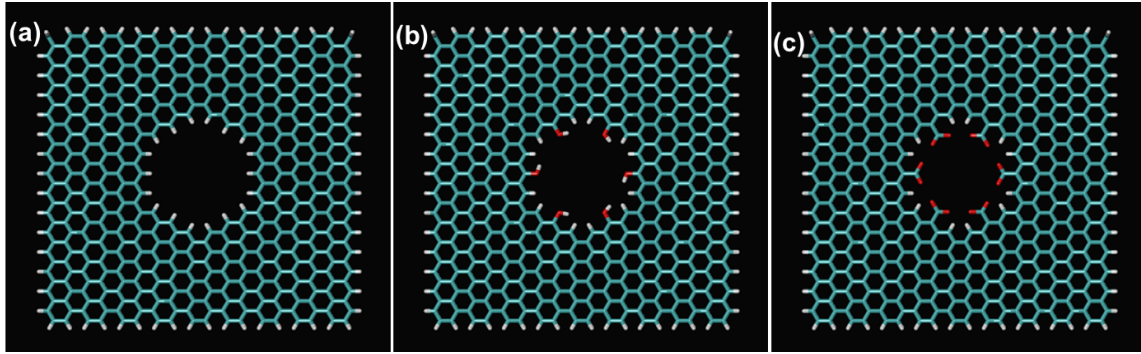
Fig. 5.1 Snapshots of (a) NPG-H (b) NPG-OH (c) NPG-COO⁻ functionalized membranes

A solvated membrane system was constructed by locating a TIP3P water box with xy dimensions of $36\,\text{Å} \times 36\,\text{Å}$ and an extended dimensions of $50\,\text{Å}$ and $40\,\text{Å}$ along the $-z$ and $+z$ axis of the membrane, respectively. A system with a 0.5 M NaCl feed solution (FS) concentration was generated by randomly adding the appropriate number of Na^+ and Cl^- ions into the FS domain. For the COO^- functionalized NPG, counter ions were added to the solvated system to achieve charge neutrality since all three carboxyl groups were assumed to be deprotonated. A graphene piston with similar xy dimensions as the water box was located on top of the FS domain to induce a hydrostatic pressure difference across the membrane for the pressure-induced flux simulations. External forces were applied to the graphene piston resulting in applied pressures of 60, 100, 140, 180 and 220 MPa across the membrane.

The performance of NPG membranes in forward osmosis (FO) mode was also investigated by simulating osmotic water transport across the membrane under similar conditions. The setup for the osmotic transport simulations consisted of the hydrated membrane with a 0.5 M NaCl FS and a 2 M NaCl draw solution (DS) located along the $-z$ and $+z$-directions,

78

respectively. In the case of the FO mode simulations, the driving force for water transport is provided by the osmotic pressure gradient across the membrane, hence no external forces were applied on the graphene piston. The carbon atoms of the membrane were fixed while the attached functional groups and hydrogen atoms were free to move during the simulations. Production simulations were conducted under the NVT ensemble and data were saved at 10 ps interval for analysis.

5.2.2 Simulation details

All simulations were performed with the NAMD MD package [92] using CHARMM force field [93, 94]. Simulations were performed under NPT and NVT ensembles using Langevin dynamics thermostat and a Noose-Hoover Langevin piston for temperature and pressure control, respectively. A 1 ns equilibrium MD simulation in the NPT ensemble was performed at 300 K and 1 atm, followed by 1 ns NVT simulation on the NPT-pre-equilibrated system. All bonds involving hydrogen atoms were restrained to their equilibrium value using the SHAKE algorithm [95]. The long-range electrostatic interactions were computed using Particle Mesh Ewald [96] and periodic boundary conditions were applied in all directions. The non-bonded interactions were subjected to a switching cutoff distance of 12 Å. An integration time step of 1 fs was employed in all simulations.

5.2.3 NOM fouling simulations

Simulations were further performed to investigate the fouling behavior of NPG membranes and the effect of organic fouling on water flux using humic acid (HA) as a representative NOM foulant. Umbrella sampling simulations were performed to probe the nature and strength of membrane-foulant interactions. A solvated NPG-HA complex was generated by randomly locating a single HA molecule on the surface of each membrane and equilibrating the system at a temperature of 300 K and 1 atm pressure. Umbrella sampling simulations of the solvated complexes were performed using the collective variable mod-

ule implemented in NAMD. A harmonic potential with a force constant of 20 kcal/mol Å^2 was applied to restrain the center-to-center distance of the NPG membranes and the HA molecule. The position along the reaction coordinate was varied from the optimum intermolecular separation to 20 Å in 0.5 Å increments, resulting in a series of windows with overlapping distributions. Each window was simulated for 1 ns and the coordinates saved at 10 ps interval for analysis. The potential of mean force (PMF) describing the interaction of the HA with the NPG membranes were generated from the output of the simulations using the weighted histogram analysis method [121, 122].

In evaluating the influence of NOM foulant on NPG membrane permeability, 10 HA molecules were randomly located on the surface of the equilibrated hydrated membrane resulting in a foulant layer thickness of 24.2 Å. Counter ions were added to the system to compensate for the deprotonated carboxyl groups in the HA molecule. Water molecules overlapping with the NOM layer and the counter ions were removed and the system was equilibrated following procedures described previously. The effect of NOM foulant on water flux was quantified by repeating the pressure-induced flux simulation procedures described above.

5.3 Results and discussion

5.3.1 Water permeability and salt rejection

Snapshots from the pressure-induced flux simulations presented in Fig. 5.2 show the displacement of the graphene piston over the simulation period. A lower graphene position is observed as a result of the movement of water across the membrane. Fig. 5.3 shows a comparison of the permeability rates of pure water and a representative seawater containing 0.5 M NaCl. At the initial stage, the observed graphene displacements indicates similar water permeability for both systems. However, as the simulation proceeds, the movement of water across the membrane causes a decrease in the volume of the FS domain and a subsequent increase in the FS salt concentration. The increase in concentration causes a buildup

80
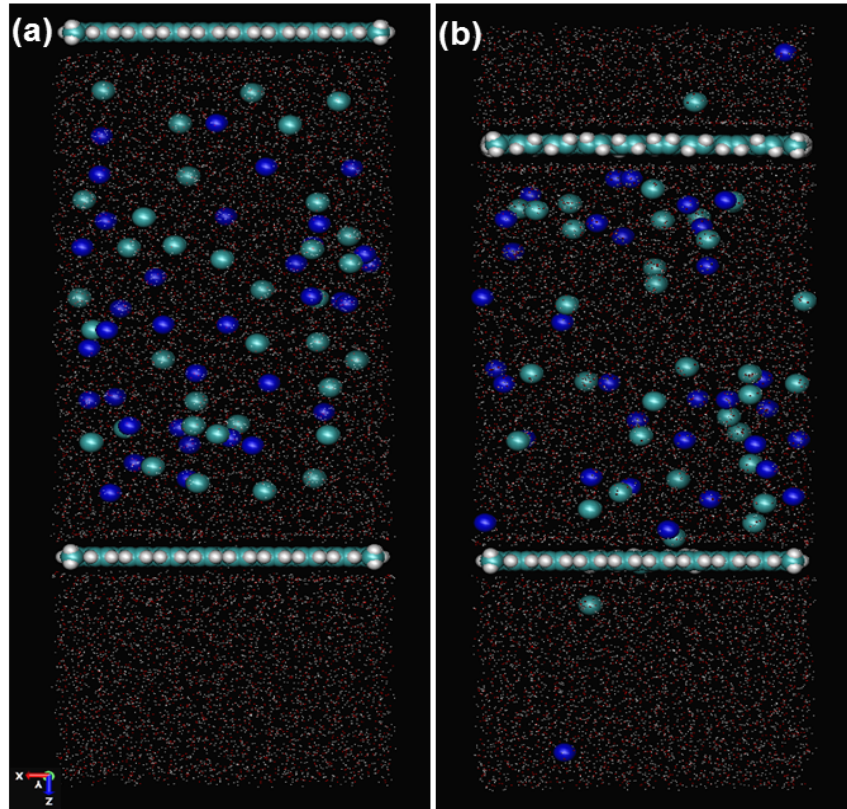
Fig. 5.2   Snapshots of (a) Pressure-induced flux simulation initial setup (b) Pressure-induced flux simulation after 10 ns. Graphene and NPG membrane are shown in VDW model, Na$^+$ and Cl$^-$ ions are shown as blue and green spheres, respectively and TIP3P water molecules shown as points.

of solutes at the membrane surface which increases the osmotic pressure that must be over-come for water to move across the membrane, hence the decreased water permeability in the presence of salt.

The size of nanopores in NPG dictates the overall membrane performance in terms of water flux and salt rejection. Based on a size exclusion principle, smaller pores can effectively hinder salt passage across the membrane but at the expense of reduced water flux. Thus, it is critical to determine an optimum pore size capable of rejecting salt ions while allowing water permeation. A recent study suggests that pores must be narrower than 5.5 Å to effectively hinder the passage of salt and allow water permeation [13]. Pore diameters were varied from 7.6 Å to 11.2 Å to investigate the effect of pore size on water

81
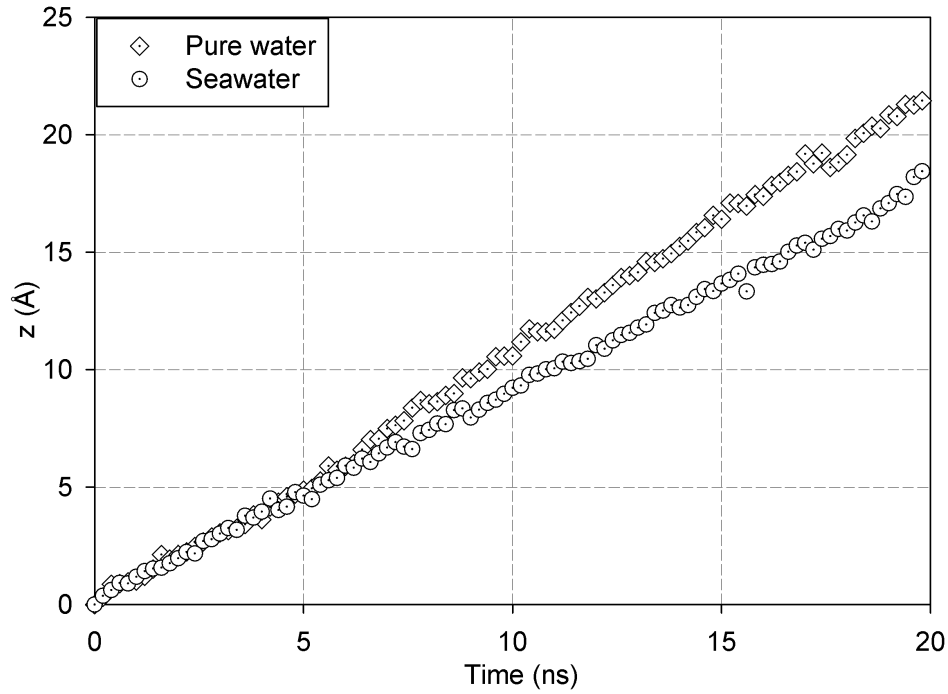
Fig. 5.3   Piston displacements for pure water and seawater.

flux and salt rejection in a pristine NPG membrane. Salt rejection (R) is calculated using:

$$R = \left(1 - \frac{C_p}{C_F} \right) \tag{5.1}$$

where C_P and C_F are the NaCl concentrations in the permeate and FS domain. At higher applied pressure, the FS domain is likely to be depleted during the course of the simulation. Therefore, realistic estimates of the salt rejection are obtained at the time when half of the FS water has flowed to the permeate side of the membrane [13]. While water flux increases with increasing pore diameter, salt rejection decreases because of the lower energy barrier for salt permeation. The 7.6 Å pore diameter exhibits the highest salt rejection (98.6%) with only one Na^+ ion permeating the membrane during the time frame of the simulations. In contrast, a few ions permeated the membrane in the case of the 11.2 Å pore diameter resulting in a NaCl rejection of 93%. Thus the size of the nanopore is key in evaluating water flux and salt rejection in NPG desalination membranes.

82

Fig. 5.4 shows a comparison of the water flux in FO and RO modes across the pristine membrane. The difference in the molar concentrations of the FS and DS created an initial
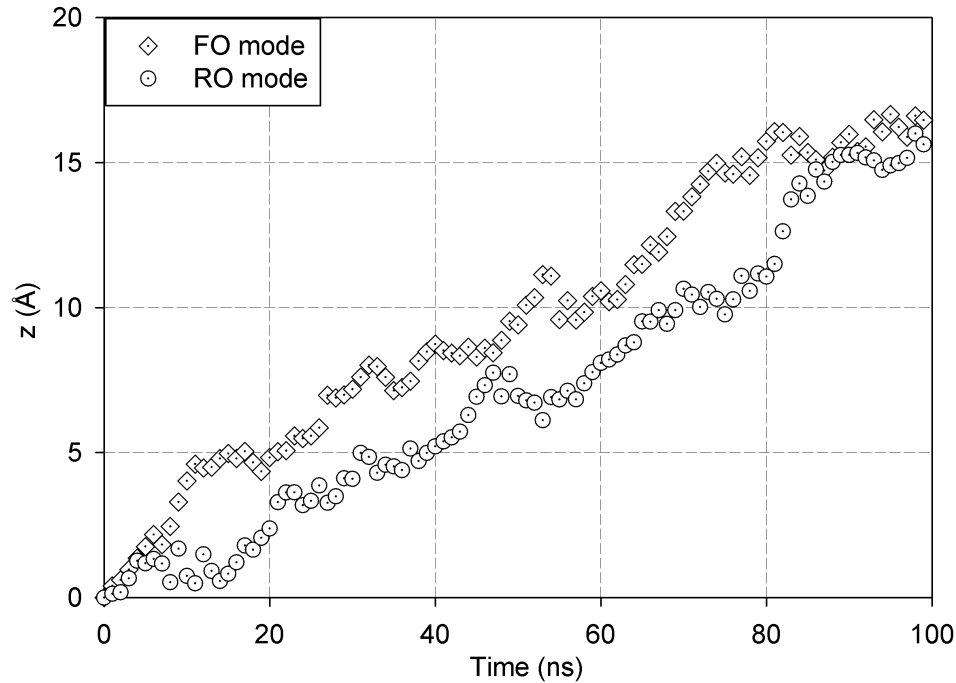
Fig. 5.4   Simulated water flux in RO and FO modes of operation.

osmotic pressure gradient of 7.5 MPa, across the membrane. In order to compare the desalination performance of NPG in both FO and RO modes, water flux across the membrane was simulated in RO mode by applying 0.003 kcal/mol external force on the graphene, corresponding to a 7.5 MPa applied pressure. As indicated by the results, the osmotic driving force in FO systems can provide water flux comparable to that of RO systems. The observed lower flux in RO mode is partly due to the reduction in driving force caused by the osmotic pressure gradient across the membrane. This reduction in driving force can be compensated by providing an additional pressure to offset the osmotic pressure gradient to establish the same total driving force for FO and RO modes of operation.

A pressure range of 60-220 MPa is investigated in RO mode to evaluate the effect of applied pressure on water flux and salt rejection as shown in Fig. 5.5. Pressures higher
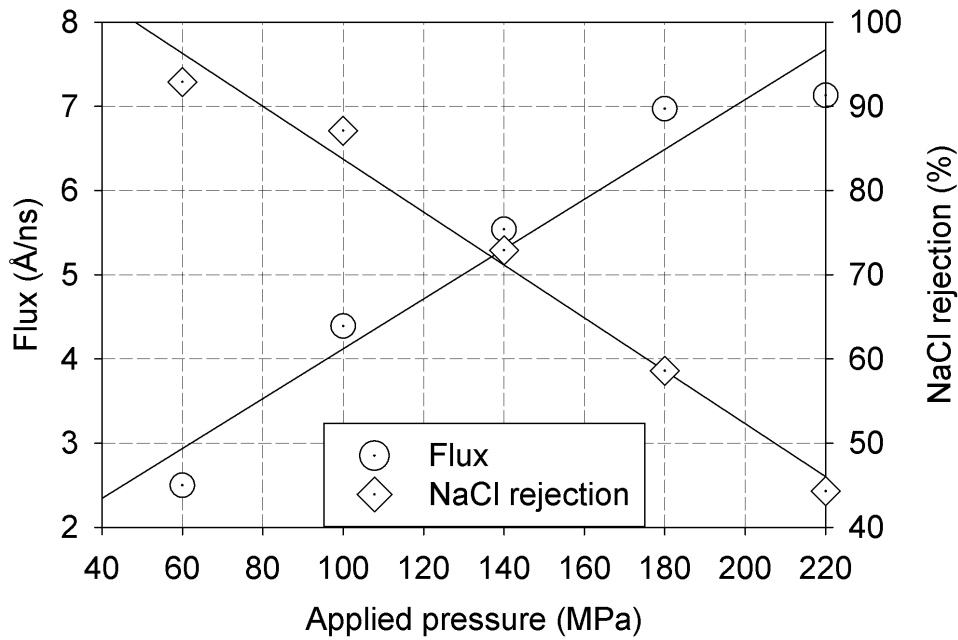
Fig. 5.5   Water flux and salt rejection as a function of applied pressure.

than typical RO systems are applied to observe significant graphene displacement over the time frame of the simulations. As shown in the figure, the water flux shows a linear dependence on the applied pressure which is typical of RO systems. Despite the higher pressure range investigated, a similar trend is expected in systems with lower to moderate applied pressure. Interestingly, an increase in salt flux is also observed at higher pressure. This can be attributed to the rapid response of ions to pressure increase [13] and the increased compression of the FS space domain at higher pressure. Moreover the random movement of ions in solution is enhanced at elevated pressure which increases the tendency of ions approaching the pore of the membrane and subsequent ion permeation.

5.3.2   Influence of functionalization on water flux and salt rejection

The effect of surface functionalization on the performance of NPG membranes is investigated by estimating water flux and salt rejection in the functionalized NPG membranes. Although previous studies have directly compared water permeability of different func-

84

tionalized NPG membranes, the difference in pore diameter resulting from the attachment of the functional groups to the pores does not make this a fair comparison. Therefore, water permeability across the different NPG membranes is evaluated by comparing the normalized water fluxes across each membrane. The flow velocity at the pore is obtained by normalizing the flow rate of the graphene piston to the area of each pore. As shown in Fig. 5.6, OH functionalized pore indicates the highest water permeability with COO⁻ functionalized pore recording the lowest water flux. Recent studies have attributed the high
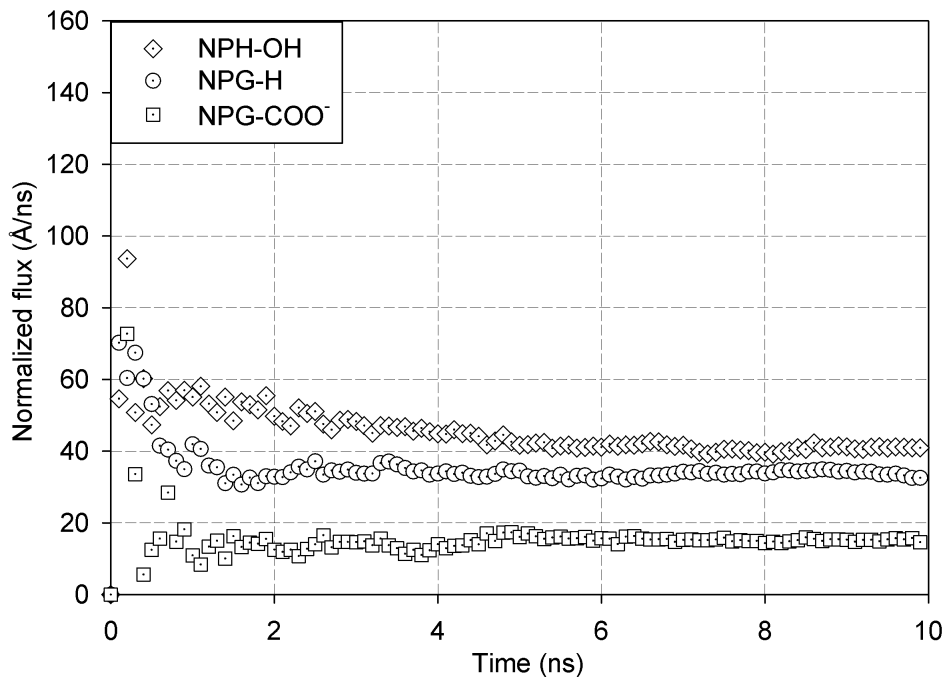
Fig. 5.6 Normalized water flux as a function of NPG functionalization.

water permeability of the OH functionalized pore to its hydrophilic nature which favors water transport compared to the hydrophobic nature of hydrogenated pores which imposes conformational restraint on water molecules approaching the rim [13]. The reduced water permeability across the NPG-COO⁻ membrane is due to the accumulation of Na^+ ions around the negatively charged carboxyl rims thereby reducing the available pore diameter for water permeation. This was evident in the increased Na^+ ion concentration around the pore over the course of the simulations. The reduced water flux partly results from the

slight increase in the osmotic pressure due to the additional Na^+ counter ions added to the system to maintain electroneutrality.

A comparison of salt rejection for the different functionalized membranes is presented in Fig. 5.7. The COO^- functionalized pore outperforms the pristine and OH functionalized pores in salt rejection possibly due to the repulsion of Cl^- ions approaching the negatively charged rim. The association of Na^+ ions to the pore also contributes to a reduction in total ion permeation across the COO^- functionalized membrane, hence the increased salt rejection. In order to separate the effect of FS ions on water flux, the pure water permeability
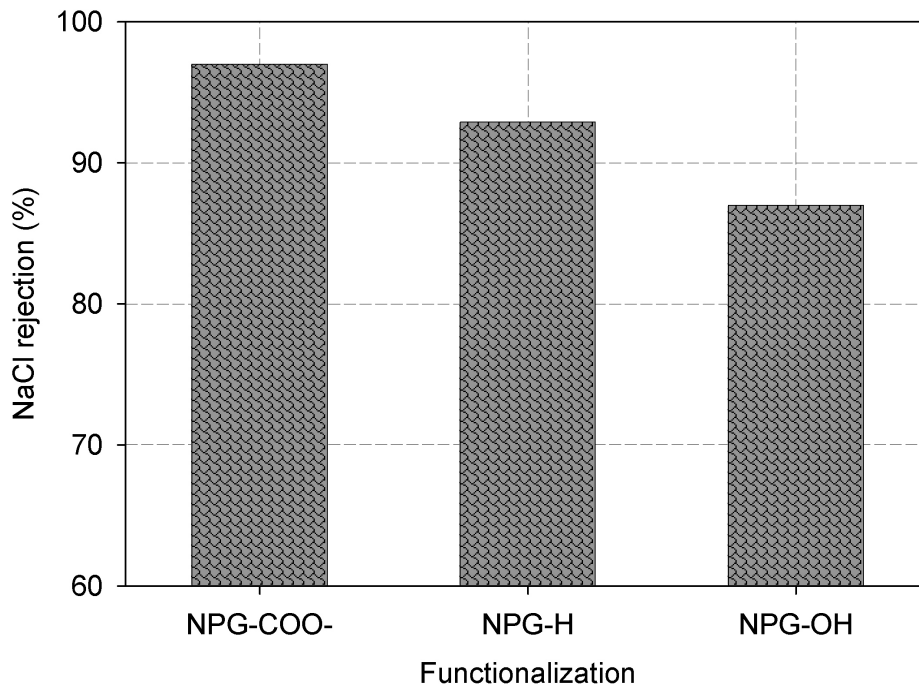
Fig. 5.7   Salt rejection as a function of NPG functionalization

of the functionalized NPG membranes are evaluated using pure water in the FS domain. As presented in Fig. 5.8, although the COO^- functionalized pore still indicates the lowest water flux, the results show an overall increase in water permeability compared to the observed water flux in RO mode, which is expected because of the opposing osmotic pressure gradient in RO mode that counteracts the applied pressure. The effect of the osmotic

86
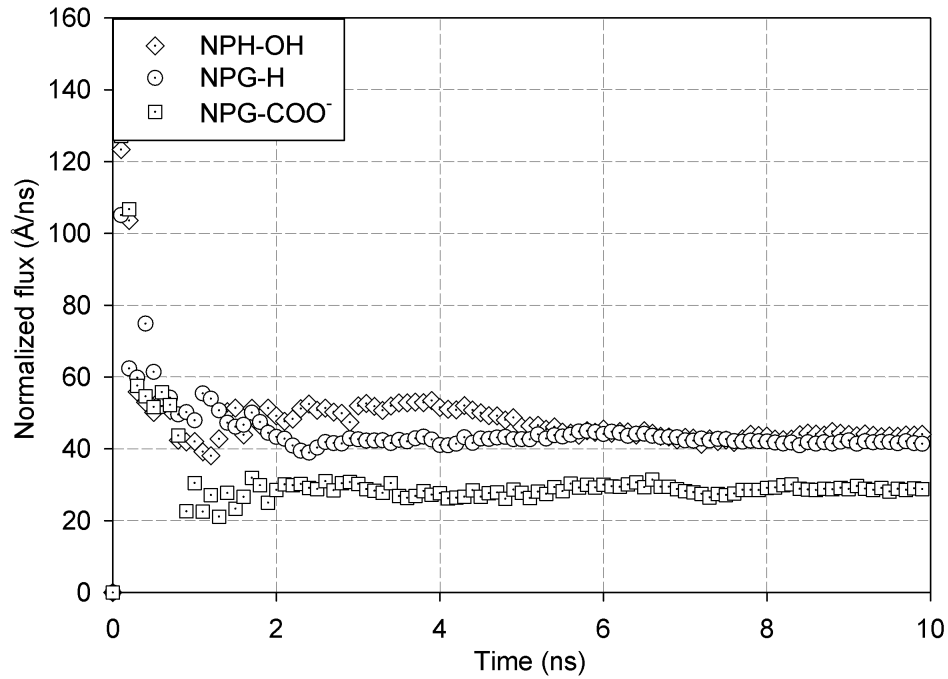
Fig. 5.8   Normalized pure water flux as a function of NPG functionalization

pressure is dominant in the case of the NPG-COO⁻ membrane because of the increased association of Na^+ onto the membrane pore which increases the buildup of ions on the membrane surface. Interestingly, the pure water flux across the pristine pores approaches that of the OH functionalized pores although the NPG-OH membrane exhibits a slightly higher water permeability.

5.3.2.1   Influence of NOM fouling on water flux

The association of humic substances onto membranes can significantly impact membrane permeability and water flux across membranes. The major mechanisms contributing to the association of NOM onto CNM-based membranes include $pi-pi$ interactions, hydrophobic effects and electrostatic interactions. The free energies associated with the interactions of NOM with NPG membranes are quantified and used to evaluate the fouling propensity of the pristine and functionalized membranes. Fig. 5.9 shows snapshots of the initial and final stages of the simulation of NOM interaction with NPG-H. As shown in its lowest

87

energy conformation, NOM interacts favorably with the pristine NPG membrane with its aromatic groups oriented towards the surface of the membrane to enable $pi-pi$ interactions. Moreover, a greater surface area of the NOM is exposed to the adsorbent due to possible
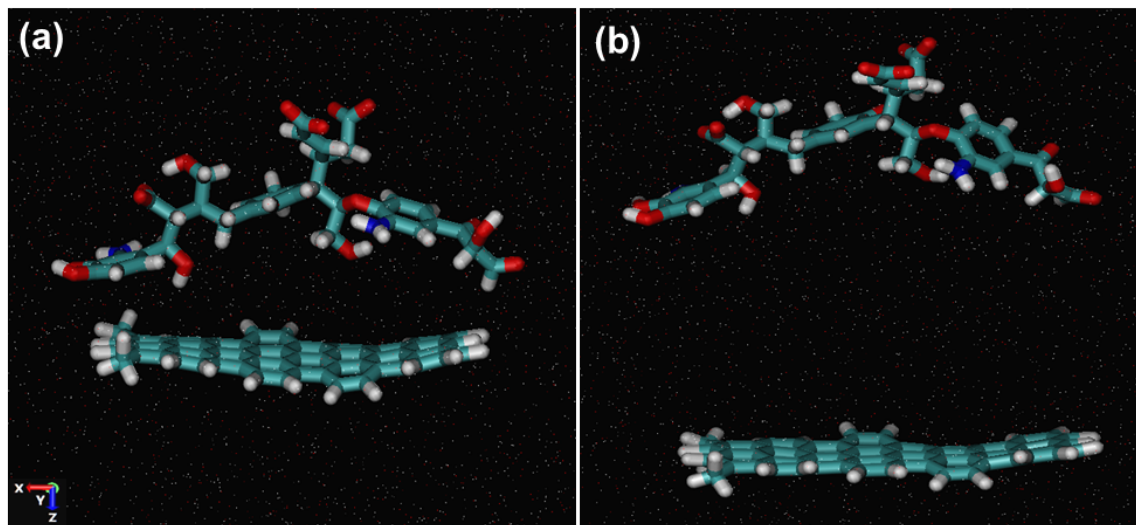
Fig. 5.9 Snapshots of (a) NOM interacting with NPG-H at optimum separation (b) NOM interacting with NPG-H at distant separation.

overlap of "orbitals" with the membrane, resulting in an overall increase in the van der Waals interactions.

The PMF depicting NOM interaction with NPG-H as a function of separation distance is presented in Fig. 5.10. The binding of NOM onto the pristine NPG membrane is associated with a free energy difference of -16.0 kcal/mol at an intermolecular separation of 10.5 Å, suggesting that NOM adsorption onto the membrane is energetically favored. The calculated free energies indicate favorable interactions between the NPG membranes and NOM in all cases as presented in Fig. 5.11. The interaction of NOM with the NPH-OH membrane is characterized with a less favorable binding energy compared to the pristine membrane. The hydrophilic nature of the OH groups is expected to reduce hydrophobic interactions between the membrane and NOM foulant and induce electrostatic repulsion between the polar functional groups and the negatively charged NOM. In the case of the pristine NPG, NOM interaction with the membrane is dominated by short range van der

88
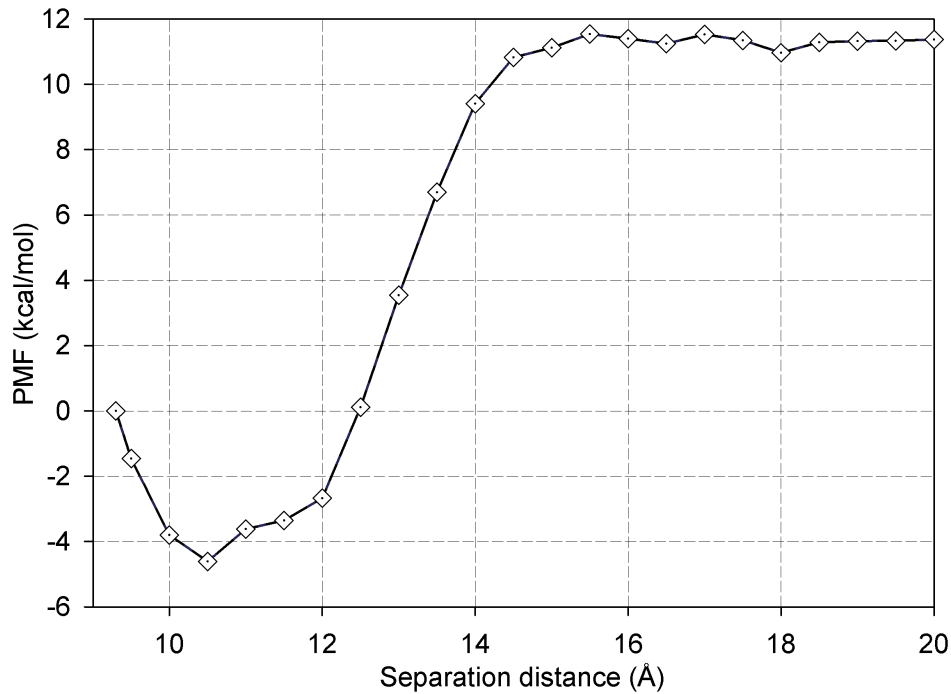
Fig. 5.10   PMF depicting NOM interaction with NPG-H membrane.

Waals. However with increasing polarity of the functional groups, the long range electro-static interactions become dominant which can enhance or decrease the overall membrane-foulant interaction depending on the interplay between the ions and the charged groups.

Surface charge plays a major role in the adsorption of humic substances onto aromatic membranes. For the pH under consideration, both NOM and NPG-COO⁻ functionalized membranes are expected to maintain an overall negative surface charge. As expected, the NOM-NPG-COO⁻ pair indicates a lesser stable configuration with the least favorable in-teraction because of the increased electrostatic repulsion between the negatively charged NOM and the NPG-COO⁻ membrane. Despite the association of Na⁺ ions onto the NPG-COO⁻ membrane, the membrane retains an overall negative surface charge which increases the resistance to NOM adsorption. In the presence of divalent ions however, the interaction between two charged surfaces can be enhanced through cation mediation. Studies have shown that divalent ions associate more strongly with the carboxyl groups of NOM than

89
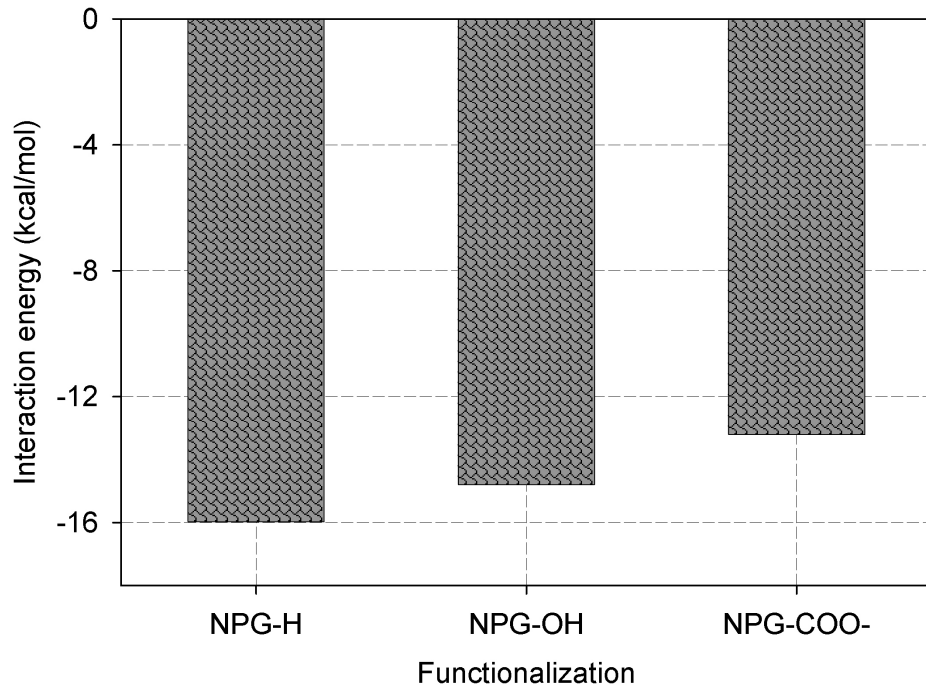
Fig. 5.11   Interaction energy as a function of NPG functionalization.

monovalent ions [62]. The presence of Na$^+$ ions did not induce a strong association of the NOM foulant onto the NPG-COO$^-$ membrane hence the reduced interaction. NOM interaction with NPG-COO$^-$ membrane is expected to be enhanced in the presence of divalent ions which can potentially increase the fouling propensity of NPG-COO$^-$ membranes.

A favorable membrane-foulant interaction translates to increased adsorption of NOM molecules onto the surface of the membranes as demonstrated in previous studies [55]. The preferential sorption of NOM onto NPG membranes ultimately leads to the buildup of NOM foulants and a reduction in water flux. The simulated effect of NOM foulant on water flux is presented in Fig. 5.12. The observed decline in water flux is due to the reduction in the available pore area which results in an increased resistance to water flow. It must be emphasized that, the observed decline in water flux results from the effect of a foulant layer with a fixed thickness. With the expected high NOM buildup, the influence of fouling on NPG membrane performance could be greater within the course of the filtration process.

90
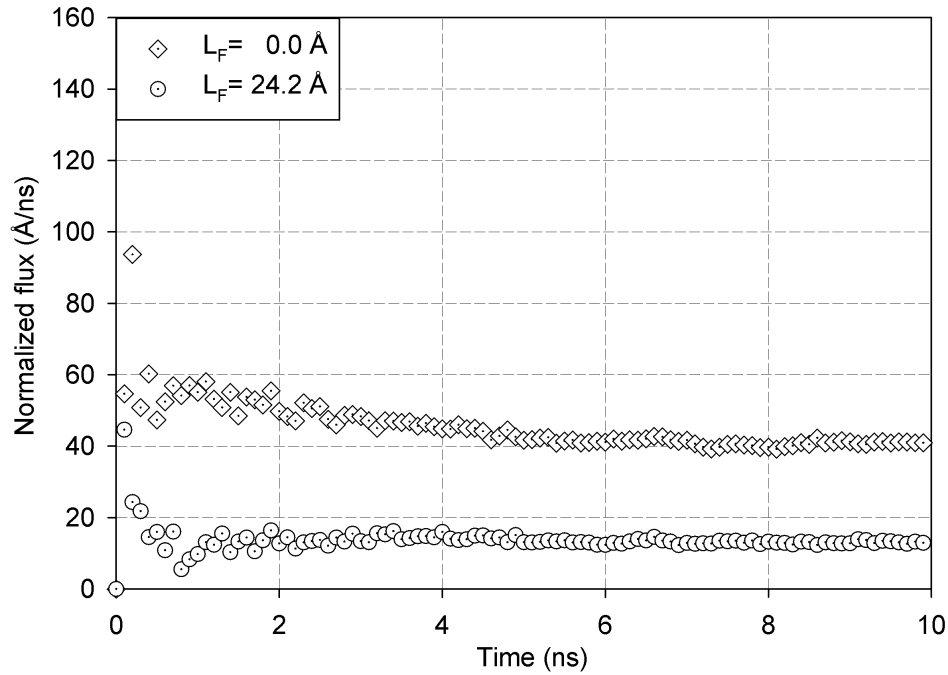
Fig. 5.12   Influence of NOM foulant on water flux.

5.4   Conclusions

MD simulations were performed to study the influence of surface functionalization on water flux, salt rejection, and NOM fouling in NPG membranes. Water flux and salt rejection were computed using data from pressure-induced flux simulations. NOM interactions with different functionalized NPG membranes were investigated using umbrella sampling simulations.

The results of the simulations indicated that pore diameter and surface functionalization have significant impact on the performance of NPG membranes. The results further established that surface functionalization can increase water flux and salt rejection and improve antifouling performance of NPG membranes. OH functionalization of the membranes resulted in a higher water flux as a result of the hydrophilic nature of OH pores which facilitate water transport. NPG-COO⁻ functionalized membrane exhibited a better salt rejection and antifouling properties but at the expense of reduced water flux.

91

NOM interaction with the NPG-COO⁻ membrane was characterized with the least binding energy due to electrostatic repulsion between the charged surfaces thus making NPG-COO⁻ functionalized membranes less prone to fouling. By simulating the interactions between NOM and the membranes, it became evident that van der Waals and electrostatic interactions are the dominant mechanisms driving the association of NOM foulants onto NPG membranes. The calculated free energies indicated favorable interactions between the NPG membranes and NOM in all cases. The favorable membrane-foulant interactions translates to increased adsorption of NOM onto the membrane resulting in a decline in water flux.

The interactions between organic foulants and NPG play a key role in assessing the desalination performance of NPG membranes. It has been established that the fouling propensity of functionalized NPG membranes is significantly influenced by surface functionalization and water chemistry conditions. Thus strategic selection of NPG functionalization could provide a means to control membrane-foulant interactions to potentially minimize membrane fouling.

Acknowledgments

CHAPTER 6

CONCLUSIONS AND RECOMMENDATIONS

A multiscale modeling framework connecting atomistic simulations to the process level is presented to study water and salt transport in membranes. The framework analyzes MD simulations data and extracts membrane parameters from the data to make full-scale predictions based on experimental conditions. Overall, the results highlight the importance of MD simulations in understanding membrane-based transport mechanisms at the atomic-scale. This work has generated new insight into water and salt transport mechanisms in membranes at the molecular and process levels as well as membrane-foulant interactions, and the influence of surface functionalization and water chemistry conditions on such interactions.

A criterion for estimating pure water flux in pressure-driven membranes was established by means of Bayesian inference and process level Monte Carlo simulations. The results of the Bayesian analysis suggest that given prior information on membrane processes, Bayesian updating can be performed using data from MD simulations to obtain realistic estimates of membrane parameters. It was established that MD simulations must be at least 5 ns long and must be based on unique structural configurations in order to capture realistic membrane properties at the molecular scale. The effectiveness of Bayesian updating is dependent on the availability of information about the process. Considering the vast information that can be generated from MD simulations, Bayesian inference can provide a means to incorporate prior experimental knowledge in model updating and serve as a useful tool for analyzing and interpreting MD simulations.

Membrane parameters obtained from MD simulations can be used to make predictions

that are consistent with experiments and reflective of process level conditions. Based on the consistency between the predictions and experimental data, it can be concluded that full-scale predictions based on parameters from MD simulations provide an effective means to scale up MD simulations. However, accurate predictions of full-scale observations require detailed characterization of the membrane properties. This was evident in the sensitivity of the membrane parameters on the full-scale predictions. At the full-scale, the flux scales inversely with the mass transfer boundary layer and membrane thickness because of the longer distance required for back diffusion of salt and the increased resistance to flow. For the FO system considered in this study, the critical point of the mass transfer boundary layer thickness was found to be within 1-10 μm based on a membrane thickness range of 5-15 μm. Moreover, the effects of several water quality parameters indicated significant impact on FO process, in accordance with experiments. Divalent ions provide greater driving force for water transport due to higher osmotic pressure and lower RSF compared to monovalent ions. The presence of NOM foulant layer resulted in a decline in water flux across the membrane suggesting that NOM fouling can significantly impact FO performance.

This work also highlights the potential application of ultrathin NPG membranes for water desalination. The identification of an optimum pore diameter was found to be critical in assessing water permeability and salt rejection performance of NPG membranes. OH functionalized pores exhibited the highest water flux while the COO^- functionalized NPG recorded the highest salt rejection as a result of the electrostatic interactions between ions and the negatively charged carboxyl rim. The results further indicate that surface functionalization of NPG membranes can enhance their desalination performance in terms of developing higher water flux and better salt rejection and improving antifouling properties. The pristine NPG membrane demonstrated greater NOM fouling propensity compared to the functionalized membranes. NOM interaction with the NPG-COO^- membrane was characterized with the least binding energy due to electrostatic repulsion between the charged surfaces thus making COO^- functionalized membranes less prone to fouling. The calcu-

94

lated free energies however indicated favorable interactions between the NPG membranes and NOM in all cases. The favorable membrane-foulant interactions translate to increased adsorption of NOM onto the membrane which decreased the water flux across the membrane because of the increased resistance to flow. The results suggest that depending on treatment conditions, strategic selection of NPG functionalization could provide a means to control membrane-foulant interactions to potentially minimize membrane fouling.

The presented framework can potentially serve as a useful tool for analyzing and interpreting MD simulations to elucidate water and salt transport mechanisms in membrane processes. The implementation of such a framework will provide an avenue for integrating simulation results into full-scale models which can expedite the development of strategic treatment conditions to optimize water flux and minimize membrane fouling.

Future work will focus on incorporating a full-scale material balance within the process model in order to accurately simulate bench-scale experimental conditions. A multiscale approach will also be adopted to evaluate the desalination performance of NPG membranes at the full-scale.

REFERENCES

[1]   D. Magen, Parliamentary committee of inquiry on the israeli water sector (2002).

[2]   Abengoa commissions Ghana's first desalination plant at Accra, http://www.water-technology.net/news/newsabengoa-commissions-ghanas-first-desalination-plant-at-accra-4557558, accessed: 2015-11-25.

[3]   T. Matsuura, Progress in membrane science and technology for seawater desalination: A review, Desalination 134 (1) (2001) 47–54.

[4]   P. Allison, C. Gasson, G. Intelligence, Desalination markets 2005–2015: A global assessment and forecast, Media Analytics.

[5]   Q. Yang, K. Y. Wang, T.-S. Chung, A novel dual-layer forward osmosis membrane for protein enrichment and concentration, Separation and Purification Technology 69 (3) (2009) 269–274.

[6]   B. Mi, M. Elimelech, Gypsum scaling and cleaning in forward osmosis: measurements and mechanisms, Environmental Science & Technology 44 (6) (2010) 2022–2028.

[7]   E. Cornelissen, D. Harmsen, K. De Korte, C. Ruiken, J.-J. Qin, H. Oo, L. Wessels, Membrane fouling and process performance of forward osmosis membranes on activated sludge, Journal of Membrane Science 319 (1) (2008) 158–168.

[8]   C. Y. Tang, Q. She, W. C. Lay, R. Wang, A. G. Fane, Coupled effects of internal concentration polarization and fouling on flux behavior of forward osmosis membranes during humic acid filtration, Journal of Membrane Science 354 (1) (2010) 123–133.

[9]   T. Y. Cath, Osmotically and thermally driven membrane processes for enhancement of water recovery in desalination processes, Desalination and Water Treatment 15 (1-3) (2010) 279–286.

[10]   N. T. Hancock, P. Xu, D. M. Heil, C. Bellona, T. Y. Cath, Comprehensive bench-and pilot-scale investigation of trace organic compounds rejection by forward osmosis, Environmental Science & Technology 45 (19) (2011) 8483–8490.

[11] M. Elimelech, Yale constructs forward osmosis desalination pilot plant, Membrane Technology 2007 (1) (2007) 7–8.

[12] A. Alexiadis, S. Kassinos, Molecular simulation of water in carbon nanotubes, Chemical Reviews 108 (12) (2008) 5014–5034.

[13] D. Cohen-Tanugi, J. C. Grossman, Water desalination across nanoporous graphene, Nano Letters 12 (7) (2012) 3602–3608.

[14] B. Pan, B. Xing, Adsorption mechanisms of organic chemicals on carbon nanotubes, Environmental Science & Technology 42 (24) (2008) 9005–9013.

[15] E. Harder, D. E. Walters, Y. D. Bodnar, R. S. Faibish, B. Roux, Molecular dynamics study of a polymeric reverse osmosis membrane, The Journal of Physical Chemistry B 113 (30) (2009) 10177–10182.

[16] J. H. Jensen, Molecular Modeling Basics, CRC Press, 2010.

[17] P. L. Freddolino, A. Y. Shih, A. Arkhipov, Y. Ying, Z. Chen, K. Schulten, 20 application of residue-based and shape-based coarse-graining to biomolecular simulations, Coarse-graining of Condensed Phase and Biomolecular Systems (2008) 299.

[18] S. J. Marrink, H. J. Risselada, S. Yefimov, D. P. Tieleman, A. H. De Vries, The MARTINI force field: coarse grained model for biomolecular simulations, The Journal of Physical Chemistry B 111 (27) (2007) 7812–7824.

[19] L. Monticelli, S. K. Kandasamy, X. Periole, R. G. Larson, D. P. Tieleman, S.-J. Marrink, The MARTINI coarse-grained force field: extension to proteins, Journal of Chemical Theory and Computation 4 (5) (2008) 819–834.

[20] A. Gautieri, S. Vesentini, A. Redaelli, How to predict diffusion of medium-sized molecules in polymer matrices. From atomistic to coarse grain simulations, Journal of Molecular Modeling 16 (12) (2010) 1845–1851.

[21] P. J. Bond, D. L. Parton, J. F. Clark, M. S. Sansom, Coarse-grained simulations of the membrane-active antimicrobial peptide maculatin 1.1, Biophysical Journal 95 (8) (2008) 3802–3815.

[22] Z. E. Hughes, J. D. Gale, A computational investigation of the properties of a reverse osmosis membrane, Journal of Materials Chemistry 20 (36) (2010) 7788–7799.

[23]   L. Monticelli, On atomistic and coarse-grained models for C60 fullerene, Journal of Chemical Theory and Computation 8 (4) (2012) 1370–1378.

[24]   A. W. W. Association, et al., Committee report–membrane processes in potable water treatment (PDF), American Water Works Association 84 (1) (1992) 59–67.

[25]   M. R. Wiesner, S. Chellam, Peer reviewed: The promise of membrane technology, Environmental Science & Technology 33 (17) (1999) 360A–366A.

[26]   S. Freeman, B. Long, S. Veerapaneni, J. Pressdee, Integrating low-pressure membranes into water treatment plants, American Water Works Association Journal 98 (12) (2006) 26.

[27]   N. Fujiwara, H. Matsuyama, Elimination of biological fouling in seawater reverse osmosis desalination plants, Desalination 227 (1) (2008) 295–305.

[28]   J. Xu, G. Ruan, L. Zou, C. Gao, Effect of chlorine and acid injection on hollow fiber RO for SWRO, Desalination 262 (1) (2010) 115–120.

[29]   J. Kessler, C. Moody, Drinking water from sea water by forward osmosis, Desalination 18 (3) (1976) 297–306.

[30]   A. Achilli, T. Y. Cath, A. E. Childress, Selection of inorganic-based draw solutions for forward osmosis applications, Journal of Membrane Science 364 (1) (2010) 233–241.

[31]   S. K. Yen, M. Su, K. Y. Wang, T.-S. Chung, et al., Study of draw solutes using 2-methylimidazole-based compounds in forward osmosis, Journal of Membrane Science 364 (1) (2010) 242–252.

[32]   J. R. McCutcheon, R. L. McGinnis, M. Elimelech, A novel ammonia-carbon dioxide forward (direct) osmosis desalination process, Desalination 174 (1) (2005) 1–11.

[33]   J. R. McCutcheon, R. L. McGinnis, M. Elimelech, Desalination by ammonia–carbon dioxide forward osmosis: influence of draw and feed solution concentrations on process performance, Journal of Membrane Science 278 (1) (2006) 114–123.

[34]   R. L. McGinnis, M. Elimelech, Energy requirements of ammonia–carbon dioxide forward osmosis desalination, Desalination 207 (1) (2007) 370–382.

[35] B. Mi, M. Elimelech, Chemical and physical aspects of organic fouling of forward osmosis membranes, Journal of Membrane Science 320 (1) (2008) 292–302.

[36] B. Mi, M. Elimelech, Organic fouling of forward osmosis membranes: fouling reversibility and cleaning without chemical reagents, Journal of Membrane Science 348 (1) (2010) 337–345.

[37] J. R. McCutcheon, M. Elimelech, Modeling water flux in forward osmosis: implications for improved membrane design, AIChE Journal 53 (7) (2007) 1736–1744.

[38] H. Ebro, Y. M. Kim, J. H. Kim, Molecular dynamics simulations in membrane-based water treatment processes: A systematic overview, Journal of Membrane Science 438 (2013) 112–125.

[39] F. Zhu, E. Tajkhorshid, K. Schulten, Collective diffusion model for water permeation through microscopic channels, Physical Review Letters 93 (22) (2004) 224501.

[40] F. Zhu, E. Tajkhorshid, K. Schulten, Pressure-induced water transport in membrane channels studied by molecular dynamics, Biophysical Journal 83 (1) (2002) 154–160.

[41] J. Goldsmith, C. C. Martens, Pressure-induced water flow through model nanopores, Physical Chemistry Chemical Physics 11 (3) (2009) 528–533.

[42] D. Cohen-Tanugi, J. C. Grossman, Water permeability of nanoporous graphene at realistic pressures for reverse osmosis desalination, The Journal of Chemical Physics 141 (7) (2014) 074704.

[43] Y. Luo, E. Harder, R. S. Faibish, B. Roux, Computer simulations of water flux and salt permeability of the reverse osmosis FT-30 aromatic polyamide membrane, Journal of Membrane Science 384 (1) (2011) 1–9.

[44] R. C. Ong, T.-S. Chung, Fabrication and positron annihilation spectroscopy (PAS) characterization of cellulose triacetate membranes for forward osmosis, Journal of Membrane Science 394 (2012) 230–240.

[45] Y. Luo, B. Roux, Simulation of osmotic pressure in concentrated aqueous salt solutions, The Journal of Physical Chemistry Letters 1 (1) (2009) 183–189.

[46] E. Aoustin, A. Schäfer, A. G. Fane, T. Waite, Ultrafiltration of natural organic matter, Separation and Purification Technology 22 (2001) 63–78.

[47] C.-H. Yu, C.-H. Wu, C.-H. Lin, C.-H. Hsiao, C.-F. Lin, Hydrophobicity and molecular weight of humic substances on ultrafiltration fouling and resistance, Separation and Purification Technology 64 (2) (2008) 206–212.

[48] M. Zhang, C. Li, M. M. Benjamin, Y. Chang, Fouling and natural organic matter removal in adsorbent/membrane systems for drinking water treatment, Environmental Science & Technology 37 (8) (2003) 1663–1669.

[49] Y. Yoon, G. Amy, J. Cho, N. Her, Effects of retained natural organic matter (NOM) on NOM rejection and membrane flux decline with nanofiltration and ultrafiltration, Desalination 173 (3) (2005) 209–221.

[50] A. Zularisam, A. Ismail, R. Salim, Behaviours of natural organic matter in membrane filtration for surface water treatment-A review, Desalination 194 (1) (2006) 211–231.

[51] C.-F. Lin, A. Y.-C. Lin, P. S. Chandana, C.-Y. Tsai, Effects of mass retention of dissolved organic matter and membrane pore size on membrane fouling and flux decline, Water Research 43 (2) (2009) 389–394.

[52] T. Carroll, N. Booker, J. Meier-Haack, Polyelectrolyte-grafted microfiltration membranes to control fouling by natural organic matter in drinking water, Journal of Membrane Science 203 (1) (2002) 3–13.

[53] A. Seidel, M. Elimelech, Coupling between chemical and physical interactions in natural organic matter (NOM) fouling of nanofiltration membranes: implications for fouling control, Journal of Membrane Science 203 (1) (2002) 245–255.

[54] Z. E. Hughes, J. D. Gale, Molecular dynamics simulations of the interactions of potential foulant molecules and a reverse osmosis membrane, Journal of Materials Chemistry 22 (1) (2012) 175–184.

[55] L. K. Boateng, J. Heo, J. R. Flora, Y.-G. Park, Y. Yoon, Molecular level simulation of the adsorption of bisphenol A and 17α-ethinyl estradiol onto carbon nanomaterials, Separation and Purification Technology 116 (2013) 471–478.

[56] J. Heo, L. K. Boateng, J. R. V. Flora, H. Lee, N. Her, Y.-G. Park, Y. Yoon, Comparison of flux behavior and synthetic organic compound removal by forward osmosis and reverse osmosis membranes, Journal of Membrane Science 443 (2013) 69–82.

[57] F. Wu, Y. Bai, Y. Mu, B. Pan, B. Xing, Y. Lin, Fluorescence quenching of fulvic acids by fullerene in water, Environmental Pollution 172 (2013) 100–107.

[58] R. S. DeFever, N. K. Geitner, P. Bhattacharya, F. Ding, P. C. Ke, S. Sarupria, PA-MAM dendrimers and graphene: Materials for removing aromatic contaminants from water, Environmental Science & Technology 49 (7) (2015) 4490–4497.

[59] A. Vinu, K. Hossain, G. S. Kumar, K. Ariga, Adsorption of l-histidine over meso-porous carbon molecular sieves, Carbon 44 (3) (2006) 530–536.

[60] M. Fontecha-Cámara, M. López-Ramón, M. Alvarez-Merino, C. Moreno-Castilla, Effect of surface chemistry, solution pH, and ionic strength on the removal of herbi-cides diuron and amitrole from water by an activated carbon fiber, Langmuir 23 (3) (2007) 1242–1247.

[61] E. Iskrenova-Tchoukova, A. G. Kalinichev, R. J. Kirkpatrick, Metal cation complex-ation with natural organic matter in aqueous solutions: molecular dynamics simula-tions and potentials of mean force, Langmuir 26 (20) (2010) 15909–15919.

[62] W.-Y. Ahn, A. G. Kalinichev, M. M. Clark, Effects of background cations on the fouling of polyethersulfone membranes by natural organic matter: Experimental and molecular modeling study, Journal of Membrane Science 309 (1) (2008) 128–140.

[63] K. Yang, L. Zhu, B. Xing, Adsorption of polycyclic aromatic hydrocarbons by car-bon nanomaterials, Environmental Science & Technology 40 (6) (2006) 1855–1861.

[64] Y.-H. Li, S. Wang, J. Wei, X. Zhang, C. Xu, Z. Luan, D. Wu, B. Wei, Lead adsorption on carbon nanotubes, Chemical Physics Letters 357 (3) (2002) 263–266.

[65] F. Su, C. Lu, Adsorption kinetics, thermodynamics and desorption of natural dis-solved organic matter by multiwalled carbon nanotubes, Journal of Environmental Science and Health Part A 42 (11) (2007) 1543–1552.

[66] Q. Zaib, I. A. Khan, N. B. Saleh, J. R. Flora, Y.-G. Park, Y. Yoon, Removal of bisphenol A and 17β-estradiol by single-walled carbon nanotubes in aqueous so-lution: adsorption and molecular modeling, Water, Air, & Soil Pollution 223 (6) (2012) 3281–3293.

[67] L. Joseph, Q. Zaib, I. A. Khan, N. D. Berge, Y.-G. Park, N. B. Saleh, Y. Yoon, Re-moval of bisphenol A and 17α-ethinyl estradiol from landfill leachate using single-walled carbon nanotubes, Water Research 45 (13) (2011) 4056–4068.

[68] J. Heo, J. R. Flora, N. Her, Y.-G. Park, J. Cho, A. Son, Y. Yoon, Removal of bisphe-nol A and 17β-estradiol in single walled carbon nanotubes–ultrafiltration (SWNTs–UF) membrane systems, Separation and Purification Technology 90 (2012) 39–52.

101

[69] B. Pan, K. Sun, B. Xing, Adsorption kinetics of 17α-ethinyl estradiol and bisphenol A on carbon nanomaterials. ii. concentration-dependence, Journal of Soils and Sediments 10 (5) (2010) 845–854.

[70] T. Kar, H. F. Bettinger, S. Scheiner, A. K. Roy, Noncovalent π-π stacking and CH–π interactions of aromatics on the surface of single-wall carbon nanotubes: an MP2 study, The Journal of Physical Chemistry C 112 (50) (2008) 20070–20075.

[71] U. Arsawang, O. Saengsawang, T. Rungrotmongkol, P. Sornmee, K. Wittayanarakul, T. Remsungnen, S. Hannongbua, How do carbon nanotubes serve as carriers for gemcitabine transport in a drug delivery system?, Journal of Molecular Graphics and Modelling 29 (5) (2011) 591–596.

[72] J. Goldsmith, C. C. Martens, Molecular dynamics simulation of salt rejection in model surface-modified nanopores, The Journal of Physical Chemistry Letters 1 (2) (2009) 528–535.

[73] A. Kalra, S. Garde, G. Hummer, Osmotic water transport through carbon nanotube membranes, Proceedings of the National Academy of Sciences 100 (18) (2003) 10175–10180.

[74] A. Sagle, B. Freeman, Fundamentals of membranes for water treatment, The Future of Desalination in Texas 2 (2004) 137–154.

[75] J. Herron, Asymmetric forward osmosis membranes, US Patent 7, 445, 712 (Nov. 4 2008).

[76] A. Szymczyk, P. Fievet, Investigating transport properties of nanofiltration membranes by means of a steric, electric and dielectric exclusion model, Journal of Membrane Science 252 (1) (2005) 77–88.

[77] V. Freger, S. Bason, Characterization of ion transport in thin films using electrochemical impedance spectroscopy: I. principles and theory, Journal of Membrane Science 302 (1) (2007) 1–9.

[78] V. Sharma, P. Singh, S. Gautam, P. Maheshwari, D. Dutta, R. Mukhopadhyay, Dynamics of water sorbed in reverse osmosis polyamide membrane, Journal of Membrane Science 326 (2) (2009) 667–671.

[79] S. Azari, L. Zou, E. Cornelissen, Assessing the effect of surface modification of polyamide RO membrane by l-DOPA on the short range physiochemical interactions

with biopolymer fouling on the membrane, Colloids and Surfaces B: Biointerfaces 120 (2014) 222–228.

[80] M. Kotelyanskii, N. Wagner, M. Paulaitis, Atomistic simulation of water and salt transport in the reverse osmosis membrane FT-30, Journal of Membrane Science 139 (1) (1998) 1–16.

[81] M. Kotelyanskii, N. Wagner, M. Paulaitis, Molecular dynamics simulation study of the mechanisms of water diffusion in a hydrated, amorphous polyamide, Computational and Theoretical Polymer Science 9 (3) (1999) 301–306.

[82] B. Corry, Designing carbon nanotube membranes for efficient water desalination, The Journal of Physical Chemistry B 112 (5) (2008) 1427–1434.

[83] F. Zhu, K. Schulten, Water and proton conduction through carbon nanotubes as models for biological channels, Biophysical Journal 85 (1) (2003) 236–244.

[84] J. Millam, K. Eppinnett, W. L. Hovell, R. Gilliland, Gaussview, version 3.09; semichem, Inc.: Shawnee Mission, KS.

[85] S. Grimme, J. Antony, S. Ehrlich, H. Krieg, A consistent and accurate *ab initio* parametrization of density functional dispersion correction DFT-D for the 94 elements H-Pu, The Journal of Chemical Physics 132 (15) (2010) 154104.

[86] S. Grimme, S. Ehrlich, L. Goerigk, Effect of the damping function in dispersion corrected density functional theory, Journal of Computational Chemistry 32 (7) (2011) 1456–1465.

[87] J. Kästner, J. M. Carr, T. W. Keal, W. Thiel, A. Wander, P. Sherwood, DL-FIND: An open-source geometry optimizer for atomistic simulations, The Journal of Physical Chemistry A 113 (43) (2009) 11856–11865.

[88] I. S. Ufimtsev, T. J. Martinez, Quantum chemistry on graphical processing units. 3. analytical energy gradients, geometry optimization, and first principles molecular dynamics, Journal of Chemical Theory and Computation 5 (10) (2009) 2619–2628.

[89] V. Maingi, V. Jain, P. V. Bharatam, P. K. Maiti, Dendrimer building toolkit: Model building and characterization of various dendrimer architectures, Journal of Computational Chemistry 33 (25) (2012) 1997–2011.

[90] D. Case, T. Darden, T. E. Cheatham III, C. Simmerling, J. Wang, R. Duke, R. Luo, R. Walker, W. Zhang, K. Merz, et al., Amber 12, University of California, San Francisco 1 (3).

[91] W. Humphrey, A. Dalke, K. Schulten, VMD: Visual Molecular Dynamics, Journal of Molecular Graphics 14 (1) (1996) 33–38.

[92] J. C. Phillips, R. Braun, W. Wang, J. Gumbart, E. Tajkhorshid, E. Villa, C. Chipot, R. D. Skeel, L. Kale, K. Schulten, Scalable molecular dynamics with NAMD, Journal of Computational Chemistry 26 (16) (2005) 1781–1802.

[93] O. Guvench, S. S. Mallajosyula, E. P. Raman, E. Hatcher, K. Vanommeslaeghe, T. J. Foster, F. W. Jamison, A. D. MacKerell Jr, CHARMM additive all-atom force field for carbohydrate derivatives and its utility in polysaccharide and carbohydrate–protein modeling, Journal of Chemical Theory and Computation 7 (10) (2011) 3162–3180.

[94] X. Zhu, P. E. Lopes, A. D. MacKerell, Recent developments and applications of the CHARMM force fields, Wiley Interdisciplinary Reviews: Computational Molecular Science 2 (1) (2012) 167–185.

[95] J.-P. Ryckaert, G. Ciccotti, H. J. Berendsen, Numerical integration of the cartesian equations of motion of a system with constraints: molecular dynamics of n-alkanes, Journal of Computational Physics 23 (3) (1977) 327–341.

[96] T. Darden, D. York, L. Pedersen, Particle mesh ewald: An n log (N) method for ewald sums in large systems, The Journal of Chemical Physics 98 (12) (1993) 10089–10092.

[97] A. D. Kiureghian, O. Ditlevsen, Aleatory or epistemic? Does it matter?, Structural Safety 31 (2) (2009) 105–112.

[98] A. Gelman, J. B. Carlin, H. S. Stern, D. B. Rubin, Bayesian data analysis, Vol. 2, Taylor & Francis, 2014.

[99] P. M. Lee, Bayesian statistics: An introduction, John Wiley & Sons, 2012.

[100] E. T. Jaynes, Probability theory: The logic of science, Cambridge university press, 2003.

[101] E. T. Jaynes, Prior probabilities, Systems Science and Cybernetics, IEEE Transactions on 4 (3) (1968) 227–241.

[102] E. Jaynes, Straight line fitting: A bayesian solution, Unpublished Manuscript, item 22.

[103] J. VanderPlas, Frequentism and bayesianism: A python-driven primer, arXiv preprint arXiv:1411.5018.

[104] H. Jeffreys, An invariant form for the prior probability in estimation problems, in: Proceedings of the Royal Society of London A: Mathematical, Physical and Engineering Sciences, Vol. 186, The Royal Society, 1946, pp. 453–461.

[105] A. R. Ortiz-Lasprilla, J. M. Caicedo, Comparing closed loop control models and mass-spring-damper models for human structure interaction problems, in: Dynamics of Civil Structures, Volume 2, Springer, 2015, pp. 67–74.

[106] W. K. Hastings, Monte carlo sampling methods using markov chains and their applications, Biometrika 57 (1) (1970) 97–109.

[107] J. R. Flora, R. A. Hargis, W. J. O'dowd, A. Karash, H. W. Pennline, R. D. Vidic, The role of pressure drop and flow redistribution on modeling mercury control using sorbent injection in baghouse filters, Journal of the Air & Waste Management Association 56 (3) (2006) 343–349.

[108] J. Geweke, et al., Evaluating the accuracy of sampling-based approaches to the calculation of posterior moments, Vol. 196, Federal Reserve Bank of Minneapolis, Research Department, 1991.

[109] W. Gao, F. She, J. Zhang, L. F. Dumée, L. He, P. D. Hodgson, L. Kong, Understanding water and ion transport behaviour and permeability through poly (amide) thin film composite membrane, Journal of Membrane Science 487 (2015) 32–39.

[110] S. Zhang, K. Y. Wang, T.-S. Chung, H. Chen, Y. Jean, G. Amy, Well-constructed cellulose acetate membranes for forward osmosis: minimized internal concentration polarization with an ultra-thin selective layer, Journal of Membrane Science 360 (1) (2010) 522–535.

[111] C. Y. Tang, Q. She, W. C. Lay, R. Wang, R. Field, A. G. Fane, Modeling double-skinned FO membranes, Desalination 283 (2011) 178–186.

[112] J. Heo, K. H. Chu, N. Her, J. Im, Y.-G. Park, J. Cho, S. Sarp, A. Jang, M. Jang, Y. Yoon, Organic fouling and reverse solute selectivity in forward osmosis: Role of working temperature and inorganic draw solutions, Desalination.

105

[113] L. T. Sein, J. M. Varnum, S. A. Jansen, Conformational modeling of a new building block of humic acid: approaches to the lowest energy conformer, Environmental Science & Technology 33 (4) (1999) 546–552.

[114] M. Mulder, Basic principles of membrane technology, Springer Science & Business Media, 1996.

[115] W. Pusch, R. Riley, Relation between salt rejection R and reflection coefficient σ of asymmetric cellulose acetate membranes, Desalination 14 (3) (1974) 389–393.

[116] Scilab Enterprises, Scilab: Free and open source software for numerical computation, Scilab Enterprises, Orsay, France (2012), http://www.scilab.org.

[117] V. Gekas, B. Hallström, Mass transfer in the membrane concentration polarization layer under turbulent cross flow: I. critical literature review and adaptation of existing sherwood correlations to membrane operations, Journal of Membrane Science 30 (2) (1987) 153–170.

[118] G. F. Schneider, S. W. Kowalczyk, V. E. Calado, G. Pandraud, H. W. Zandbergen, L. M. Vandersypen, C. Dekker, DNA translocation through graphene nanopores, Nano Letters 10 (8) (2010) 3163–3167.

[119] M. Bieri, M. Treier, J. Cai, K. Aït-Mansour, P. Ruffieux, O. Gröning, P. Gröning, M. Kastler, R. Rieger, X. Feng, et al., Porous graphenes: two-dimensional polymer synthesis with atomic precision, Chemical Communications (45) (2009) 6919–6921.

[120] D. C. Bell, M. C. Lemme, L. A. Stern, J. R. Williams, C. M. Marcus, Precision cutting and patterning of graphene with helium ions, Nanotechnology 20 (45) (2009) 455301.

[121] J. M. Rosenbergl, The weighted histogram analysis method for free-energy calculations on biomolecules. i. the method, Journal of Computational Chemistry 13 (8) (1992) 1011–1021.

[122] A. Grossfield, WHAM: The Weighted Histogram Analysis Method, Disponıvel em:< http://membrane. urmc. rochester. edu/content/wham.